Vector Polarization Observables of the Deuteron and A New Measurement of the Magnetic Dipole Form Factor G_M

BY

Peter Joseph Karpius

B.S. in Physics, State University of New York, College at Cortland, 1993
B.S.M.E., Clarkson University, 1994
M.Eng. in Engineering Physics, Cornell University, 1996
M.Sc. in Physics, University of New Hampshire, 2004

DISSERTATION

Submitted to the University of New Hampshire
in partial fulfillment of
the requirements for the degree of

Doctor of Philosophy

in

Physics

December 2005

This dissertation has been examined and approved.

Director, John Calarco
Professor of Physics

John Dawson
Professor of Physics

Maurik Holtrop
Assistant Professor of Physics

Dawn Meredith
Associate Professor of Physics,
Chairperson of the Department of Physics

William Turchinetz
Senior Research Scientist
(MIT Bates Linear Accelerator Center)

Date

Dedication

This work is dedicated to those who strive to give an unbiased view of the world.

Acknowledgments

This work is the culmination of over five years of effort, the success of which would not have been possible without the help of many people. I would first like to thank my advisor John Calarco for always being a patient mentor. Over the years John received my many questions, perhaps the same one for the 5^{th} time on more than one occasion, in a welcoming manner. He always took the time to answer them carefully and thoughtfully. I learned a great deal from John about physics and about being an experimentalist in general. I have little doubt that some day when I am struggling with some electronic device I will hear John in my head saying "Remember, the scope is your eyes!".

I would like to thank my doctoral committee. Thanks to John Dawson, Maurik Holtrop, Dawn Meredith, and Bill Turchinetz. I know that I pushed an aggressive schedule in the end and I truly appreciate you working with me to make it happen. Thanks to John Dawson for years of allowing me to barge in at any time and ask naive questions on theoretical physics. Thanks to Dawn for teaching me how to be a better teacher. Thanks to Bill T. for asking the hard questions at BLAST Collaboration meetings, and thanks to Maurik for his attention to detail.

Thank you to my graduate student colleagues at UNH, MIT, and Arizona. From the very beginning of my graduate career, in the "DeMeritt Hall Scintillator Factory," to showing what were the fruits of our labor at the APS-DNP meeting at the Ritz-Carlton in Maui, I worked, complained, celebrated, and laughed like hell with my boy Adrian "Moose" Sindile. I thank Tavi Filoti for taking so many graveyard shifts while I had morning classes. Special thanks go to Chi Zhang, on whose analysis mine relied so heavily I have considered making him co-author on this dissertation. Thanks to Jason for talking

with me about the decay of tritium and always offering us a place to stay when my wife and I would visit him and his wife Jen Cambridge. Thanks to Chris for really evaluating the TDC offsets once and for all. Thanks to Aaron for being the most natural teaching talent that I have seen in years. Thanks to Nik for teaching me some chess and always saying what is on your mind. Also thanks to Nik and Vitaliy for helping me with MASCARAD among other things. Thanks to Yuan for keeping that ion polarimeter away from me. Thanks to Eugene for playing rock and roll. Thanks to Ben for tolerating my overdone Australian accent. Thanks to Adam for really providing some nice automation with the HVGUI. You guys have saved my hide more than once and I wish I could repay you.

I would also like to thank many folks from and formerly from MIT and MIT-Bates. Doug Hasell was the lynch pin in the running of BLAST, perpetually cognizant and never angered by phone calls in the wee hours. Michael Kohl, thanks for your help in the pit with a ladder and an oscilloscope and in my analysis, always precise, and always a friend. Karen Dow, thanks for your answers to my numerous questions about how that black box CODA works. Bill Franklin thank you for keeping that compton polarimeter running like a clock. Taylan Akdogan, thanks for the auto-cruncher and setting up my Powerbook to run Linux. Tim Smith, thanks for tolerating my thousands of questions in that first summer and since then time and again. Townsend Zwart thank you for answering my many questions on the beam. Renee Fatemi, thanks taking over Aaron's analysis when I really needed it. Tancredi Botto thanks for helping me with my analysis, many laughs, and pizza while working on the retiming-OR. Thanks to Wang Xu for being patient with my dBGUI. Manouch Farkondeh, thank you for your sense of humor (telling Wang that his Bats Report was missing an 'e' for example :) and Richard Milner for being a fair and approachable director as well as employing me ahead of time for two months when I arrived in July 2000. I thank Jim Kelsey and Ernie Ihloff as well as the the technicians such as Peter Binns and Brian O'Rourke for being on call at all hours. I thank the Bates electricians for their strong coffee, always at the ready, my lifeblood.

Thanks also to Ernie Bisson at Bates and Aaron Hope, Dan Noe, and my good friend Scott "S-Dawg" Garman for keeping the Linux train moving.

I thank Bob Lambert for teaching me electrodynamics.

$$\nabla \cdot \mathbf{Jrr} \;=\; (\nabla \cdot \mathbf{J})\mathbf{rr} + (\mathbf{J} \cdot \nabla)\mathbf{rr} + \mathbf{r}(\mathbf{J} \cdot \nabla)\mathbf{r}$$

Holy cow I hope that's right!

Thanks to Katie, Rosemary, and Michelle for tolerating my sometimes last minute requests.

I would also like to thank Bogdan Diaconescu, Lorenzo Zana, Aaron Torok, and Jim Harper for listening to my practice talk. Thanks to Iulian Ruset for his advice on formatting.

Thanks to Liz and Rob for garbage can turkey and many good times.

Thanks to my family in NY, CT, VT, FL, and AU. I know you think I am crazy, and you may be right, but you supported me all this time and I really appreciate it.

But I say thank you the most to my friend, my wife, the love of my life, Laura. I always told people "I left a good job in Silicon Valley ... and my wife is being very good about it." Well you were much better than good. I know that I can be hard to live with sometimes, but you stuck with me through it all and supported me the whole way. You were Nobel Peace Prize good. Thanks Girlie!

For anyone I have not mentioned but played a positive part in all of this, please forgive me, it is not that I want to leave you out, it is just that, at this point, my brain is so cooked it is as if I fell asleep in the Bates South Hall during the injection flash of some really nice beam.

This work was supported by DOE grants 181021 (UNH) and DEFC02-94ER40818 (MIT-Bates).

Table of Contents

List of Tables

List of Figures

ABSTRACT

Vector Polarization Observables of the Deuteron

and A New Measurement of the

Magnetic Dipole Form Factor G_M

by

Peter Joseph Karpius
University of New Hampshire, December, 2005

A measurement of the vector analyzing power T_{11}^e in elastic electron-deuteron scattering has been performed at the MIT-Bates Linear Accelerator Center using a polarized electron beam, an internal polarized atomic deuterium target, and the symmetric BLAST (Bates Large Acceptance Spectormeter Toroid) detector in the Bates South Hall Ring. The beam helicity dependent target vector asymmetries, simultaneously measured in both sectors of BLAST, allow the extraction of T_{11}^e. To the best of our knowledge this is the first such use of a polarized target to determine T_{11}^e. Furthermore, these data, when combined with measurements of $A(Q^2)$ and the target tensor polarization observables T_{20} and T_{21}, allow the extraction of the magnetic dipole form factor G_M in the low Q^2 region.

CHAPTER 1

Introduction

A long standing goal in nuclear physics has been to understand the nucleon-nucleon (NN) force which binds protons and neutrons in the formation of atomic nuclei. Even with well understood probes of nuclear structure, the subatomic landscape is painted with the broad brush strokes of phenomenology. The inherent complexities that create this situation warrant the study of the most basic manifestation of the NN interaction. This representation is the nucleus of the second isotope of hydrogen, better known as the deuteron. Being a loosely bound system of a single proton and neutron the deuteron lends itself naturally to the study of the NN interaction.

The existence of the deuteron was first proposed in 1931 by Birge and Menzel [8] and a few months later discovered by Urey *et al*. [9]. However, at this time, Chadwick had not yet discovered the neutron and the theories of the day suggested that the nucleus was a mixture of protons and electrons. In fact, this was true of the neutron itself. In 1932 Heisenberg introduced the idea of a phenomenological potential to describe the pn force [10]. This theory held that the force must involve an exchange of spin and charge but still assumed that the neutron was a bound system of a proton and electron [1]. Spin arguments[1] and the success of the Fermi theory of β-decay [11] eventually led to the downfall of this idea. Furthermore, from basic quantum mechanics, an electron trapped in a well

[1]The classic case being the integer spin of ^{14}N which can not be explained by supposing that this nucleus contains fourteen half-integer spin protons to account for the mass and seven half-integer spin electrons to account for the charge.

with dimensions on the order of the nuclear diameter would have a kinetic energy $\sim$ 300 MeV, which is far in excess of the binding energy per nucleon ($\sim$ 8 MeV) of any known element.

A watershed year for nuclear physics came in 1935. Not only did Bethe and Peierls develop a Hamiltonian for the deuteron and introduce the short-range interaction [12], but in that same year Yukawa made his remarkable postulate. He suggested that the force between the neutron and the proton was mediated by yet another particle [13], which eventually came to be known as the π-meson. This was the first true application of quantum field theory to the problem of the NN interaction. Of course as time went on, it became clear that protons, neutrons, and even the mediating mesons were not fundamental paricles but were instead composed of quarks whose physics is governed my quantum chromodynamics (QCD). Notwithstanding, the picture of the deuteron in nucleonic degrees of freedom still provides the nuclear physicist with a valuable approach for describing the phenomenology of nuclear structure [14]. Furthermore, effective field theories (EFT), associated with chiral perturbation theory have, as of late, been gaining ground in this area of nuclear physics [15].

Because the physics of electromagnetic probes is well understood in terms of quantum electrodynamics (QED), electron scattering experiments are an excellent tool in the study of nuclear structure. Early experiments such as those performed by Hofstadter [16] examined the range of the NN potential. With the advent of polarized beams and targets, as well as recoil polarization measurements, spin degrees of freedom emerged as an important set of observables in electron scattering.

Recent review articles [1], [17], [18], illustrate the present state of knowledge on the structure of the deuteron as described by electromagnetic form factors. Following a multipole decomposition of the nuclear current, the phenomenological description of the electromagnetic structure of the deuteron can be parameterized in terms of three form factors, G_C, G_Q, and G_M representing the electric monopole, electric quadrupole, and magnetic

dipole nature of the deuterium nucleus respectively. Through a Rosenbluth separation, the magnetic form factor, G_M, can be extracted. However, one can make use of polarization observables to do this also, as well as extract the monopole and quadrupole form factors. The analyzing power, T_{20}, associated with the tensor polarization of the deuteron, is the dominant observable in separating the form factors and is the subject of much experimental and theoretical work [1]. Additionally, however, one has access to the beam-vector double polarization observables T_{10}^e and T_{11}^e. It turns out that the latter of these, which is the larger effect, is dominated by the interference of the form factors G_C and G_M at low momentum transfer. Since G_C is known to within a few percent in this region [7], one can use a measurement of T_{11}^e as an extra handle on G_M. Furthermore one can argue that measurements of T_{10}^e and T_{11}^e are of value in their own right. Such measurements help to constrain theories of nuclear structure in regions of significant model dependence.

To our knowledge no such measurement has been made of T_{11}^e with a polarized target. A proposal was submitted by Mitchell to measure this analyzing power at the Thomas Jefferson National Accelerator Facility (JLab) in Newport News, Virginia, in 1994 [2]. This proposal, however, suffered from systematic errors and a limited predicted event rate and did not receive approval by the Program Advisory Committee (PAC).

Central to this monograph is that of a measurement of both vector analyzing powers T_{10}^e and T_{11}^e albeit with a large relative error on the former due to its small value. These measurements exploit spin observables by using an intense polarized electron beam, a polarized internal deuterium target, and the BLAST detector[2] at the MIT-Bates Linear Accelerator Center in Middleton, Massachusetts. The contribution to the BLAST experiment that is described herein, is the analysis of but one of many simultaneous, and in some cases interdependent, reaction channels. Bates has a long history in electron scattering

[2]BLAST: Bates Large Acceptance Spectometer Toroid

and made earlier measurements of the analyzing powers[3] t_{20} [19], [20], [21], t_{21} [20], [21], and t_{22} [20], [21]. The current measurement of T_{10}^e and T_{11}^e, in fact, has been made concurrently with a new T_{20} experiment [22] at Bates by virtue of a target that simultaneously possesses both vector and tensor polarization, and thus has required no additional beam-time. To our knowledge, this is the first such measurement of the vector analyzing powers T_{10}^e and T_{11}^e using a polarized internal target.

As will be seen, these polarization observables can be written in terms of the elastic form factors G_C, G_Q, and G_M. By making use of the contentious [18] world data for $A(Q^2)$ and the BLAST data for the target tensor polarization observables T_{20} and T_{21}, we can use our measurement of the analyzing power T_{11}^e to perform a novel extraction of G_M in this Q^2 range. This innovative approach has thus led to providing a different handle on vector polarization observables and the magnetic form factor of the deuteron. These data provide additional degrees of freedom which constrain the various theoretical contributions to the deuteron wavefunction, and hence the NN interaction, in the low Q^2 region.

[3]The lower case t_{2q}'s here represent recoil polarization measurements.

CHAPTER 2

Theoretical Framework and Phenomenology

This chapter will serve as a brief survey of the formalism that underlies the cross section for unpolarized and polarized electron scattering. The phenomenology of not only the deuteron, but hadronic targets in general, and a brief overview of models of the deuteron as well as the kinematics involved will also be presented.

2.1 The Deuteron Elastic Form Factors

The phenomenology of the electromagnetic structure of the deuteron can be described by three form factors. Let us delve into the origin of these form factors, their relation to the cross section, and some parameterizations of the current set of world data.

2.1.1 Multipole Expansion of the Nuclear Current

A multipole analysis of the deuteron is key to understanding the contributions of the form factors. Proceeding generally [23], we have the nuclear four-current in momentum space as

$$J^{\mu}(\mathbf{q}) \equiv (\rho(\mathbf{q}), \mathbf{J}(\mathbf{q})) \tag{2.1}$$

Expanding the Fourier transform of the charge density and spherical components of the spatial current three-vector, we have

$$\rho(\mathbf{q}) \;=\; 4\pi \sum_{LM} i^L Y^*_{LM}(\Omega_q) \langle \Psi_f | \hat{C}_{LM}(|\mathbf{q}|) | \Psi_i \rangle \tag{2.2}$$

$$J_\lambda(\mathbf{q}) \;=\; -\sqrt{2\pi} \sum_{L \geq 1} i^L \sqrt{2L+1} \langle \Psi_f | [\hat{T}^{elec}_{L\lambda}(\mathbf{q}) + \lambda \hat{T}^{mag}_{L\lambda}(\mathbf{q})] | \Psi_i \rangle \tag{2.3}$$

where we have the Coulomb, Electric, and Magnetic irreducible tensor operators, $\hat{C}_{LM}(|\mathbf{q}|)$, $\hat{T}^{elec}_{L\lambda}(\mathbf{q})$ and $\hat{T}^{mag}_{L\lambda 9}(\mathbf{q})$ in nuclear Hilbert space. [24],

$$\hat{C}_{LM}(|\mathbf{q}|) \;=\; \int d\mathbf{r} \jmath_L(|\mathbf{q}|r) Y_{LM}(\Omega_r) \hat{\rho}(\mathbf{r}) \tag{2.4}$$

$$\hat{T}^{elec}_{LM}(\mathbf{q}) \;=\; \frac{1}{|\mathbf{q}|} \int d\mathbf{r} \nabla \times [\jmath_L(|\mathbf{q}|r) \mathbf{Y}^M_{LL}(\Omega_r)] \cdot \tilde{\mathbf{J}}(\mathbf{r}) \tag{2.5}$$

$$\hat{T}^{mag}_{LM}(\mathbf{q}) \;=\; \int d\mathbf{r} \jmath_L(|\mathbf{q}|r) \mathbf{Y}^M_{LL}(\Omega_r) \cdot \tilde{\mathbf{J}}(\mathbf{r}) \tag{2.6}$$

Here $\jmath_L$ are spherical Bessel functions, Y_{LM} are the spherical harmonics, and $\mathbf{Y}^M_{LL}$ are the vector spherical harmonics.

Parity and time-reversal-invariance place resrtictions on the existence of the Coulomb (CL), Electric (EL), and Magnetic (ML) multipoles [23]. The parity operator acts so as to multiply the the Coulomb and Electric multipoles by a factor of $(-1)^L$ and the Magnetic multipoles by $(-1)^{L+1}$. Since, for elastic scattering, parity is conserved, this means that only even values of L are allowed for the CL and EL multipoles, whereas only odd values of L are allowed for the ML multipoles. Furthermore, it can be shown that time-reversal invariance demands [24][1]

$$\langle L_f || \hat{T}^{elec,mag}_L || L_i \rangle \;=\; (-1)^{L_i - L_f + L + 1} \langle L_i || \hat{T}^{elec,mag}_L || L_f \rangle \tag{2.7}$$

For elastic scattering $L_i = L_f$ and thus only odd values of L are allowed. But remember, parity conservation forbids odd electric multipoles. Therefore the combination of time reversal invariance and parity conservation in elastic scattering allows only even Coulomb multipoles and odd Magnetic multipoles.

In a transition of one state of definite angular momentum to another, the addition rule governing the coupling of these states is

$$|L_f - L_i| \leq \ L \ \leq L_f + L_i \tag{2.8}$$

Therefore in the case of elastic scattering from the deuteron, which has spin and parity $J^\pi = 1^+$, L can equal $0, 1$, or 2. The allowable multipoles for this process, based on parity conservation and time reversal invariance demands described above, are the Coulomb multipoles C0, C2, and the Magnetic multipole M1. C0 and C2 reflect the charge monopole and quadrupole nature of the deuteron respectively. The M1 multipole reflects the magnetic dipole nature of the deuteron. These multipoles give rise to the three Sachs form factors G_C, G_Q, and G_M [23] which are discussed in the following section.

2.1.2 The Sachs Form Factors

The Sachs form factors introduced in the last section provide an intuitive picture of the internal electromagnetic structure of the nucleus as they are directly related to the spatial Fourier transforms of the nuclear charge and current densities [23]. The Sachs form

[1] We have made use of the definition of the reduced matrix elements [24]

$$\langle L_f M_f | \hat{O}_{LM} | L_i M_i \rangle = (-1)^{L_f - L_i} \begin{pmatrix} L_i & L & L_f \\ -M_f & M & M_i \end{pmatrix} \langle L_f || \hat{O}_L || L_i \rangle$$

factors are normalized in the $Q^2 \to 0$ limit such that [1]

$$G_C(Q^2 \to 0) \;=\; 1 \tag{2.9}$$

$$G_Q(Q^2 \to 0) \;=\; M_D^2 Q_D \;=\; 25.83 \tag{2.10}$$

$$G_M(Q^2 \to 0) \;=\; (M_D/M)\mu_D \;=\; 1.714 \tag{2.11}$$

where Q_D is the quadrupole moment[2] and μ_D is the magnetic dipole moment of the deuteron in its ground state. World data for G_C, G_Q, and G_M are shown in the Figure 2-1.

2.1.3 Parameterizations of the G_C, G_Q, and G_M

The curves correspsond to three parameteriztions of these data by Abbott [7]. These parameterizations have the following form.

Parameterization I:

$$G_X(Q^2) \;=\; G_X(0) \cdot \Big[1 - \Big(\frac{Q}{Q_X^0}\Big)^2\Big] \cdot \Big[1 + \sum_{i=1}^{5} a_{Xi} Q^{2i}\Big]^{-1} \tag{2.12}$$

where $X = C, Q$, or M and Q_X^0 is the first node of each form factor.

Parameterization II:

$$\begin{pmatrix} G_C \\ G_Q \\ G_M \end{pmatrix} \;=\; G_D^2\Big(\frac{Q^2}{4}\Big) \cdot \mathcal{M}(\eta) \begin{pmatrix} g_0 \\ g_1 \\ g_2 \end{pmatrix} \tag{2.13}$$

where G_D^2 is the square of a dipole nucleon form factor and g_k are reduced helicity transition amplitudes defined in terms of four Lorentzian factors which themselves depend on

[2] One can convert from fm^2, the conventional units of Q_d, to GeV^2, the units of M_d when taking $c = 1$, using the well known relation $\hbar c \simeq 197$ MeV-fm

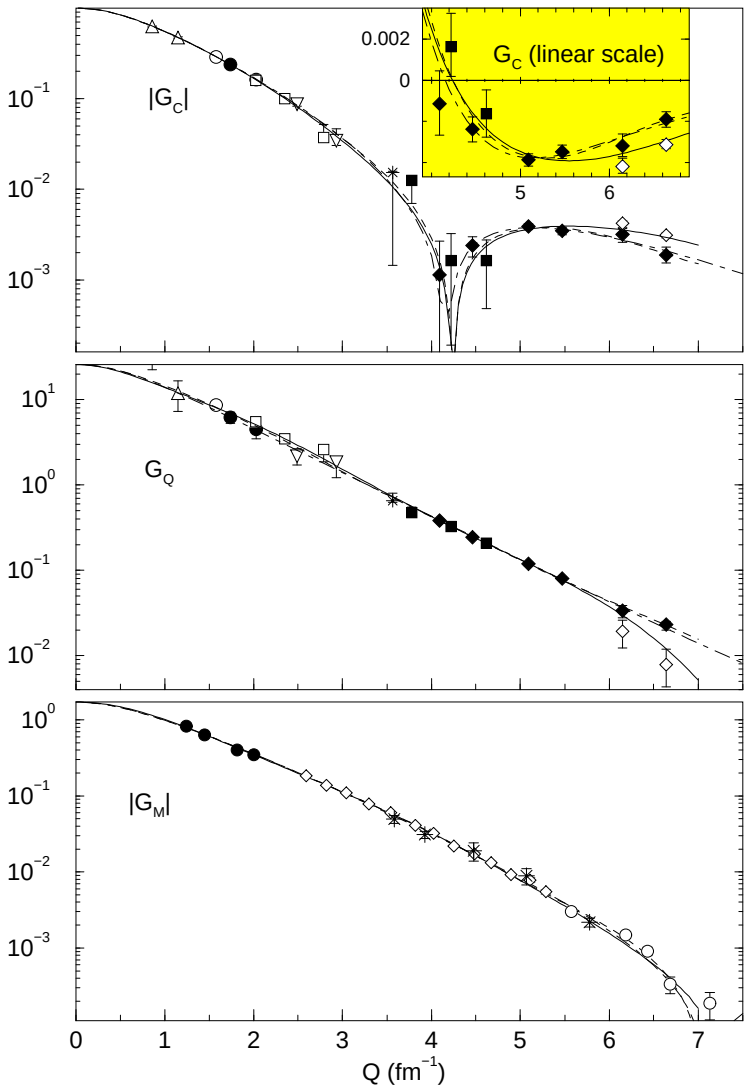

Figure 2-1: World Data and Parameterizations for the Deuteron Elastic Form Factors [1]: Parameterization I (solid line), II (dot-dashed line), III (short-dashed line)

two parameters,

$$g_k \;=\; Q^k \sum_{i=1}^{4} \frac{a_{ki}}{\alpha_{ki}^2 + Q^2} \tag{2.14}$$

Parameterization III:

$$G_X(Q^2) \;=\; G_X(0) \cdot e^{-\frac{1}{4}Q^2\gamma^2} \sum_{i=1}^{25} \frac{A_i}{1 + 2R_i^2/\gamma^2} \cdot \left(\cos(QR_i) + \frac{2R_i^2}{\gamma^2 \frac{\sin(QR_i)}{QR_i}} \right) \tag{2.15}$$

This parameterization is called a Sum-of-Gaussians (SOG). A_i and γ are the amplitudes and widths of the fitted data, R corresponds to the distance of the nucleons to the deuteron center of mass.

2.2 The Rosenbluth Cross Section

The elastic scattering of electrons from a general hadronic target can be described by the Feynman diagram shown in Figure 2-2 in the one-photon-exchange (OPE) approximation. The OPE approximation is justified as each vertex contributes a factor of $\sqrt{\alpha}$ thus leaving higher order QED corrections small compared to the leading term[3]. The momentum and spin of the electron(deuteron) are described by $k(P)$ and $s(\sigma)$ respectively, where primes on these variables represent the final state spin and momenta. $A^\mu(x)$ is the electromagnetic four-potential and $e\gamma^\mu$ is the vertex factor of this reaction. From quantum electrodynamics (QED), the differential cross section for the elastic scattering of unpolarized electrons of initial(final) energy $\epsilon(\epsilon')$ from an unpolarized target with internal structure can be written as

$$\frac{d\sigma}{d\Omega'} \;=\; \sigma_{Mott} \cdot \left(\frac{\epsilon'}{\epsilon}\right) \cdot \left[A(Q^2) + B(Q^2) \tan^2 \frac{\theta_e}{2} \right] \tag{2.16}$$

[3]where $\alpha = 1/137$ is the fine structure constant.

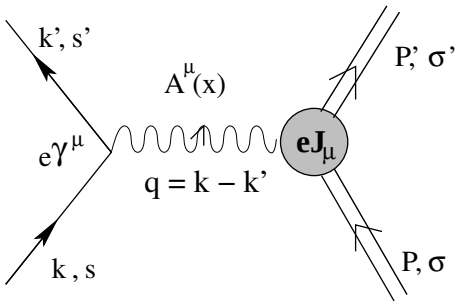

Figure 2-2: Feynman Diagram for Elastic Electron Scattering from a Complex Nucleus

This is the famous *Rosenbluth Cross Section* which was first derived in 1950 [25]. The structure functions $A(Q^2)$ and $B(Q^2)$ allow us to create a phenomenological description of the underlying structure of the target nucleus. Experimentally one can vary the incident electron beam energy and measured electron scattering angle and plot this cross section versus $\tan^2(\theta_e/2)$. A linear fit of the data will then allow for extraction of $A(Q^2)$ and $B(Q^2)$. This technique is called a Rosenbluth Separation. World data for $A(Q^2)$ and

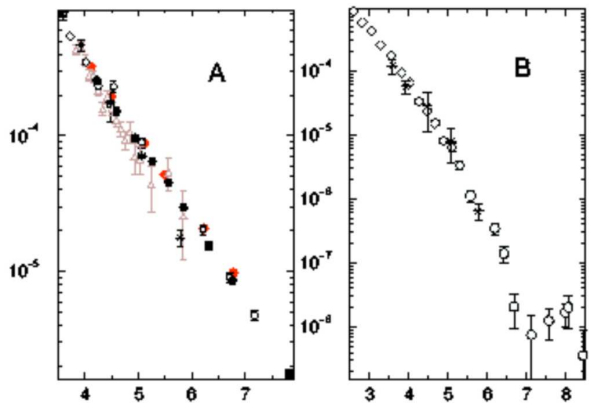

Figure 2-3: World Data for Deuteron Structure Functions $A(Q^2)$ and $B(Q^2)$ [1]

$B(Q^2)$ are seen in Figure 2-3. At forward scattering angles, $A(Q^2)$ dominates and is known to within approximately 3% [5]. Conversely, $B(Q^2)$ is determined through scattering at

backward angles and is known only to about 10% at low Q^2 [6].

The structure functions $A(Q^2)$ and $B(Q^2)$ can be written in terms of the deuteron elastic form factors as [1]

$$A(Q^2) = G_C^2(Q^2) + \frac{8}{9}\tau^2 G_Q^2(Q^2) + \frac{2}{3}\tau G_M^2(Q^2) \tag{2.17}$$

$$B(Q^2) = \frac{4}{3}\tau(1+\tau)G_M^2(Q^2) \tag{2.18}$$

$$\text{where } \tau = \frac{Q^2}{4M_d^2} \tag{2.19}$$

We can see that a Rosenbluth separation can determine G_M from $B(Q^2)$ but another observable is needed to separate G_C and G_Q.

2.3 Polarized Cross Section

In summarizing the formalism of the polarized cross section, we adopt the conventions for the scattering plane and the reaction plane shown in Figure 2-4. The angles θ^* and ϕ^*

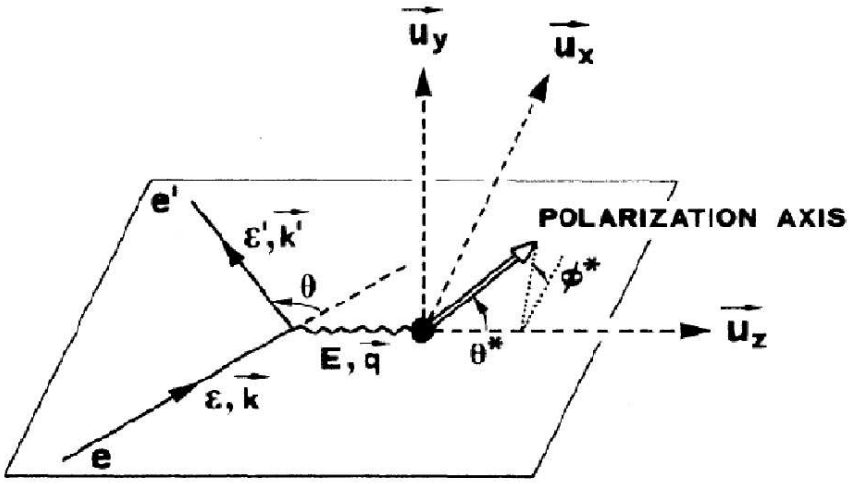

Figure 2-4: Scattering plane conventions

are defined as the polar and azimuthal angles between the target polarization vector and the direction of the three-momentum transfer $\mathbf{q}$.

Following Donnelly and Raskin [26], in the one-photon-exchange (OPE) Born-approximation the cross section for the scattering of polarized beam from a polarized target can be written quite generally as

$$\frac{d\sigma}{d\Omega}(h, P_z, P_{zz}) \;=\; \Sigma + h\Delta \tag{2.20}$$

where h is the helicity and polarization of the incident electron beam[4] and P_z and P_{zz} are the vector and tensor polarization of the target. The first term Σ contains the tensor analyzing powers T_{2q}. The second term is a product of h and the factor Δ which contains the vector analyzing powers T^e_{1q} [27]. Here the superscript on T^e_{1q} indicates that polarized beam is required to extract these observables.

$$\Sigma \;=\; \sigma_0\Big[1 + \Gamma\Big] \tag{2.21}$$

$$\sigma_0 \;= \sigma_{Mott} \cdot \left(\frac{\epsilon'}{\epsilon}\right) \cdot S \tag{2.22}$$

$$S \;= A(Q^2) + B(Q^2)\tan^2\frac{\theta_e}{2} \tag{2.23}$$

$$\begin{aligned} \Gamma \;=\quad & P_{zz}\Big[\tfrac{1}{\sqrt{2}}P_2^0(\cos\theta^*)T_{20}(Q^2,\theta_e) - \\ & \tfrac{1}{\sqrt{3}}P_2^1(\cos\theta^*)\cos\phi^* T_{21}(Q^2,\theta_e) + \\ & \tfrac{1}{2\sqrt{3}}P_2^2(\cos\theta^*)\cos 2\phi^* T_{22}(Q^2,\theta_e)\Big] \end{aligned} \tag{2.24}$$

[4] If one assumes that the beam is 100% polarized, then $h = \pm 1.0$.

$$\Delta \;=\; \sigma_0 P_z \Big[\sqrt{\tfrac{3}{2}} P_1(\cos\theta^*) T^e_{10}(Q^2,\theta_e) - \sqrt{3} P^1_1(\cos\theta^*)\cos\phi^* T^e_{11}(Q^2,\theta_e) \Big] \tag{2.25}$$

where the Legendre Polynomials $P_\ell(x)$ and Associated Legendre Polynomials $P^m_\ell(x)$ are, following the convention of Edmunds [28].[5]

2.3.1 Relating Polarization Tensors t_{kq} to Analyzing Powers T_{kq}

In specifying polarization moments, we use a right handed coordinate system that is defined in terms of the scattering plane. In the case of a recoil polarization measurement, we measure polarization tensors, conventionally denoted in the lower case t_{kq}. The z-axis is defined by the momentum vector of the outgoing deuteron, $\mathbf{P}_f$ and the y-direction is defined by the axial vector $\mathbf{P}_i \times \mathbf{P}_f$, where $\mathbf{P}_i$ is the momentum vector of the initial deuteron beam. When the recoil polarization is not measured and instead, a polarized target is used, we measure the analyzing powers T_{kq}. Here, the z-axis is defined by the *electron* initial momentum vector, $\mathbf{k}_i$, and the y-axis is defined by the axial vector $\mathbf{k}_i \times \mathbf{q}$, where again the three-momentum transfer $\mathbf{q}$ is just the momentum of the outgoing deuteron $\mathbf{P}_f$ in the lab frame.[6] Taking into account time-reversal-invariance, and the above definition of coordinate systems, we can relate the polarization tensors to the analyzing powers of the inverse reaction by [29]

$$T_{kq} \;=\; (-1)^{k+q} t_{k+q} \tag{2.26}$$

[5] Edmunds defines the Associated Legnedre Polynomials as

$$P^m_\ell(x) \;=\; (1-x^2)^{m/2} \frac{d^m}{dx^m} P_\ell(x)$$

whereas some authors retain a leading factor of $(-1)^m$. In the convention which we have adopted, this factor is absorbed into the spherical harmonics, of which the associated Legnedre polynomials are a part.

[6] Note that in the case of an incident beam of polarized deuterons, the z-axis would be defined by the momentum vector of the incident beam.

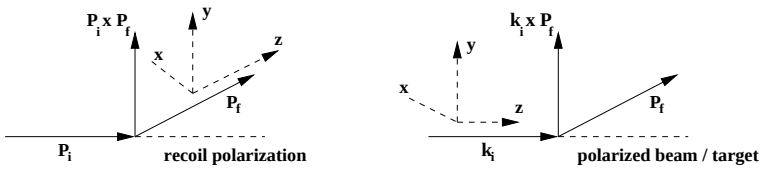

Figure 2-5: Coordinate system conventions for use with polarization tensors or analyzing powers

2.3.2 The Analyzing Powers T_{kq} in terms of G_C, G_Q, and G_M

Following the Madison Convention[29], the analyzing powers in terms of the deuteron elastic form factors are

$$T^e_{10}(Q^2,\theta_e) = -\sqrt{\frac{2}{3}}\frac{1}{S}\tau\{(1+\tau)[1+\tau\sin^2(\theta_e/2)]\}^{1/2}G_M^2\tan\frac{\theta_e}{2}\sec\frac{\theta_e}{2} \quad (2.27)$$

$$T^e_{11}(Q^2,\theta_e) = \sqrt{\frac{3}{2}}\frac{1}{S}\frac{4}{3}[\tau(1+\tau)]^{1/2}G_M(G_C+\frac{\tau}{3}G_Q)\tan\frac{\theta_e}{2} \quad (2.28)$$

$$T_{20}(Q^2,\theta_e) = -\sqrt{2}\frac{1}{S}\tau\Big(\frac{4}{3}G_CG_Q+\frac{4}{9}G_Q^2+\frac{1}{6}(1+(\tau+1)\tan^2(\theta_e/2))G_M^2\Big) \quad (2.29)$$

$$T_{21}(Q^2,\theta_e) = -\frac{2}{\sqrt{3}}\frac{1}{S}\tau\Big(\tau+\tau^2\sin^2(\theta_e/2)\Big)^{1/2}G_MG_Q\sec\frac{\theta_e}{2} \quad (2.30)$$

$$T_{22}(Q^2,\theta_e) = -\frac{1}{2\sqrt{3}}\frac{1}{S}\tau G_M^2 \quad (2.31)$$

where again $S = A(Q^2)+B(Q^2)\tan^2(\theta_e/2)$.

T_{20} is the dominant analyzing power used in separating G_C and G_Q [27]. The interference term of G_C and G_Q in T_{21} and the factor of G_M^2 in T_{22} mitigate the magnitude of these observables. In addition to the tensor analyzing powers, the vector analyzing powers T^e_{10} and T^e_{11} can be used as an another handle on extracting the form factors. Here, it is T^e_{11} that is dominant even with its interference term of $G_M(G_C+(\tau/3)G_Q)$. This is due to the kinematic factors leading each of these observables.

2.3.3 The Beam-Target Vector Asymmetry

The polarized cross section of equations 2.20 - 2.25 can be cast explicitly in terms of beam, target, and beam-target asymmetries [30]

$$\sigma(h, P_z, P_{zz}) \;=\; \Sigma + h\Delta \;=\; \sigma_0[1 + P_z A_d^V + P_{zz} A_d^T + h(A_e + P_z A_{ed}^V + P_{zz} A_{ed}^T)] \quad (2.32)$$

where σ_0 is the unpolarized cross section, h is the beam polarization, P_z is the target vector polarization, P_{zz} is the target tensor polarization, A_V^d and A_T^d are the target vector and tensor asymmetries, and A_{ed}^V and A_{ed}^T are the beam-target vector and tensor asymmetries. This form, more directly related to experiment, allows one to extract A_{ed}^V for comparison with the form shown in terms of the vector analyzing powers. this will be addressed later in the analysis chapter. For elastic scattering in the OPE approximation, $A_e = A_d^V = A_{ed}^T = 0$ and from the polarized cross section we can define the beam-target vector asymmetry A_{ed}^V.

$$A_{ed}^V \;\equiv\; \frac{\Delta}{\Sigma} \;=\; \sqrt{3}\Big[\frac{1}{\sqrt{2}} \cos\theta^* T_{10}^e(Q^2, \theta_e) - \sin\theta^* \cos\phi^* T_{11}^e(Q^2, \theta_e)\Big] \quad (2.33)$$

In practice one actually measures $hP_z \cdot A_{ed}^V$ where here h and P_z are the beam and target vector polarizations respectively.

2.4 Kinematics

For elastic scattering of an electron with initial(final) four momentum $k(k')$ from a deuteron with initial(final) four momentum $P(P')$, we assume that the target deuteron is at rest in the lab frame and we can write

$$P \;\rightarrow\; (M_d, \mathbf{0})$$

If we then define the three-momentum transfer $\mathbf{q}$ and energy, ω, delivered to the target as

$$\mathbf{q} \;=\; \mathbf{k} - \mathbf{k}' \tag{2.34}$$

$$\omega \;=\; \epsilon - \epsilon' \tag{2.35}$$

Then the four-momentum transfer is

$$q \;=\; (\omega, \mathbf{q}) \tag{2.36}$$

which is just the four-momentum of the transferred virtual photon. In the extreme relativistic limit (ERL) $|\mathbf{k}| \gg m_{e^-}$ the four-momentum transfer for electron scattering is

$$q^2 \;\simeq\; -4\epsilon\epsilon' \sin^2\left(\frac{\theta_{\mathbf{k}\mathbf{k}'}}{2}\right) \qquad (ERL) \tag{2.37}$$

Defining $Q^2 \;\equiv\; -q^2$, we have

$$Q^2 \simeq\; 4\epsilon\epsilon' \sin^2\left(\frac{\theta_{\mathbf{k}\mathbf{k}'}}{2}\right) \qquad (ERL) \tag{2.38}$$

In the case of elastic scattering, conservation of four-momentum yields

$$Q^2 \;=\; 2\omega M_d \tag{2.39}$$

From the above relations, we can now derive the scattered electron energy, ϵ', as a function of electron scattering angle θ_e. Inserting (2.37) and (2.40) into (2.41) we find

$$4\epsilon\epsilon' \sin^2\left(\frac{\theta_e}{2}\right) \;=\; 2(\epsilon - \epsilon')M_d$$

which, after some rearrangement yields

$$\epsilon' \;=\; \frac{\epsilon}{(1 \;+\; \frac{2\epsilon \sin^2(\theta_e/2)}{M_d})} \tag{2.40}$$

Putting the above back into our ERL relation for Q^2 we find

$$\theta_e \;=\; 2\sin^{-1}\sqrt{\frac{Q^2}{(4\epsilon^2 - \frac{2\epsilon Q^2}{M_d})}} \tag{2.41}$$

2.5 Theoretical Models

2.5.1 The Non-Relativistic Deuteron Wavefunction

Since the proton and neutron each carry spin-1/2, these can combine to yield $S = 1$ (triplet) or $S = 0$ (singlet) states [31]. A positive pn scattering length corresponds to a bound triplet in the deuteron ground state with a binding energy of $E_B = 2.2245\ MeV$. The first excited state is a singlet and just unbound by 70 keV (negative scattering length). The triplet state yields possible values of orbital angular momenta of $L = 0$ or 2. The positive parity of the deuteron forbids the $L = 1$ state due to the form of the parity operator $P_L = (-1)^L$.

A positive electric quadrupole moment of $Q_d = 0.2859$ fm^2 indicates that the deuteron is not a spherically symmetric distribution of electric charge, but instead has a prolate (cigar-shaped) deformation. This supports the notion that the deuteron is not in a pure $S(L = 0)$ state but is an admixture of S and $D(L = 2)$ states. The relative contributions of each of these states can be estimated from the deuteron magnetic moment $\boldsymbol{\mu}_D$ which has an observed value of $0.857\mu_N$.

$$\boldsymbol{\mu}_D \;=\; \boldsymbol{\mu}_p + \boldsymbol{\mu}_n + \boldsymbol{\ell}_p\mu_N \;\equiv\; g\mu_N\mathbf{J} \tag{2.42}$$

where

$$\boldsymbol{\mu}_p \;=\; 2.793\boldsymbol{\mu}_N \qquad \text{(proton magnetic moment)} \tag{2.43}$$

$$\boldsymbol{\mu}_n \;=\; -1.913\boldsymbol{\mu}_N \qquad \text{(neutron magnetic moment)} \tag{2.44}$$

$$\mu_N \;=\; eh/2m_p \qquad \text{(the nuclear magneton)} \tag{2.45}$$

$$\boldsymbol{\ell}_p \;=\; \frac{1}{2}\mathbf{L} \qquad \text{(orbital angular momentum of the proton)} \tag{2.46}$$

Assuming a general form for the deuteron ground state wave function of

$$|\psi\rangle \;=\; \alpha|\psi(^3S_1)\rangle + \beta|\psi(^3D_1)\rangle \tag{2.47}$$

where

$$|\alpha|^2 + |\beta|^2 \;=\; 1 \tag{2.48}$$

substitution of $|\psi\rangle$ into

$$\langle\psi|g\mathbf{J}^2|\psi\rangle \tag{2.49}$$

yields a D-state contribution that depends on how one normalizes the wavefunction[7].

The admixture of the $^3S_1$ and $^3D_1$ states due to a tensor component of the NN force essentially means that we are coupling the spin $S = 1$ to orbital angular momenta $L = 0$ and $L = 2$. This gives rise to a wavefunction for the deuteron of the form [1]

$$\psi_M(\mathbf{x}) \;=\; \frac{u(r)}{r}\mathcal{Y}^M_{101}(\theta,\phi) + \frac{w(r)}{r}\mathcal{Y}^M_{121}(\theta,\phi) \tag{2.50}$$

where

$$\mathcal{Y}^M_{JLS}(\theta,\phi) \;=\; \sum_{m_L,m_S}\langle J,M|L,m_L;S,m_S\rangle Y_{LM}(\theta,\phi)|S,m_S\rangle \tag{2.51}$$

[7]The D-state probability is model dependent and thus does not constitute an observable.

are the spin spherical harmonics. $u(r)$ and $w(r)$ are the radial parts of the wavefunction corresponding to the S and D waves respectively. The probability for finding the deuteron in an S or D state found from

$$P_S = \int_0^\infty \rho_S(r)dr \tag{2.52}$$

and

$$P_D = \int_0^\infty \rho_D(r)dr \tag{2.53}$$

where ρ_i is the probability density for the $i = S, D$ state. The deuteron must be in either of these two states, therefore we normalize the wavefunction by requiring

$$P_S + P_D = 1 \tag{2.54}$$

Many potential models exist for the deuteron such as the Reid-SC [32], Paris [33], Bonn [34], CD-Bonn [35], Nijmegen II [36], Reid93 [36], and Argonne v_{18} [37], each yielding a different value for Q_d and P_D. Most potentials yield a D-state probability between 5.6% and 5.8% while the CD-Bonn potential yields P_D =4.83% [1]. Part of the motivation for this work is to further constrain these various models. As an example, we show the reduced radial wavefunctions as a function of the nucleon separation using the Argonne v_{18} potential in Figure 2-6. Note the steep descrease at small r due to the repulsive core. In Figure 2-7, we show the density distributions of the deuteron, as calculated using the Paris potential, for $M = 0$ and $M = 1$ magnetic substates. The repulsive core is seen here as "the hole in the doughnut" of the toroidal density distribution of the deuteron magnetic spin substates. In the non-relativistic impulse approximation (NRIA), we assume that the nuclear current is the sum of the $free$ nucleon currents. In this way, we can write the deuteron electromagnetic form factors in terms of the nucleon form factors and the deuteron reduced radial

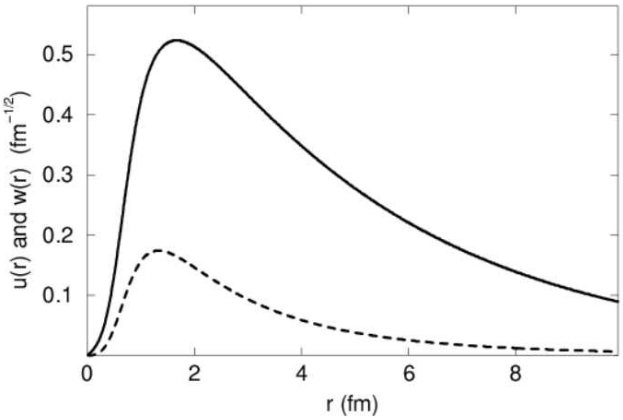

Figure 2-6: Deuteron reduced radial wave functions u (solid line) and w (dashed line) for the Argonne v_{18} potential [1]

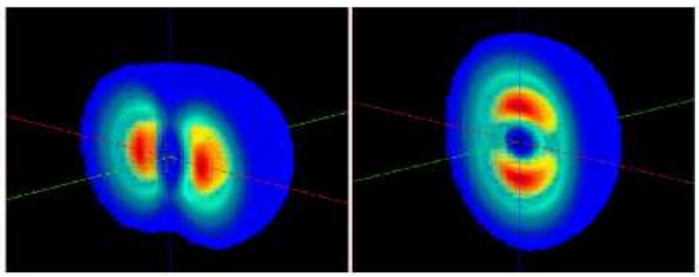

Figure 2-7: Deuteron densities in $M = 0$ (left) and $M = 1$ (right) states for the Paris potential [1]

wavefunctions [38].

$$G_C = (G_E^p + G_E^n) \int \Big[u^2(r) + w^2(r)\Big] \jmath_0\Big(\frac{qr}{2}\Big)\, dr \tag{2.55}$$

$$G_Q = \frac{3}{\tau\sqrt{2}}(G_E^p + G_E^n) \int w(r)\Big[u(r) - \frac{w(r)}{\sqrt{8}}\Big] \jmath_2\Big(\frac{qr}{2}\Big)\, dr \tag{2.56}$$

$$G_M = 2(G_M^p + G_M^n) \int \Big[u^2(r) - \frac{w^2(r)}{2}\Big] \jmath_0\Big(\frac{qr}{2}\Big) + \Big[\frac{u(r)w(r)}{\sqrt{2}} + \frac{w^2(r)}{2}\Big] \jmath_2\Big(\frac{qr}{2}\Big)\, dr$$
$$+ \frac{3}{2}(G_E^p + G_E^n) \int w^2(r)\Big[\jmath_0\Big(\frac{qr}{2}\Big) + \jmath_2\Big(\frac{qr}{2}\Big)\Big]\, dr \tag{2.57}$$

where $j_\ell(qr/2)$ are spherical Bessel functions.

2.5.2 Meson Exchange Currents

The dominant corrections to the NRIA are meson-exchange currents (MECs), isobar configurations, and relativistic corrections [27]. The experiment to measure the vector analyzing powers T_{10}^e and T_{11}^e covers a range of four momentum transfer $Q < 2.5\ fm^{-1}$, that shows little model dependence. This can be seen in the plot of T_{11}^e and of the magnetic dipole form factor G_M from the JLab proposal[8] to measure the vector analyzing power [2] which did not receive approval due to systematic error concerns. Regardless, we will say a few words here for completeness.

The long range part of the nucleon-nucleon (NN) interaction is well understood in terms of a one-pion exchange potential (OPEP). In the medium and short range of inter-nucleon separation, two-pion exchange, as well as the exchange of other mesons such as the ρ and ω become important [21]. The movement of charged mesons gives rise to currents in the nuclear medium. Currents also result from the recoil of a charged nucleon due to interaction with a neutral meson. Also, in our electron scattering process, a virtual photon can couple to a nucleon while that nucleon is interacting with another via meson

[8] In the proposal [2] the polarization observable T_{11}^e is indicated as t_{11} and the form factors G_C, G_Q, and G_M are called G_M, G_Q, and G_D respectively.

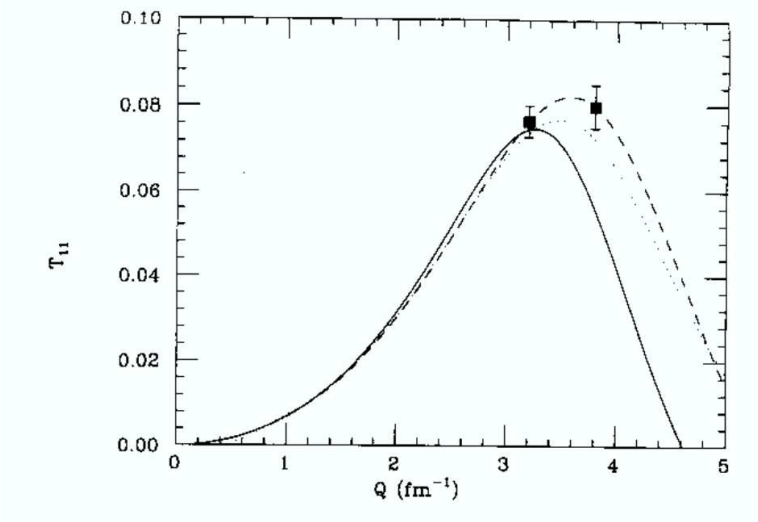

Figure 2-8: Deuteron Vector Analyzing Power T_{11}^e from Proposal PR94-013: (solid) NRIA + MECs, (dashed) realistic magnetic contribution, (dots) RIA with MECs [2]

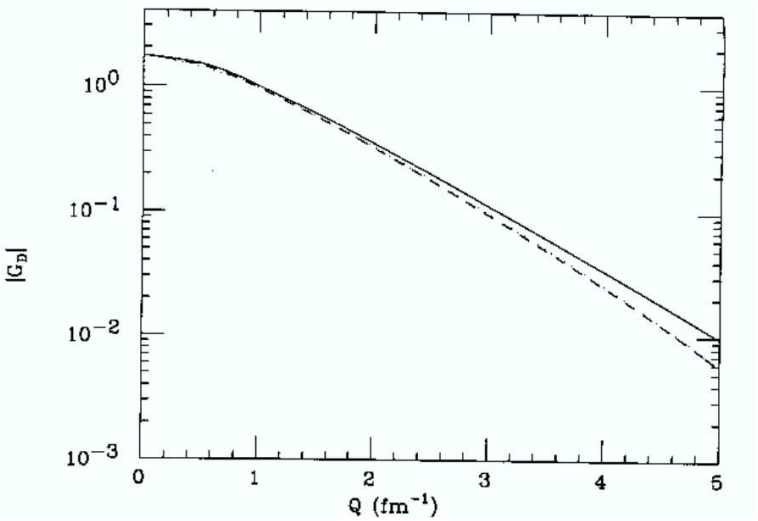

Figure 2-9: Deuteron Magnetic Dipole Form Factor G_M from Proposal PR94-013: (solid) MECs, (dashes) NRIA, (dots) RIA with MECs [2]

exchange. Furthermore, the virtual photon can couple to the exchanged meson itself. The MEC adjustment of the NRIA has been calculated for π, ρ, ω pair term and for the $\pi\rho\gamma$ exchange by Gari and Hyuga [39]. The diagrams for these processes are shown in Figure 2-10a-c with the darkened circles representing form factors for the interaction vertices. Since the deuteron is an isospin-zero object, there is no isovector 2-body current contribution in these interactions. However, the structure function $B(Q^2)$, for example, is sensitive to isoscalar contributions from model-independent two-body currents as well as the model dependent $\pi\rho\gamma$ term [17]. Relativistic corrections to the impulse approximation (RIA)

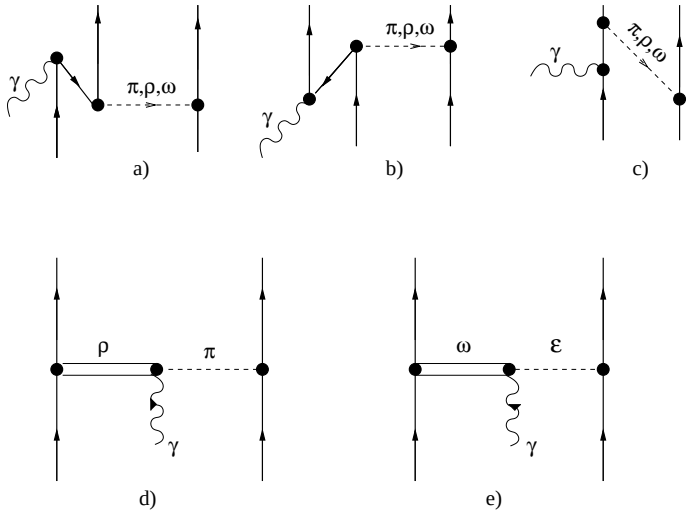

Figure 2-10: Meson-exchange current diagrams: a), b) pair terms, c) recoil, d) $\rho\pi\gamma$ term, e) $\omega\epsilon\gamma$ term

were found to have a significant effect with respect to the contribution of the $\omega\epsilon\gamma$ graph to the deuteron magnetic form factor [40]. However for low momentum transfer, the deuteron properties and elastic electromagnetic form factors are both predicted with similar results by the RIA and non-relativistic potentials such as the Reid Soft Core (RSC) potential [40]. Overall, the magnitude of model dependence of the deuteron structure functions $A(Q^2)$ and $B(Q^2)$ decreases with decreasing momentum transfer.

CHAPTER 3

Experimental Apparatus

The experiment was performed at the William F. Bates Linear Accelerator Center in Middleton, Massachusetts. This facility is funded by the U.S. Department of Energy and operated by the Massachusetts Institute of Technology. The many components of the magnetic spectrometer were developed by the multi-institution BLAST Collaboration [41] for the simultaneous detection of electrons, protons, neutrons, deuterons, and pions comprising the constituents of the many BLAST reaction channels. The combination of an intense polarized electron beam, a polarized internal target, and a relatively large acceptance detector, is rather unique in the world of intermediate energy nuclear physics. This chapter serves to provide a overview of these elements as well as the BLAST Data Acquisition System.

3.1 The MIT-Bates Linear Accelerator

A longitudinally polarized electron beam was delivered to the BLAST detector by the MIT-Bates Linear Accelerator. Low energy polarized electrons were injected into the linac and accelerated to an energy of up to 500 MeV. These electrons then make a second pass through the linac by way of a recirculator, thereby increasing the energy of the beam up to ∼1 GeV. The BLAST experiment used beam with an energy of 850 MeV. After leaving the recirculator, a switchyard guided the beam to various possible experimental areas. In this experiment, the beam was injected into the Bates South Hall Ring (SHR). The

beam was then circulated through the BLAST polarized internal target and spectrometer located in the Bates SHR.

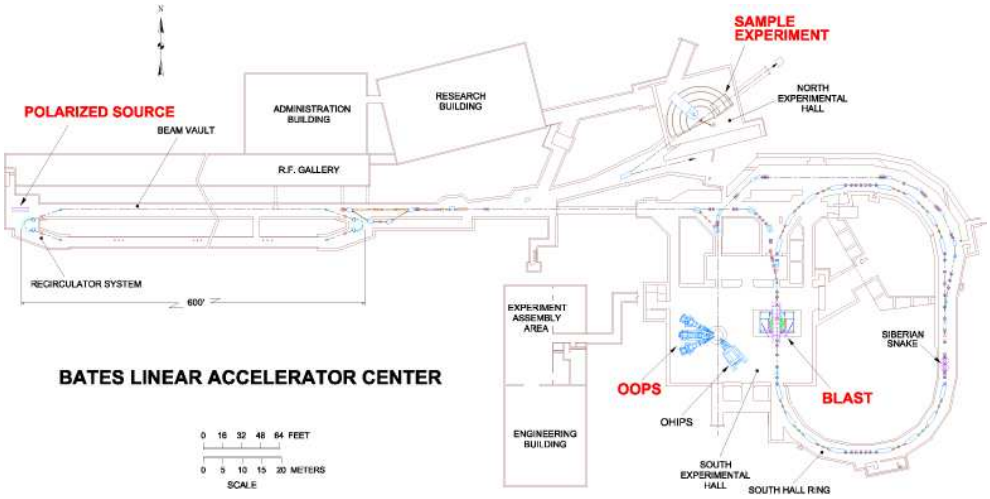

Figure 3-1: Plan View of the MIT-Bates Linac

3.1.1 The Polarized Source

The Bates polarized electron source consists of a stressed gallium arsenide (GaAs) crystal upon which circularly polarized laser light is shone [42]. The wavelength of the incident laser light must be on the order of the bandgap in the crystal so as to excite the valence electrons to the conduction band. Lowering the work function of the GaAs by building a surface dipole with Cesium and an oxidant then makes it possible for the electrons in the conduction band to escape. The emitted photoelectrons must have their spins polarized to satisfy conservation of angular momentum. These electrons are fed into the linac for acceleration to the proper energy of the experiment. A 1/4-λ waveplate was inserted into and withdrawn from the laser path to flip the helicity of the emitted

photoelectrons once per each fill of the electron storage ring[1]

3.1.2 The Bates South Hall Ring

The BLAST spectrometer and polarized target are installed into the west straight section of the Bates South Hall Ring. With an internal target experiment, the Bates SHR is designed to operate as a storage ring. For external targets, the ring is operated in pulse-stretcher mode to convert the low duty factor beam supplied by the linac to near continuous wave beam [42]. Injection currents as high as 225 mA with lifetimes on the order of 25 minutes have been achieved with an energy of 850 MeV with the deuterium internal target thicknesses required by the experiment. The current is measured by a parametric current transformer (DCCT) which operates essentially as a pickup coil.

Ultra relativistic electrons have polarization in the longitudinal direction alone but the spin of these electrons will precess about the momentum due to the g-2 anomaly [43]. To counteract this precession, a pair of superconducting solenoids, called Siberian Snakes [42], orient the spins such that they precess to the desired direction upon reaching the BLAST target. The Snakes are located in the east straight section of the South Hall Ring.

Diagnostics of the beam halo consist of Versa Module Europa (VME) scaler readbacks from the BLAST wire chambers as well as a set of four photomultiplier tubes, collectively called the beam quality monitors (BQMs), strapped about the beampipe in a symmetric fashion downstream of the target. Beam halo in the target area is mitigated through the use of collimators as well as four independently adjustable beam scrapers, located at a point of high β in the ring[2]. The scrapers are adjusted with stepper motors such that a minimum rate was seen on the halo monitors up until the point of reducing the beam

[1]The Bates South Hall Ring is described in the next section. The ring was filled, and the helicity of the beam was flipped, once every ∼10-20 minutes approximately depending on running conditions.

[2]β is a solution to the equation governing the optics of the storage ring. It describes a sausage-like envelope that is defined by the trajectories of successive orbits of a single particle in the ring.[44]

lifetime. The slow controls system Experimental Physics and Industrial Control System (EPICS) provides the means of user interface and controls for much of the beam hardware and diagnostics.

3.1.3 The Compton Polarimeter

Polarization of the stored beam is monitored by Compton backscattering of laser light from the electrons circulating in the ring. The backscattered photons have a trajectories constrained to a tight cone about the electron beam axis due to the very high momentum of the electron beam [45]. This allows for a relatively small acceptance detector to collect them. The incident 532 nm laser light is frequency shifted by the back scattering to gamma ray energies. A cesium iodide calorimeter was used to measure photon energy as well as count rate. The cross section for Compton scattering depends, to some extent, on the polariztion of the electron beam as well as the polarization of the incident laser light [45]. This characteristic allows the compton scattering rate to be used as a diagnostic in electron beam polariztion measurements. Specifically, by flipping the helicity of the laser with a Pockels Cell, an asymmetry can be measured in the intensity of the backscattered photons. This asymmetry is directly proportional to the product of the laser and electron beam polarization. A beam chopper allows for a measurement of background while sweeper magnets ensure that no charged particles reach the calorimeter [45]. Average beam polarization as measured with the Compton Polarimeter was on the order of $65 \pm 4\%$.

3.2 The Polarized Internal Target

The polarized internal target system at Bates was based on an atomic beam source (ABS) design that was employed at the NIKHEF laboratory [46]. The ABS provided an intense polarized atomic beam to a windowless storage cell through which the circulating

electrons of the Bates South Hall Ring passed. ABS operation was maintained through EPICS slow controls.

3.2.1 The Atomic Beam Source

Molecular hydrogen or deuterium is converted to its respective atomic species via a RF dissociator. The resulting atomic beam is polarized via a Stern-Gerlach apparatus and polarization is transferred to the nucleus through transitions between hyperfine states split by the Zeeman effect [47]. The hyperfine states of deuterium are shown in Figure 3-2. The

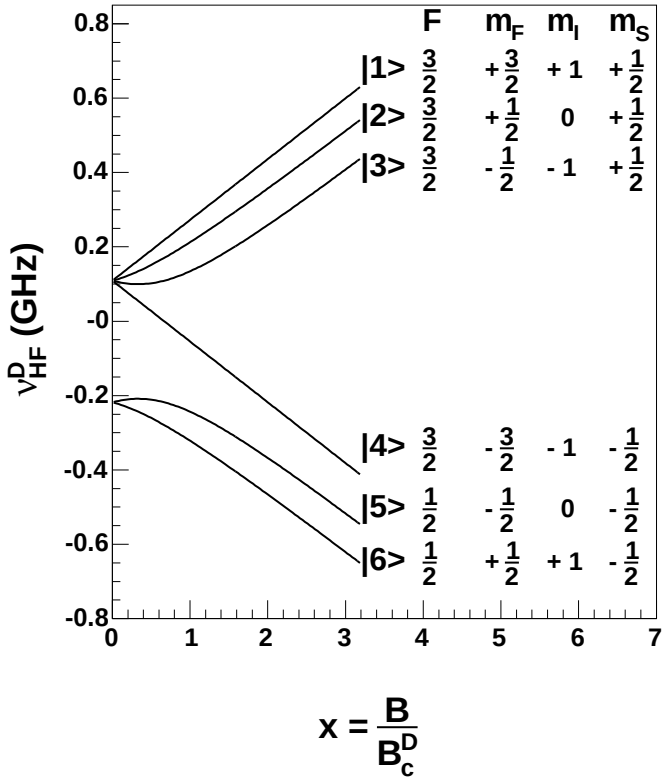

Figure 3-2: Hyperfine States of Deuterium

BLAST ABS, shown schematically in Figure 3-3, can essentially be divided into five parts,

each with a separate pumping system. The first stage contained the dissociator chamber and skimmer chamber. It was here that the atomic beam, consisting of all hyperfine states $|1\rangle$ through $|6\rangle$, was formed. The second stage contained the first set of sextupole magnets which performed a Stern-Gerlach separation of the lower hyperfine states ($m_j = -1/2$) so that only states $|1\rangle$, $|2\rangle$, and $|3\rangle$ remained in the atomic beam [47]. In the case of states V± in which the deuteron vector polarization is $P_z = \pm 1$ (ideally 100% polarization), a RF mean field transition (MFT) in the third stage took those atoms in hyperfine state $|3\rangle$ to state $|4\rangle$. The fourth stage contained the second set of sextupole magnets which filtered out these new lower hyperfine state $|4\rangle$ atoms. For production of the $V+$ state a strong field transition (SFT) followed taking state $|2\rangle$ to state $|6\rangle$ so that states $|1\rangle$ and $|6\rangle$ were injected into the storage cell. In the case of $V-$ a weak field transition (WFT) took states $|1\rangle$ and $|2\rangle$ to $|4\rangle$ and $|3\rangle$ respectively which were then injected into the storage cell. Further pumping occured in the fifth stage to reduce background in the target cell. A summary of the target states, including those required for tensor polarization $\pm T$, is shown in Table 3.1[3]

	Vector +	Vector -	Tensor +	Tensor -
MFT	3-4	3-4	1-4	1-4
SFT	2-6	Off	2-6	3-5
WFT	Off	1-4, 2-3	Off	Off
States	$\|1\rangle + \|6\rangle$	$\|3\rangle + \|4\rangle$	$\|3\rangle + \|6\rangle$	$\|2\rangle + \|5\rangle$
P_z	+1	-1	0	0
P_{zz}	+1	+1	+1	-2

Table 3.1: Operating Modes of the BLAST Polarized ABS Target

[3]See Figure 3-2 for a description of the deuteron hyperfine states.

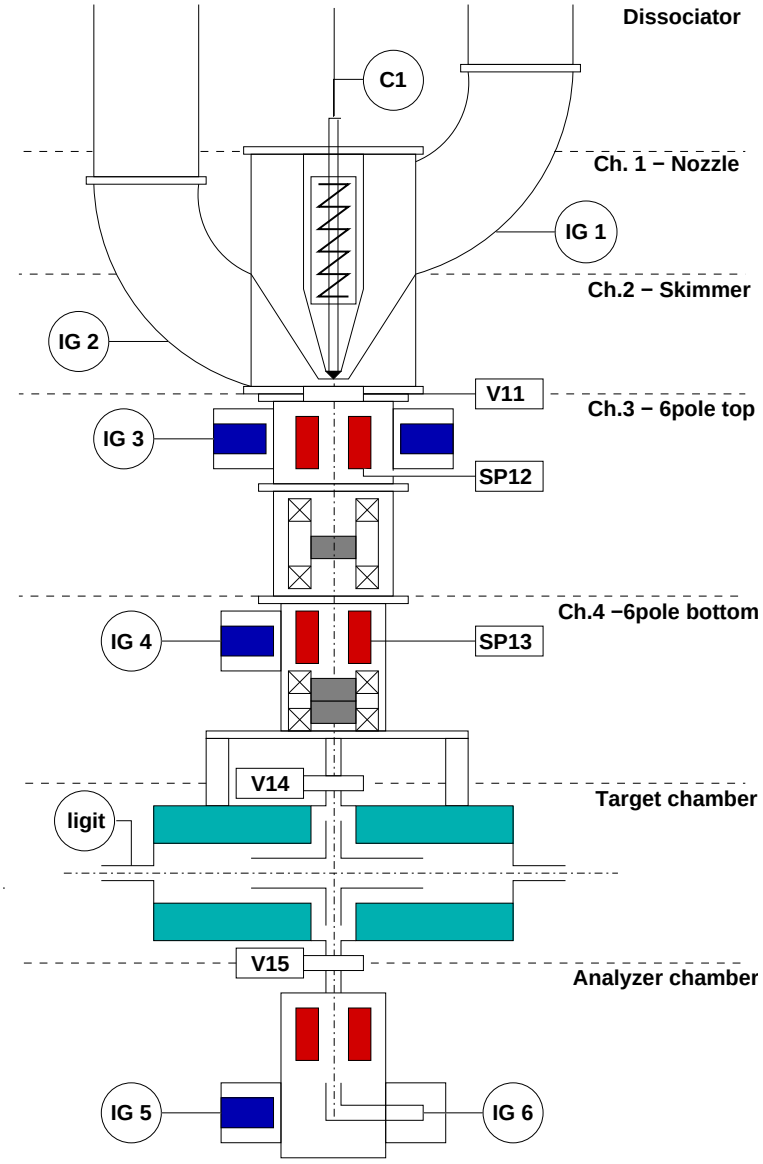

Figure 3-3: The BLAST Atomic Beam Source: Gas is injected into the dissociator C1. Valve V11 separates the skimmer chamber from the first sextupole unit, SP12, which is then followed by the MFT transition unit. The SFT and WFT units as well as the second sextupole system are in the same vacuum chamber. The target chamber is separated from the ABS by valve V14. A Breit-Rabi polarimeter vacuum chamber is located under the target chamber and separated by valve V15. All valves are remotely controlled and all vacuum chambers are equipped with ionization gauges. [3]

3.2.2 Target Storage Cell and Scattering Chamber

The ABS delivers the polarized atomic beam to a storage cell. Once in the storage cell, a magnetic holding field maintains the nuclear polariztion. This field has longitudinal and transverse components that have magnitudes from 0-50 mT and 0-25 mT respectively. In this experiment, the target vector was set 32° and 47° beam-left in the BLAST xz-plane (parallel to the South Hall floor). The beam entered and exited the storage cell through a windowless aperture thus making the target undiluted in this regard. The use of a storage cell increases the target thickness by the order of a factor of 100 [47] due to the time it takes for atoms to drift out of the target region. Cell lengths of 40 cm and 60 cm, both with a diameter of 15 mm, were used in this experiment.

A variety of factors can influence polarization of the target. Spin exchange reactions through collisions with beam dilutants or the cell wall are primary culprits in reducing target polarization. To reduce depolarization due to wall collisions, the cell was coated with a layer of Drifilm [48]. The lack of available bonds in this layer decreased the probability of binding atoms to the wall [3]. Typical values of vector polarization in the BLAST ABS were $P_z \simeq 78\%$.

3.3 The BLAST Detector

The Bates Large Acceptance Spectrometer Toroid (BLAST), is a relatively large acceptance detector that is designed to measure double polariztion asymmetries. The design of the BLAST detector consists of an eight sector copper coil array which produces a toroidal magnetic field, instrumented with two opposing wedge-shaped sectors of wire chambers, scintillation detectors, Čerenkov counters, and neutron detectors. The open geometry maximizes acceptance while allowing good momentum and angular resolution and a count rate capability matched to the projected luminosity of the polarized internal target and beam [43].

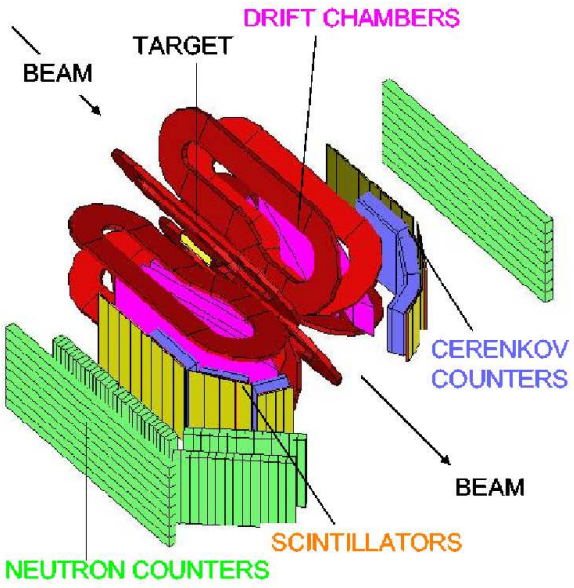

Figure 3-4: The BLAST Detector

3.3.1 The BLAST Magnetic Field

To determine the charge and momenta of the various reaction products, a strong magnetic field was required in the region of the drift chambers. Eight room temperature copper coils arranged symmetrically about the SHR electron beam axis provide a toroidal non-focusing magnetic field that varies as $B(r) = B_i r_i / r$ where r_i is the inner radius of the torus. The eight coil design has 1.4 MA-turns that yield a $\int \mathbf{B} \cdot \mathbf{d}\ell$ that meets the required momentum resolution of the experiment [43]. Furthermore the toroidal field configuration provides a field-free target region so that the target holding field and incident electron beam are not adversely affected. Twenty six turns per coil with a maximum current of 6730 A achieve $\int \mathbf{B} \cdot \mathbf{d}\ell$ values bewteen 0.6 and 0.2 T-m as well as field gradients less than 0.05 G/cm in the target $\pm$15 cm region [43]. Plots of the azimuthal field B_ϕ versus radial and axial distance from the target are shown in Figure 3-6 and Figure 3-7.

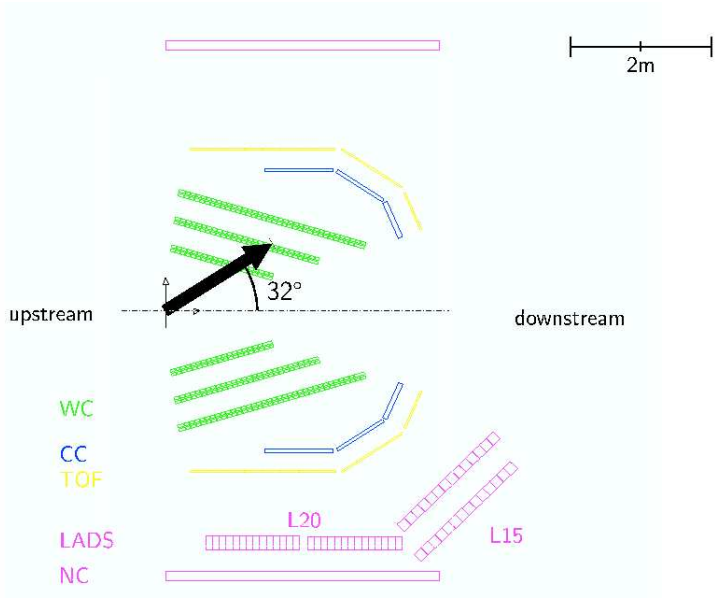

Figure 3-5: Plan View of BLAST Detector (showing Target Angle)

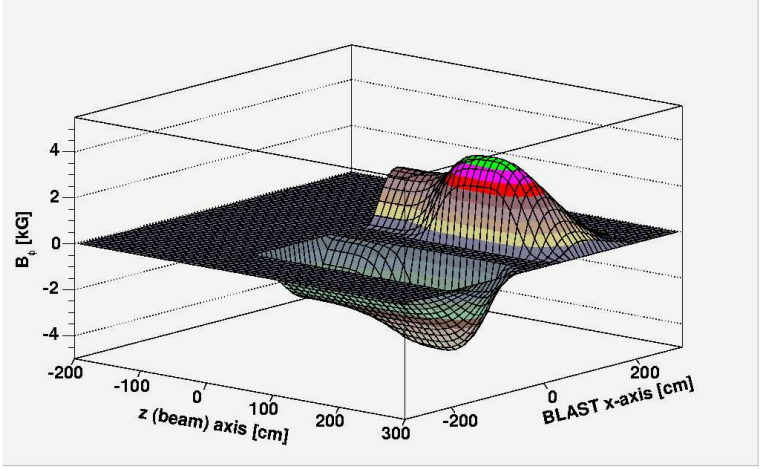

Figure 3-6: BLAST Field in 3-D

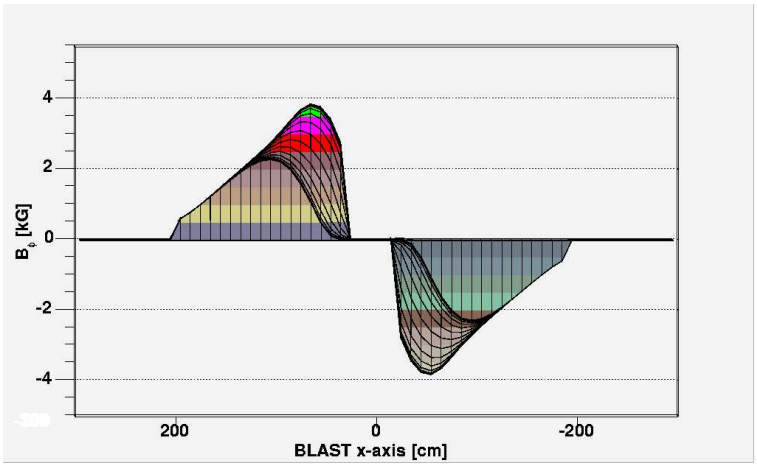

Figure 3-7: BLAST Field (downstream view)

3.3.2 Time-of-Flight Scintillators

The BLAST Time-Of-Flight Scintillators (TOFs), shown in yellow in Figures 3-4 and 3-5 provide fast timing information and triggering for charged particle identification as well as for neutron veto. Sixteen TOFs cover a scattering angle range of $20° < \theta < 80°$.[4] The forward angle TOFs at $\theta < 40°$ are 119.38 cm in length, 15.24 cm wide, and 2.54 cm thick while the backward angle TOFs at $\theta > 40°$ are 180.00 cm long, 26.2 cm wide, and 2.54 cm thick. The TOFs were designed to cover the drift chamber angular acceptance. The TOFs are made from Bicron[5] BC-408 plastic scintillator which was chosen because of its fast response time and long attenuation length, as well as the structural characteristics of plastic.

In organic scintillators, the emitted photons result from excitations of the electron and molecular vibrational levels by incident radiation. These transitions are undergone by the $free$ valence electrons of the scintillator material molecules. These electrons are not

[4]Four additional Backward-angle TOFs (BATS) in each sector of BLAST provide additional polar angle coverage from 90° to 120° but without drift chamber correlation.

[5]Bicron, 12345 Kinsman Rd, Newbury, OH 44065 USA

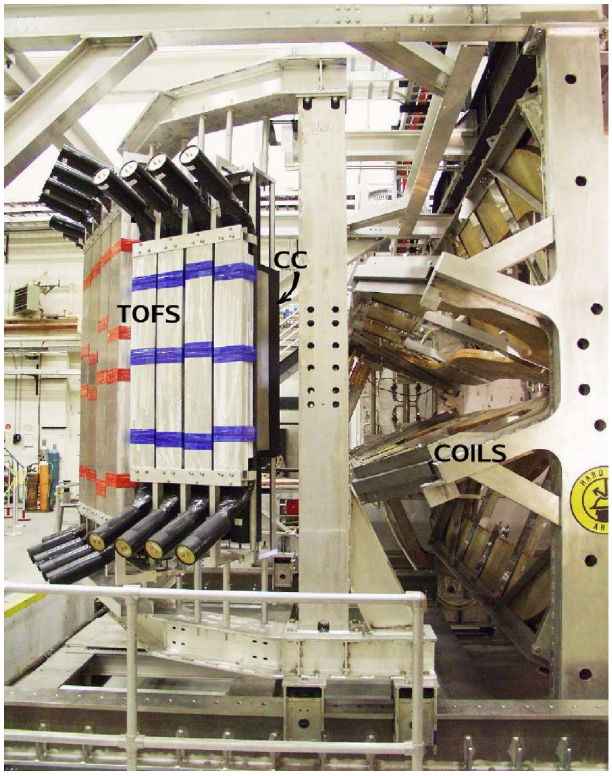

Figure 3-8: Upstream View of BLAST Right Sector TOFs and Coils

Base	Polyvinyltoluene
Refractive Index	1.58
Rise Time (ns)	0.9
Decay Time (ns)	2.1
Pulse Width, FWHM (ns)	$\sim$2.5
Attenuation Length (cm)	210
Peak Wavelength (nm)	425

Table 3.2: Properties of Bicron BC-408 Organic Plastic Scintillator

associated with any particular atom in the molecule but instead populate the π-molecular orbitals which bond adjacent benzene rings [49]. The scintillation process has a fast and slow component in the number of photons emitted per event as described by [50]

$$N \;=\; Ae^{-\frac{t}{\tau_f}} \;+\; Be^{-\frac{t}{\tau_s}} \tag{3.1}$$

Here τ_f and τs are the fast and slow decay constants respectively and A and B are material dependent factors that are a function of total number of photons emitted. Excitation and relaxation of π-electron singlet states gives rise to the fast component while recombination into the π-electron triplet states is the source of the slow component [49]. In BC-408 the fast component dominates. Both components, however, have relatively fast rise times with the net rise time totally limited by choice of photomultiplier tube (PMT).

The time resolution of the TOFs was determined, using the method of Giles [51] as discussed in Chapter 4, to be approximately 350 ps FWHM which is well below the BLAST design specification of 500 ps FWHM. This fast timing characteristic is essential for applying narrow coincidence timing cuts, a good definition of coplanarity for elastic events, and a high resolution for the drift chamber TDCs. The specifications for BC-408 are listed in Table 3.2 [52].

A Lucite lightguide on each end of each TOF bar channels the photons of each event through a joint made with optical quality glue of the matching index of refraction, to

a 3 in diameter Electron Tubes[6] PMT (Model 9822B02). The lightguides are curved in such a way as to orient the PMT perpendicular to the BLAST magnetic field to facilitate magnetic shielding. A highly permeable magnetic shield (Mu-Metal) is placed around each PMT such that the shielding extends at least one diameter past the photocathode. The entire TOF bar assembly is wrapped in opaque kapton to create a light tight environment.

The base electronics unit for each PMT consists of an actively stabilized voltage divider (Electron Tubes: Model EBA-01) which supplies the high voltage to the PMT and the output signal of the PMT to the data acquisition system [43]. This divider network contains four high voltage field effect transistors (FET) which stabilize but do not fix the voltage across the last four sections of the tube. To maintain the high quality of timing required, the voltage between the photocathode and the first dynode is set with a zener diode. This effectively makes the timing independent of the tube gain [43].

In addition to timing information, scintillators provide a measure of energy deposited by incident radiation. Above a certain minimum, scintillators behave in a linear fashion with respect to energy deposited such that the number of photons emitted is proportional to this energy [50]. Since the photomultiplier tube on the end of the scintillator also behaves in a linear fashion, the TOF assembly can be used as a crude calorimeter. Minimum ionizing particles such as electrons can be distinguished from deuterons which deposit significantly larger amounts of energy.

A discussion on the performance of the time-of-flight scintillator system occurs in Chapter 4.

3.3.3 Drift Chambers

Between the TOFs and the target are a set of wire chambers that provide tracking information for charged particles. These wedge shaped detectors fit between two of the

[6]Electron Tubes Limited, Bury Street, Ruislip, Middlesex, HA4 7TA, England

main field coils in two opposing sectors of BLAST and cover a polar range of $20^\circ < \theta < 80^\circ$ and $\pm 17.5^\circ$ in azimuth ϕ. A strong electric field gradient produces a "jet-drift" configuration which is maintained inside each chamber by various field and guard wires [53]. These jets, shown in Figure 3-9, each terminate on a sense wire. Ionization of the chamber gas due to charged particles produces electrons which drift along these jets toward these sense wires and produces a *hit*. Time-to-distance relationships, obtained phenomenologically [54], were made to determine the trajectory of the incident particle. Each chamber is divided into two "superlayers" each of which contains three layers of

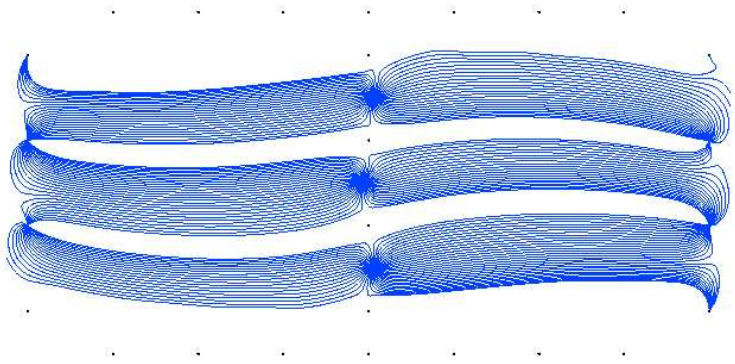

Figure 3-9: Drift Chamber Electric Field (in 3 kG magnetic field)

sense wires. If three consecutive sense wires are hit a *stub* is formed. The sense wires are staggered to disciminate against false stubs. Furthemore, a stereo angle of $\pm 5^\circ$ is alternated every other layer [53]. This allows for determination of the height of the stub so that a *segment* can be formed. Groups of stubs in adjacent layers are called *clusters*. In the jargon of reconstruction, hits form stubs, stubs form clusters, clusters form segments, and segments form tracks.

Each sector of BLAST has three chambers which share a single gas volume. The chamber gas mixture used was 82.3% helium and 17.7% isobutane [55]. This helium reduces the probability for multiple scattering while the isobutane provides a species with

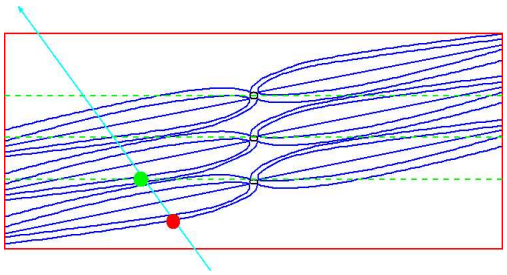

(a) Time-to-distance function calculates the perpendicular distance of the track from the wire.

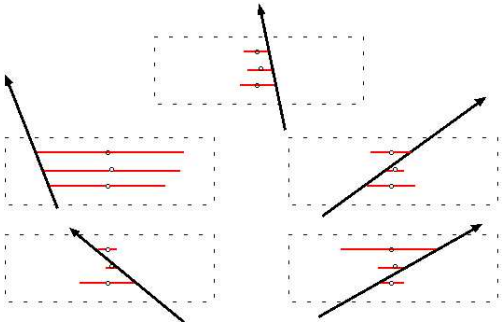

(b) Stub-finder determines which side of each wire the track passed.

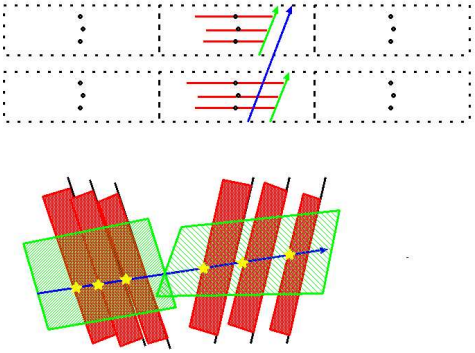

(c) In each chamber, the intersection of two stubs planes forms a line segment.

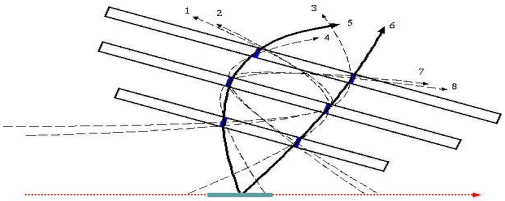

(d) The line segments are linked to form the most likely tracks.

Figure 3-10: Steps of track reconstruction from hits in the drift chambers.

low ionization potential [56]. The entrance window is composed of two thin sheets of mylar, also to reduce multiple scattering. The gap between the mylar sheets is purged with nitrogen to protect phototubes on the adjacent detectors from helium poisoning [56]. The exit window is similarly flushed but also has a thicker acrylic window.

3.3.4 Čerenkov Detectors

BLAST has four Čerenkov counter (CC) boxes in each sector for the identification of relativistic particles, primarily to allow discrimination between electrons and pions. Each

box contains a section of optically transparent aerogel[7] and a section that serves as a light collection chamber. The Čerenkov radiation produced in the aerogel is incident upon a diffusively reflective surface[8] and is collected by 5 in. Photonis[9] phototubes (Model XP4500B).

The choice of the index of refraction, n, of the aerogel was driven by pion momentum thresholds [43]. A balance was struck between complete pion rejection and sufficient light output for ultra-relativistic ($\beta \simeq 1$) electrons. Simulations indicated that single pion photoproduction cross sections of the scattering of 880 MeV electrons from ^3He yielded a pion momentum $\geq$ 600 MeV/c only at scattering angles less than 40° [43]. This led to a selection of $n = 1.02$ aerogel for the forward angle range of $20° - 40°$ and $n = 1.03$ in the backward angle range of $40° - 80°$.

Forward of 35° the BLAST coil shadow limited the size of the Čerenkov box to match the forward angle TOF length. The backward angle boxes are progressively larger and correspond to the backward angle TOF lengths. The smallest box covers $20° < \theta < 35°$ and contains 6 PMTs, the middle-size box covers $35° < \theta < 50°$ and contains 8 PMTs, and the largest box covers $50° < \theta < 70°$ and contains 12 PMTs [57]. The initial BLAST design called for a Čerenkov box covering the last section of TOFs out to 80° but this box stopped the majority of deuterons in this region and was relocated to the inboard side of the Backward Angle TOFs (BATs).

3.3.5 Neutron Detection

Neutron detection with BLAST is accomplished with two sets of scintillation detectors composed of Bicron BC-408. The first of these sets, called the neutron counters (NC)

[7] Matsushita Electric Works Ltd. 1048 Kadoma, Osaka, Japan

[8] LabSphere, 231 Shaker Street, North Sutton, New Hampshire, USA

[9] Photonis, Avenue Roger Roncier, Z.I. Beauregard, B.P. 520, 19106 BRIVE Cedex, France

were fabricated by Ohio University and contain two walls of eight rectangular bars. These are configured horizontally with an Electron Tubes type phototube on each end. The bars have dimensions of 22.5 cm $\times$400 cm $\times$10 cm [58]. The greater thickness of these bars, as compared with the TOFs, is required for greater neutron detection efficiency. The NC walls are the outermost detector segment of BLAST and cover a range in scattering angle of $45^\circ < \theta < 90^\circ$.

The Large Acceptance Detectors (LADS), manufactured by PSI and MIT, are four walls of fourteen bars of trapezoidal cross section. These are arranged in a vertical fashion and reside in the right sector of BLAST only just inboard of the NC wall. Two of these walls have the dimensions 13.7 cm $\times$ 160 cm $\times$ 15 cm and the other two have the dimensions 9.3 cm $\times$ 160 cm $\times$ 20 cm [58]. The former are doubled up with repsect to the radial distance from the target forward of 40° while the latter form a near continuous wall covering $40^\circ < \theta < 80^\circ$.

The longer flight path of the NC and LADS walls from the target as opposed to the other detectors, the greater thickness, as well as veto capability from the drift chambers and TOFs, form the basis of neutron detection with BLAST.

3.4 Data Acquisition System

Analog signals from the PMTs and the wire chambers travel via long ($\sim$ 58 m) RG58 coaxial cables to the BLAST data acquisition system (DAQ). For each sector in BLAST, there is a LeCroy[10] computer automated measurement and control (CAMAC) crate containing various programmable emitter coupled logic (ECL) modules that form the first level hardware trigger. A VME crate contains a scaler for each channel as well as coincidence circuits in addition to a CES[11] CBD8201 branch driver for communication with

[10]LeCroy Corporation 700 Chestnut Ridge Road, Chestnut Ridge, NY

[11]Creative Electronic Systems, Grand-Lancy, Switzerland

the CAMAC crates. A second level trigger requiring good wire chamber tracks greatly improves the quality of recorded data. A trigger supervisor (TS) combines the first and second level trigger and provides gates and starts for analog-to-digital converters (ADCs) and time-to-digital converters (TDCs).

3.4.1 BLAST Trigger Electronics

Prior to entering the trigger logic the TOF and NC PMT signals are sent through a passive analog splitter. The analog signals from the Čerenkov PMTs are combined in a CAEN[12] N402 analog adder prior to being sent to the splitter. One output, called the prompt, is sent directly to the trigger logic, while the other is delayed by 500 ns before being sent to the ADCs. The prompt signals from the TOF and Čerenkov counters are fed into LeCroy constant fraction discriminators (CFDs) while those of the NC and LADS are sent to LeCroy leading edge discriminators (LEDs). After the discriminators, various modules are in place to demand coincidence of two PMTs in each TOF, NC, or LADS bar, or to delay and fan out signals to TDCs and the VME scalers [59]. These details are illustrated in the trigger schematic. All detector group signals are fed into a sector LeCroy memory lookup unit (MLU) which enable programmable user-defined trigger bit patterns. The sector MLU outputs are combined in a cross-sector memory lookup unit (XMLU).

The ECL output of the XMLU is converted to NIM logic and then enters the trigger supervisor. The TS is a custom module, designed and built at TJNAF, that manages trigger type distribution, prescaling, and busy/inhibit signals [59]. To simplify the wire chamber analysis, two timing solutions are in place. First, a CAEN mean timer module makes TOF timing independent of azimuthal angle ϕ about the beam. Second, a delayed LeCroy 4564 OR registers TRUE for the first of any TOF hit providing a common strobe

[12]CAEN S.p.A. Via Vetraia, 11 55049 - Viareggio (LU) - ITALY

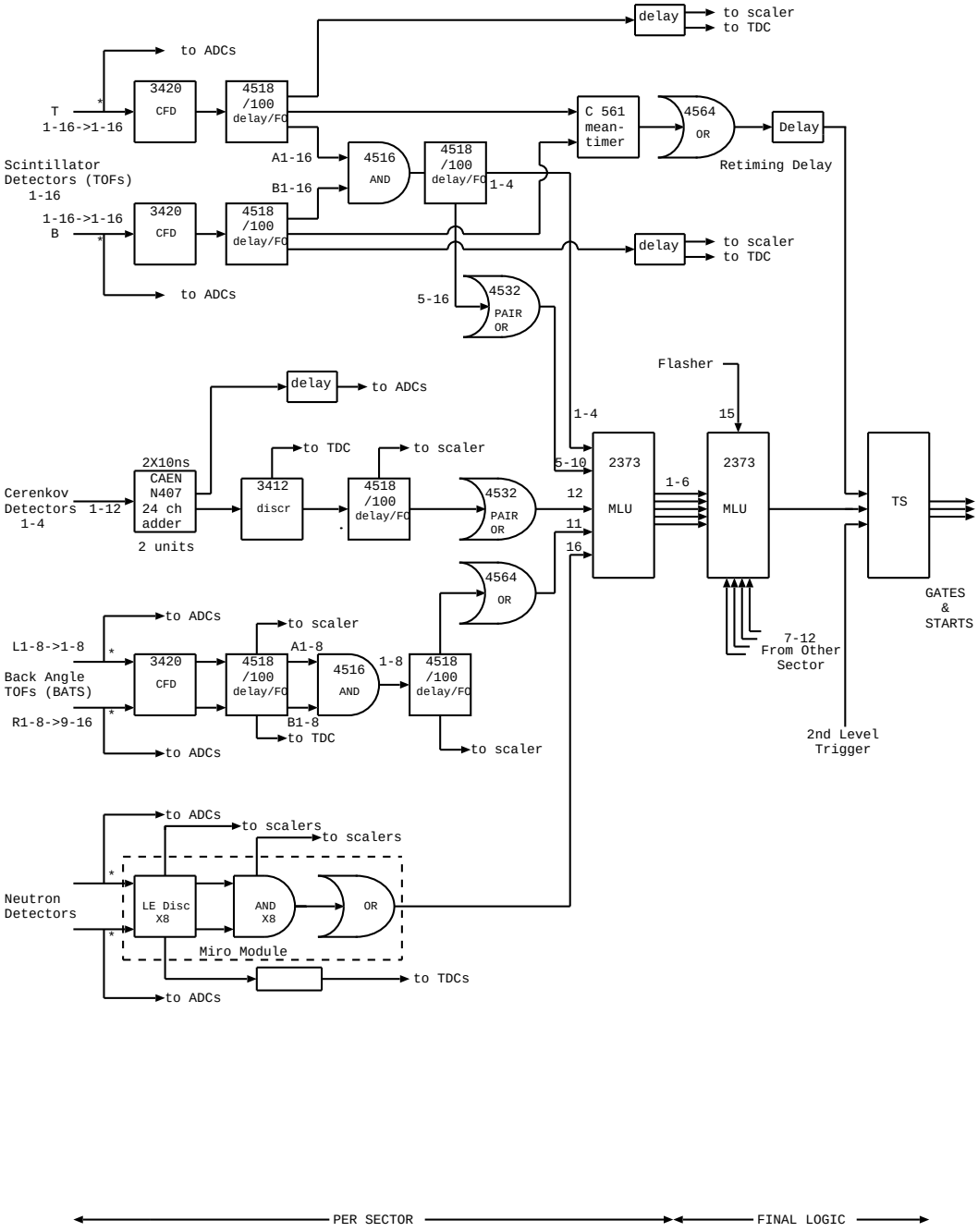

note: * all analog signal division in matched impedance passive splitters

Figure 3-11: BLAST Trigger Electronics

to the TS and making TOF timing independent of path length from the TOF to the target.

3.4.2 The Second Level Trigger

To increase the fraction of recorded data with good wire chamber information, a second level trigger was developed. Wire chamber information coming from the LeCroy 1877 TDCs via custom boards provides a TTL logic signal for groups of sixteen wires. A "sector WC hit" is TRUE only if there is a hit in the inner, middle, and outer chamber of the sector. Two sector boards can be run through an OR or an AND logic although the former is more applicable to the wide array of BLAST reaction channels. A TTL output for a good WC hit is converted to NIM and enters a NIM AND module with a first level trigger signal from the TS. The second level trigger cut the recorded event rate by a factor of ten [59].

3.4.3 TDCs, ADCs, and the ROC

The trigger supervisor provides gates and starts to LeCroy 1801M ADCs and 1875a TDCs for the phototube detectors respectively, while providing a common start for the WC TDCs. While the 400 ns ADC gate is open, detector current is integrated, and the charge is converted to ADC channel with a nominal calibration of 50 fC/ch. The calibration for the TDCs is 50 ps/ch. The ADC and TDC modules of each sector are housed in a Struck[13] Fastbus crate.

Motorola[14] MV162 single-board computers serve as readout controllers (ROCs) in each of the Fastbus crates [59]. Each ROC is housed in a VME to Fastbus interfacce called a Struck Fastbus Interface (SFI). Each ROC has an IP address by which it communicates

[13]Struck Innovative Systeme, Harksheider Str. 102A 22399, Hamburg, Germany

[14]Motorola Inc., 1303 E. Algonquin Road, Schaumburg, Illinois, USA

with an end user via ethernet.

3.4.4 CODA Data Acquisition Software

The Common Online Data Acquisition (CODA) application is the software for the BLAST DAQ. CODA, which was developed at TJNAF, reads data from the front end digitizers (ADCs and TDCs), builds events, and records data to disk. The user interface for CODA is a graphical user interface (GUI) called RunControl. RunControl allows the user to set trigger supervisor configurations for various types of data taking.[15] The ROCs pass data fragments to the Event Builder (EB) module of CODA which verifies that all fragments are of the same trigger type [59]. The EB then passes data to the Event Transport (ET) which allows for various actions such as online spying on the data or insertion of scaler and EPICS information into the data stream. The Event Recorder (ER) commincates with the Event Builder and writes the raw data, again consisting only of ADC and TDC information at this point, to disk.

[15] Programming of the CAMAC trigger hardware is done through a separate application.

CHAPTER 4

Performance of the Experiment

A double polarization measurement of the beam-target vector asymmetry A_V^{ed} requires the electron beam and internal target to each have high polarization and intensity. To extract the vector analyzing powers T_{10}^e and T_{11}^e a comparision of the left and right beam-target vector asymmetries was made. This comparison depends directly upon the symmetry of BLAST and on the performance of detector sub-systems. Initial proposal requirements for the various BLAST reaction channels specified an average ring current of 80 mA, a longitudinal beam polarization of h ∼80%, and a target vector polarization of P_z ∼50% [60]. It is the product hP_z, however, that is important and over the course of the experiment values comparable $hP_z \sim 0.4$ were achieved.

4.1 Performance of the Electron Beam

4.1.1 Beam Current and Lifetime

To achieve the desired statistics for the experiment, and hence the most efficient running mode, the beam fill cycle for the South Hall Ring was optimized. To this end, the maximum injection current into the ring, I_{max}, and the beam lifetime, τ, provided a basis for setting the cutoff current I_{cutoff}, at which the beam in the ring is dumped and the ring is refilled again by the linac. Assuming an exponential behaviour of the beam current we have the current at time t as

$$I(t) \;=\; I_{max} e^{-t/\tau} \tag{4.1}$$

Defining the down time, t_{down}, as the time to ramp down the detector high voltages, inject the beam into the ring, and then ramp the high voltage back up to operating levels, one can then determine the data acquisition time, t_{DAQ}, required to maximize the average current [61]. This is

$$t_{DAQ}^{optimal} = \sqrt{2 \cdot \tau \cdot t_{down}} \tag{4.2}$$

That is, for longer down times, one must increase t_{DAQ} to optimize data acquisition. To do this, the ring cutoff current can be determined from the above and written as

$$I_{cutoff} = I_{max} e^{-t_{DAQ}^{optimal}/\tau} \tag{4.3}$$

The maximum injection current depends on the quality of the stored beam. The quality of the beam is mainly characterized by the beam halo, the presence of which is directly observable on the Beam Quality Monitor (BQM) photomultiplier tubes and drift chamber scaler rates. These provided the main diagnostic for the experimenters on whether to accept the delivered beam or to request that the accelerator operators perform additional tuning to improve beam quality. Prior to each injection, the BLAST detector high voltage system was ramped down to a set of standby voltages stored in the MYSQL database[1]. This provided protection against overloading the detectors during the injection flash. This is the high detector rate that occurs during the 1.3 μsec injection period which is caused by electrons scattering forward from the injection septum into the beam pipe walls in the region of the BLAST detector [43].

Once the ring had been filled, the current began to drop as the beam intensity was reduced by various loss mechanisms. Two primary sources of beam losses were scattering of the beam electrons by particles in the ring, mainly in the target region, and by synchrotron

[1]Those detectors bearing PMTs had running voltages ranging from -1600V to -2400V and standby voltages of -500V. The drift chamber running voltages were nominally -3800V and the standby values were -3000V.

radiation. It has been found that the former was the dominant effect in limiting the beam lifetime [43]. Collisions with atoms and molecules in the target or residual gas in the ring can cause the electrons in the beam to be scattered outside of the ring acceptance. Ring electrons can ionize the residual gas and trap these ions in their electrostatic, and to a lesser extent magnetic, fields [43]. This phenomena, called ion trapping, creates a density of ions in the beam that is the source of the beam halo and adds to the scattering losses. A strip chart from the EPICS slow controls system shown in Figure 4-1 displays typical current and lifetime behaviour.

From the above considerations, it is clear that to attain a reasonable lifetime for the

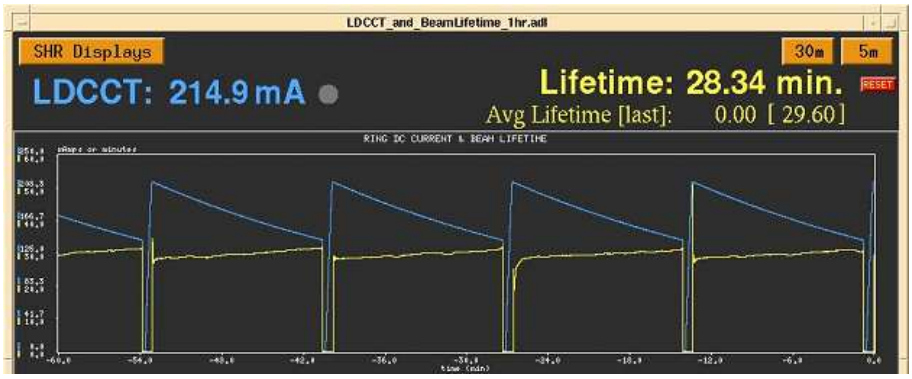

Figure 4-1: Beam Current and Lifetime

beam, the halo must be minimized. Achieving and maintaining a good ring vacuum was of paramount importance in this effort. Table 4.1 summarizes typical pressure in the target region for different operating modes. These pressures were measured by an ionization gauge referred to as Lattice Ion Gauge Internal Target (LIGIT) located in the region of the scattering chamber. Note the slight increase in LIGIT pressures during injection shown in the stripchart of Figure 4-2 from the EPICS system. To aid in reducing beam halo, a set of beam scrapers or "slits" were placed well upstream of the target. These were mechanically actuated devices that could be moved into the path of the halo as far

Target Mode	Beam Mode	LIGIT Pressure (Torr)
^2H ABS	stored	8.8E-08
^2H ABS	injection	1.2E-07
Empty	stored	8.8E-08
Empty	injection	1.2E-07

Table 4.1: LIGIT Pressure vs. Operating Mode

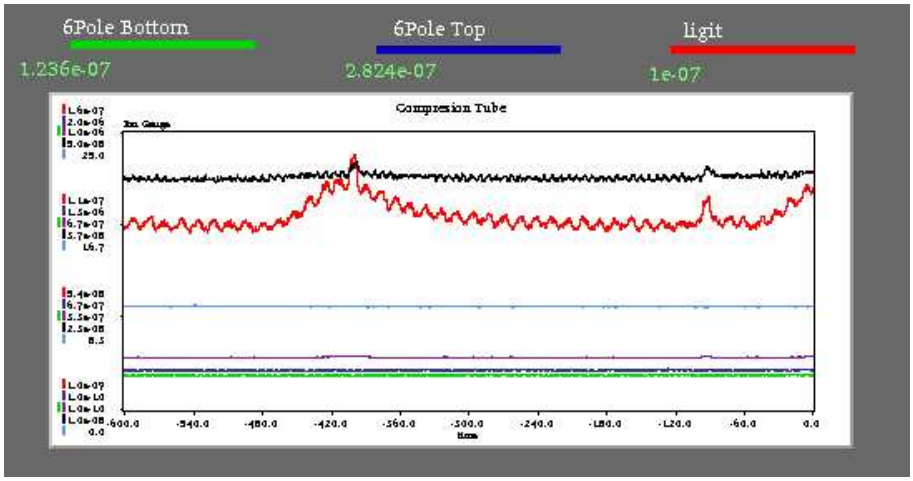

Figure 4-2: LIGIT Pressure vs Time

as possible to achieve maximum halo reduction while maintaining beam lifetime.

4.1.2 Beam Polarization

A real time measurement of the beam polarization near the target position was made possible with the Compton Polarimeter. These measurements were made independently of the operating mode of the beam with a polarization value extracted once per fill. An asymmetry of the backscattered photons from the Compton laser was measured once per fill, as this is how often the beam helicity was flipped, and beam polarization was found to be quite high at 0.6558 ± 0.0007 (stat), ± 0.04 (sys), well exceeding the initial requirements of the BLAST Technical Design Review (TDR). False asymmetries were also measured to illustrate the effect of background and were found to be less than 4% [62]. This was taken into account in the extraction of the polarization. Typical polarimeter data are shown in Figure 4-3.

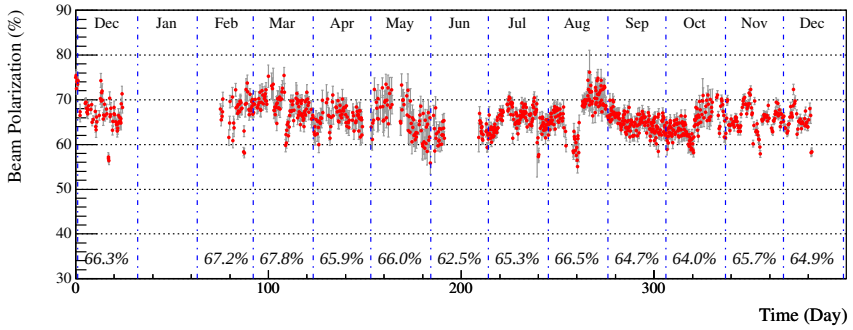

Figure 4-3: Typical Compton Polarimeter Beam Polarization Data

4.2 Performance of the Polarized Target

4.2.1 RF Dissociation and Atomic Fraction

Prior to installation into the atomic beam source assembly in the Bates South Hall, the dissociator was characterized with a Quadrupole Mass Analyzer (QMA). The figure of merit of the dissociator is primarily determined by the population of selected atomic species versus total population in the target. This degree of dissociation, called the atomic fraction α, is quantified as

$$\alpha \;=\; \frac{P^a}{P^a + 2\kappa_\nu P^m} \tag{4.4}$$

where P^a and P^m are the partial pressures of the atomic and molecular gases in the target respectively [3]. The factor $\kappa_\nu \simeq 1/\sqrt{2}$ is included to account for the difference between the atomic and molecular velocities of the target species.

Figures 4-4 and 4-5 illustrate the dependence of atomic fraction on RF power for various nozzle temperatures and flow rates in the dissociator. Note that as the flow rate increases, the atomic fraction decreases. Thus more RF power is required to obtain a comparable level of dissociation [3].

4.2.2 ABS Intensity

By replacing the target storage cell with an ionization gauge equipped compression tube, a measure of the ABS intensity was made. The intensity is defined as

$$I(Q) \;=\; I_0 \cdot Q \cdot e^{-Q/Q_0} \tag{4.5}$$

where Q is the flow into the dissociator, I_0 is the intensity in the absence of rest gas scattering, and Q_0 is a factor parameterizing the beam attenuation due to rest gas scattering. An average deuterium ABS intensity of $\simeq 2.6 \times 10^{16}$ [atoms/sec] was achieved during the course of the experiment. This intensity corresponds to a target thickness of $\simeq 4.5 \times 10^{13}$

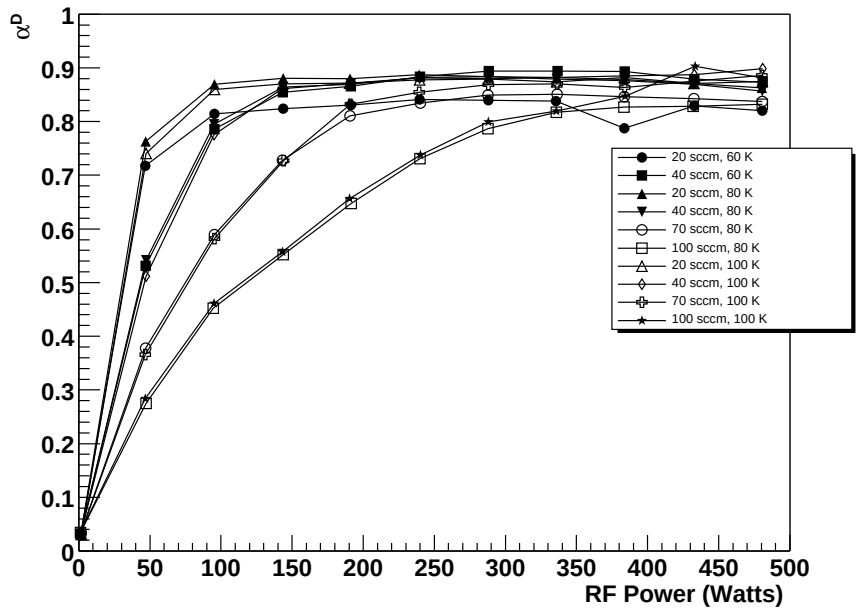

Figure 4-4: Deuterium Atomic Fraction versus Flow Rate and Nozzle Temperature

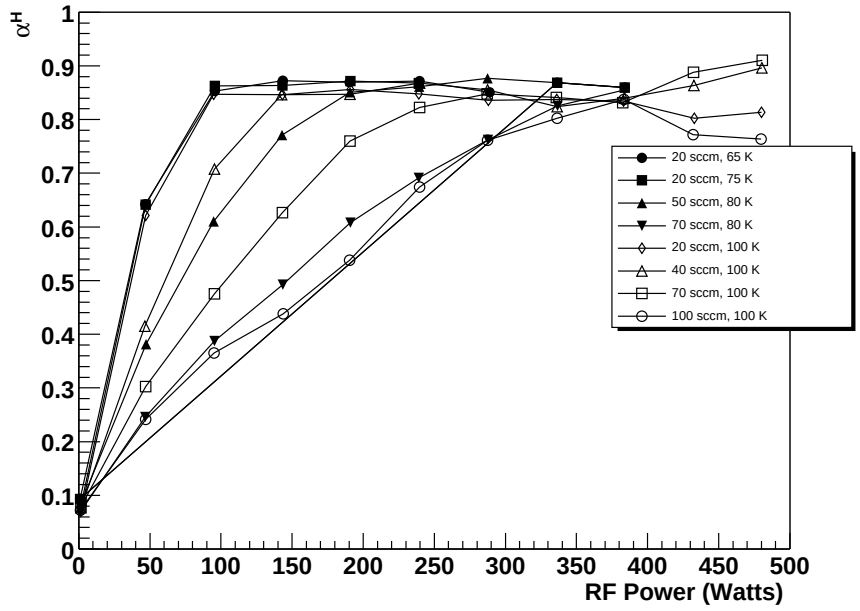

Figure 4-5: Hydrogen Atomic Fraction versus Flow Rate and Nozzle Temperature

[atoms/cm^2] [3].

4.2.3 Target Polarization

Magnetic Holding Field

The longitudinal and transverse components of the target holding field were measured prior to installation of the field coils in the Bates South Hall. These measurements are compared with simulations from the electromagnetic calculation package TOSCA[2] and are shown in Figure 4-6. In the plot of B_y versus I note the saturation of the longitudinal

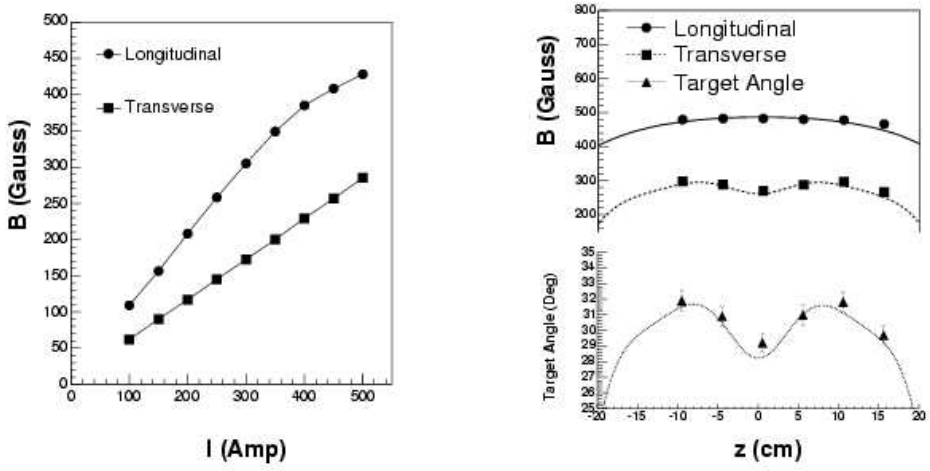

Figure 4-6: Target magnetic holding field components versus Current (left) and Vertex (right). Solid lines are from TOSCA simulations

field near 400 A, whereas the transverse field shows no saturation. Also note how the geometry of the magnet produces a dip in the transverse field in the central region of the target. The data show fair agreement with simulation.

[2]Vector Fields Inc., Aurora, IL USA

Target Polarization from d(e,e'p)n Analysis

The polarization of the BLAST internal target is critical to the measurement of the polarization observables. The target vector polarization was taken from the analysis of the deuteron quasielastic electrodisintegration channel d(e,e'p)n [63]. In this analysis the plane wave impulse approximation (PWIA) is assumed where the neutron is taken to be a spectator and the majority of the momentum of the virtual photon is transferred to the proton. This is strictly true only for a low value for missing momentum which is a defining characteristic of quasielastic scattering. In addition to cuts on low missing momentum, the data were cut on low momentum transfer, specifically $Q^2 < 0.2$ $[GeV/c]^2$. This was done in an effort to minimize statistical error and to make the measurement in a region of low model dependence, thus exploiting the PWIA assumption. The data in this region were compared with Monte Carlo simulations through a ratio which was subsequently fit with a 0^{th}-order polynomial. The parameter of the fit is then the factor hP_z which is the product of the beam and target polarization.

The Monte Carlo asymmetries were based on the formalism of Arenhövel et al [30] which assumes that the proton electric and magnetic form factors $G_E^p(Q^2)$ and $G_M^p(Q^2)$ have a dipole form. This has been shown to be inconsistent with the 2004 dataset, representing roughly half of the data, [54] and has been corrected for in this analysis by incorporating the empirical fits of Friedrich and Walcher [64]. The extraction of hP_z from the 2005 data, as used in this analysis, is still being refined at the time of this writing. The values of hP_z obtained from the pure dipole simulations were scaled by the ratio of the dipole form asymmetry to that of Friedrich and Walcher [63].

By taking the beam polarization, h, from the Compton polarimeter data, the target vector polarization, P_z, was extracted. Typical deuterium target vector polarization values which were measured daily for diagnostic purposes[3] are shown in Figure 4-7.

[3]The accepted values of P_z as derived from the product hP_z, which is what matters to the vector elastic analysis, were determined by using the *entire* dataset for each target angle setting and are thus not plotted

In addition to vector polarization, tensor polarization P_{zz}, of the target was measured

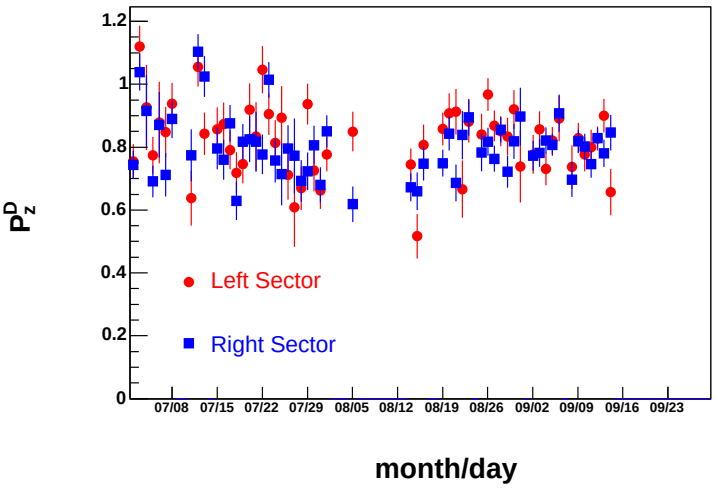

Figure 4-7: Target Vector Polarization vs Time

via the elastic electron-deuteron scattering channel as part of the T_{20} analysis [65]. A summary of vector and tensor polarizations are shown in Table 4.2. The uncertainties in the vector polarization measurments are due mainly to the systematic uncertainties in the Compton polarimeter measurement of the beam polarization. The uncertainty in the tensor polarization is due mainly to the systematic uncertainty in the model-dependent analysis of T_{20} in the elastic channel. The individual errors on h and P_z are irrelevant in the analysis of the vector polarization observables, however, as it is the *product* hP_z that is required here, and the errors on this product are much smaller than those on the beam or target polarization. Typical values for hP_z are 0.558±0.009 (stat), ±0.013 (sys.) for the July-September 2004 data and 0.441±0.003 (stat), ±0.013 (sys.) for the Spring 2005

on a daily basis.

Target	Reaction	P_z	P_{zz}
Hydrogen	p(e,e'p)	$78 \pm 4\%$	n/a
Deuterium	d(e,e'p)n, d(e,e'd)	$86 \pm 4\%$	$68 \pm 6\%$

Table 4.2: Target Polarization Summary

data[4].

4.3 Performance of the BLAST Detector

4.3.1 Mapping the BLAST Magnetic Field

The main BLAST magnetic field was mapped in the drift chamber and target regions using a set of Hall probes [66]. The field map data were then compared to Biot-Savart calculations. These calculations assumed that the main BLAST coils were in an ideal location. Figure 4-8 shows the comparison of the field map with the Biot-Savart calculations for the vertical component of the BLAST field, B_y, along the BLAST x-axis which runs perpendicular to the beam axis and parallel to the South Hall floor. Note that there

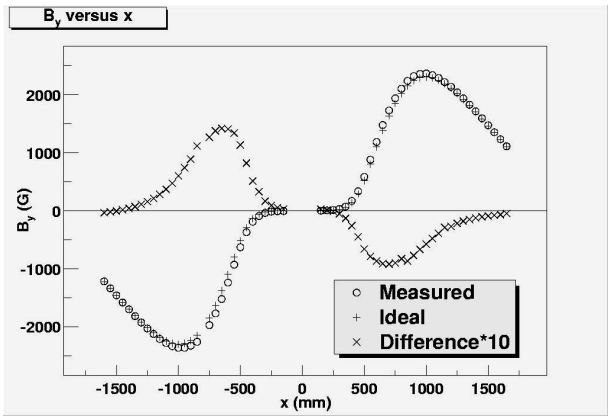

Figure 4-8: BLAST Field Map vs Biot-Savart Calculations for B_y, 500 mm downstream of the target in the midplane

[4]At the time of this writing the systematic error on the 2005 dataset value of hP_z had not been released

is relatively good agreement between the measured field and the calculated field. Minor differences are most likely due to the presence of extraneous magnetic materials and the *in situ* position of the coils which was known to within 1-2 mm [59]. Additionally the coils moved radially inward approximately 6-7 mm when full current (6730 A) was applied. This measured coil motion was not included in the Biot-Savart calculation shown in Figure 4-8 [59].

4.3.2 Time-of-Flight Scintillator Performance

The time-of-flight (TOF) scintillator system provided triggering and fast timing information to the BLAST data acquistion system. Its performance was thus critical to the operation of BLAST and the analysis of the data.

Time Resolution

Prior to installation in the BLAST detector subframes, the time resolution of each TOF was measured following the method of Giles [51]. This entailed placing the detector to be tested in between two reference detectors, which were themselves placed between two small paddles providing a coincidence trigger using cosmic rays. Furthermore, the test detector was placed orthogonal to the reference TOFs so that the positional dependence of the time resolution could be examined. This arrangment, minus the outer small paddles for clarity, is shown in Figure 4-9. In this figure, TOFs 1 and 2 are the reference detectors while TOF 3 is the detector of which the time resolution is being measured. The mean time, t_m, for each TOF is defined as the average time of the left and right photomultiplier channels.

$$t_m = \frac{t_L + t_R}{2} \tag{4.6}$$

If TOF 3 is placed exactly between the reference detectors with respect to the floor, then the difference, t_{diff}, between the average mean time of the reference detectors and the

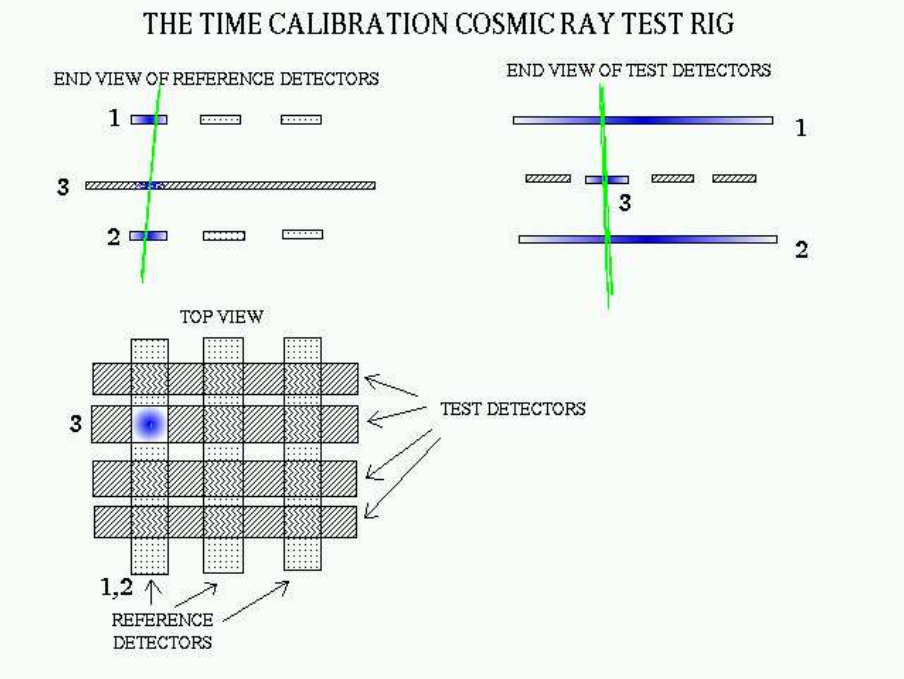

Figure 4-9: Detector Test Facility for TOF Time Resolution Measurement

detector being tested should be zero, *i.e.*

$$t_{diff} = \frac{t_{1m} + t_{2m}}{2} - t_{3m} \qquad \text{(should be zero)} \tag{4.7}$$

The time-of-flight between the two reference detectors is

$$t_{tof} = t_{1m} - t_{2m} \tag{4.8}$$

The error on t_{diff} is

$$\sigma^2_{diff} = \left(\frac{\partial t_{diff}}{\partial t_{1m}}\right)^2 \sigma^2_{1m} + \left(\frac{\partial t_{diff}}{\partial t_{2m}}\right)^2 \sigma^2_{2m} + \left(\frac{\partial t_{diff}}{\partial t_{3m}}\right)^2 \sigma^2_{3m} \tag{4.9}$$

$$\sigma^2_{diff} = \frac{1}{4}\sigma^2_{1m} + \frac{1}{4}\sigma^2_{2m} + \sigma^2_{3m} \tag{4.10}$$

The error on the time-of-flight t_{tof} is

$$\sigma_{tof}^2 \;=\; \sigma_{1m}^2 + \sigma_{2m}^2 \tag{4.11}$$

Combining these we can write the error on t_{3m} as

$$\sigma_{3m} \;=\; \sqrt{\sigma_{diff}^2 - \frac{1}{4}\sigma_{tof}^2} \tag{4.12}$$

The error σ_{3m} then defines the time resolution of that detector. Figure 4-10 displays the full width half maximum (FWHM) values for time resolution that were measured. The total number of measurements is 96 as the time resolution was measured at three locations for each of the 32 TOF detectors using three sets of reference detectors simultaneously. Note that the BLAST Technical Design Review specified a requirement of 500 psec FWHM

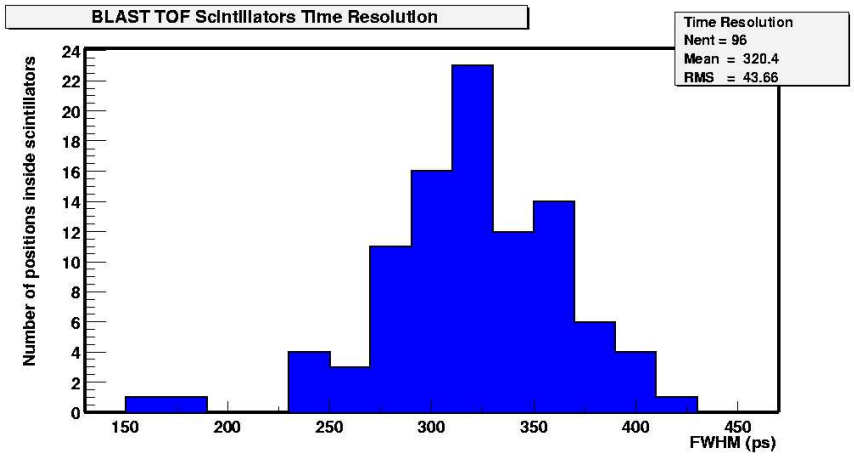

Figure 4-10: Detector Test Facility for TOF Time Resolution Measurement

for time resolution for coincident detectors. The BLAST TOF system, is within this requirement. Furthermore, a 200 MeV proton will reach a certain TOF detector ∼8 ns ahead of an elastically scattered deuteron. Thus the BLAST TOF time resolution easily

allows the TOFs to be used in discriminating between these two particles.

Due to variations in the BLAST data acquisition TDC electronics as well as cable lengths and other inconsistencies there exists an offset in timing for each TOF channel. These offsets were determined using low zenith angle cosmic rays which provided coincident events for TOF detectors in the left and right sector the BLAST. These low angle cosmic rays, mainly consisting of muons with $\beta \simeq 1$, provided a left-right sector coincidence rate of ~ 1.4 Hz. This allowed for timing calibration to be conducted periodically with only a few hours of data. The algorithm for determining the timing offsets was developed and thoroughly documented by Chris Crawford [54].

TOF Efficiency

Prior to installation in the BLAST detector subframe the efficiency of each time-of-flight scintillator was measured. Two small scintillating paddles were placed above and below the detector being tested forming a trigger using cosmic rays. Efficiency was defined by the number of events seen by the TOF divided by the number of triggers. Measurements were taken in the middle of each TOF and on the ends. A schematic of the efficiency setup is shown in Figure 4-11. All of the time-of-flight scintillators performed with an efficiency greater than 99%. The results are shown in Figure 4-12. Once the TOFs were in place in the BLAST subframes, spot checks the efficiency were made by placing a small trigger paddle on the outside of each TOF with respect to the beam and a second trigger paddle along the target scattering chamber. The efficiency was found to still be in agreement with the initial measurements. During the efficiency measurements, the optimal CFD threshold setting was determined to be 31.3 mV for all TOF channels.

Gain of Photomultiplier Tubes

The gains of the time-of-flight detector photomuliplier tubes (PMTs) were measured using cosmic rays and adjusted such that the peak of the ADC spectrum was at a target

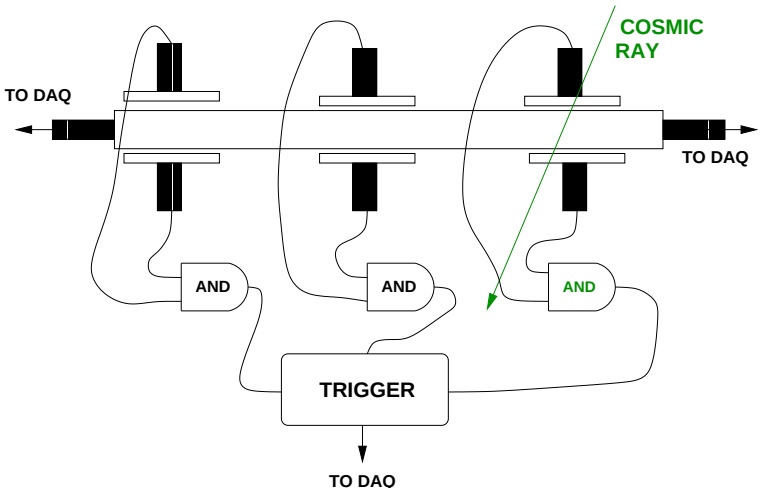

Figure 4-11: Detector Test Facility for TOF Efficiency Measurement

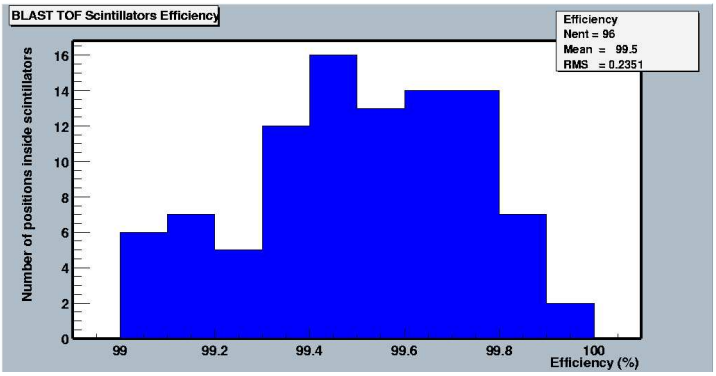

Figure 4-12: TOF Efficiency Measurements

ADC channel of 1250. Since cosmic rays are minimum ionizing, this corresponded to a lower limit of energy deposition in the TOFs by incident particles. When installed in BLAST, these minimum ionizing particles would be electrons which lose approximately 2 MeV/cm in organic plastic scintillator material. The selection of channel 1250 as a minimum ionizing target channel left adequate bandwidth in the ADC spectrum so that the maximum energy lost by protons and deuterons as they are fully stopped in the TOFs would fall below the maximum ADC channel of 8192. Eventually, TOF gains were measured with pedestal subtraction but that will be covered in the upcoming section on the data acquisition system.

During gain matching, the high voltage (HV) settings for the TOF PMTs were set and covered an operating range of -1600V to -2400V. Standby voltages were set to -500V for all channels. These values were stored in a MySQL database [67].

Once adjusted, the gains of the TOF photomultiplier tubes were monitored during running with beam. This was done by applying a Landau fit to the minimum ionizing peak in the TOF ADC spectra for each channel. Typical data representative of this are shown in Figure 4-13 for one quadrant of BLAST.

The most probable value (MPV) of the Landau fit was taken as a quantification of TOF gain. This value is plotted versus run number for a typical deuterium dataset and is shown in Figure 4-14

4.3.3 Drift Chamber Performance

As described in Chapter 3, the tracking algorithm of the BLAST drift chamber analysis is based on the fitting of three cluster of points with one cluster per chamber. The clusters are sense wire signals from ionization produced in the drift chamber gas by charged particles traversing the BLAST magnetic field. If the i^{th} cluster measurement of a track stub has an associated uncertainty $\epsilon_i = \sigma/\sqrt{N}$, where σ is the position resolution and N is the number of measurements, then, in the absence of multiple scattering, the momentum

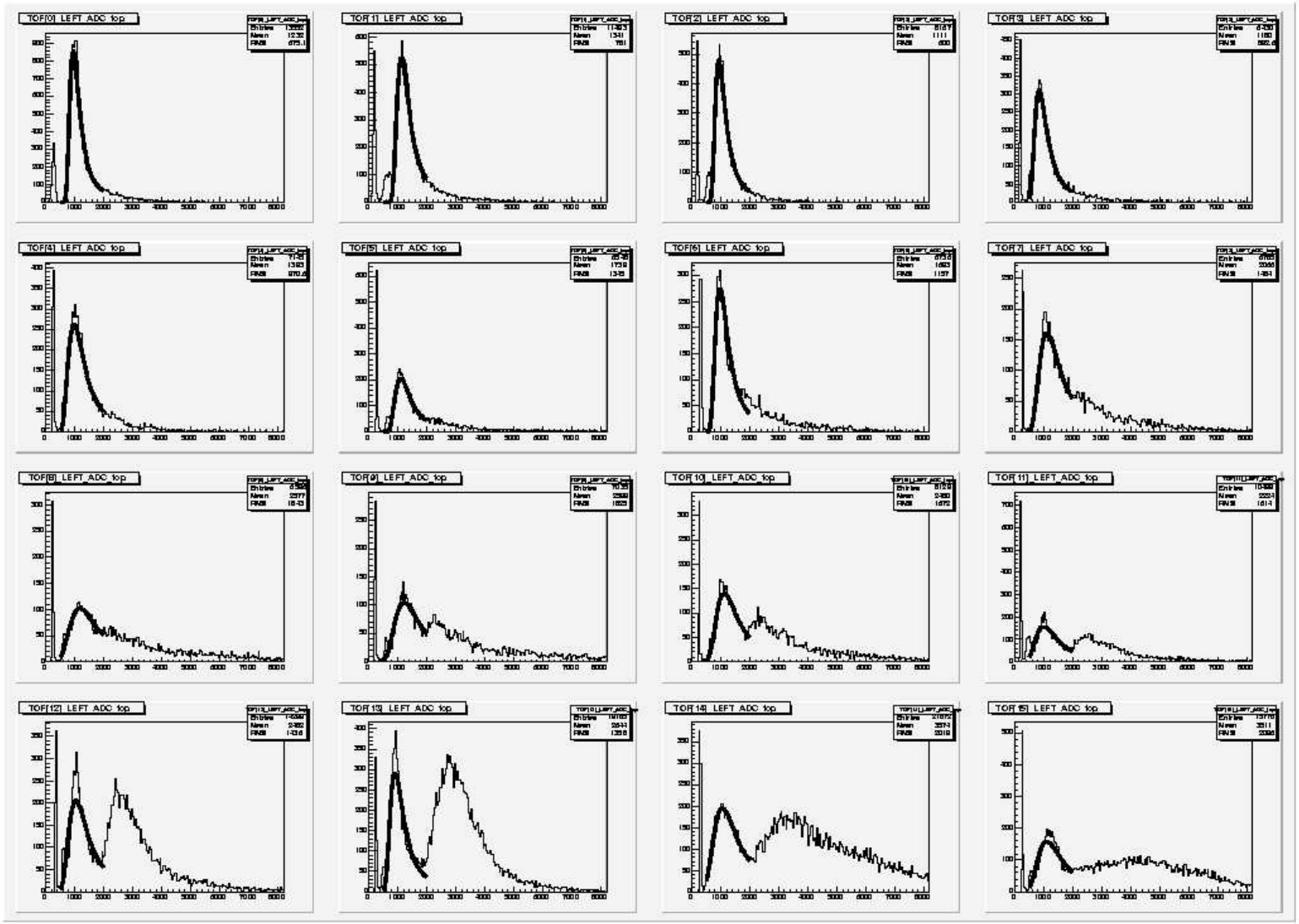

Figure 4-13: TOF Gains: Fitting the ADC Minimum Ionizing Peak for each Top Left Sector TOF PMT: The peak on the low end of the ADC spectrum is due to minimum ionizing electrons, the bump at higher ADC channel is due to protons and deuterons

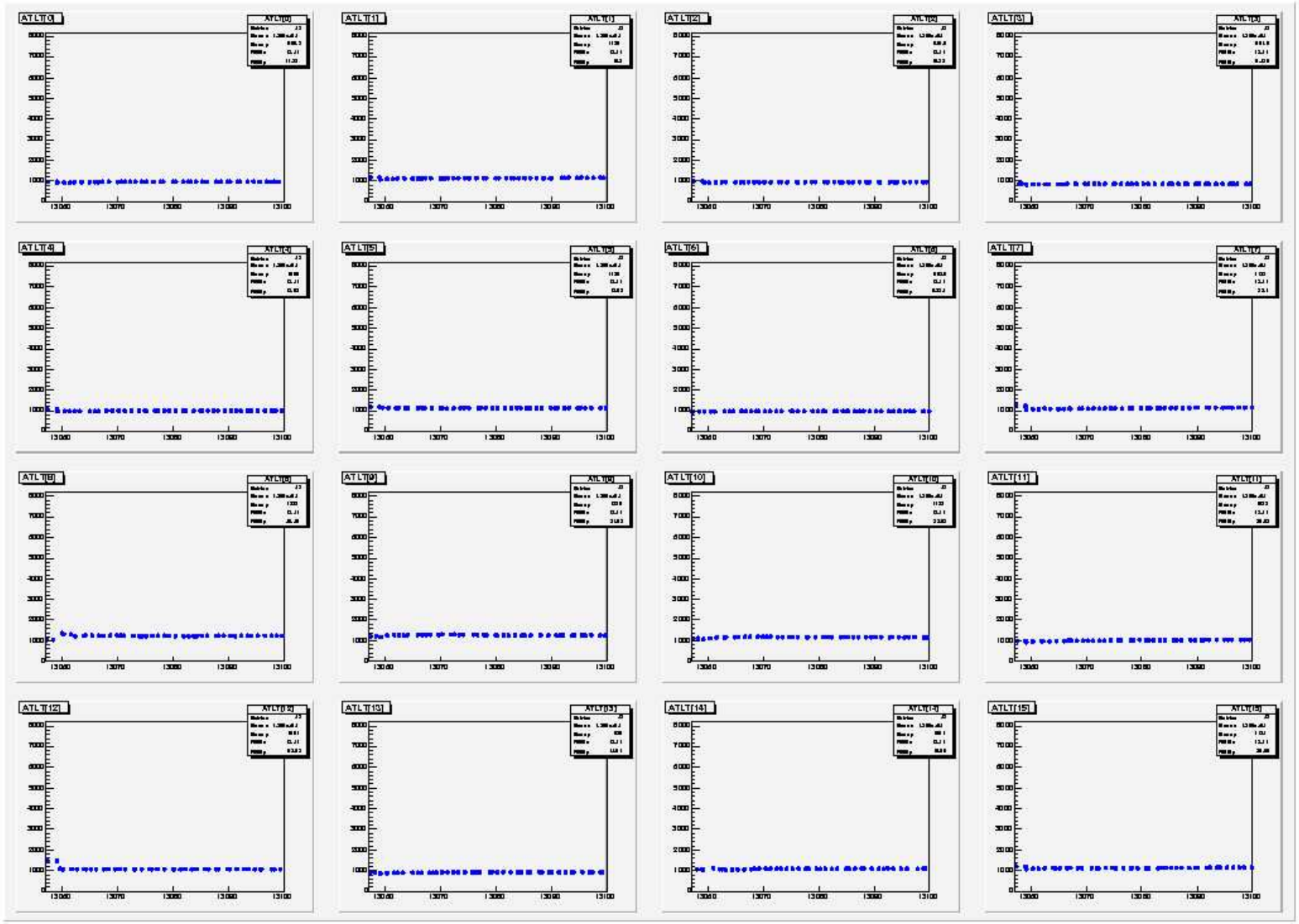

Figure 4-14: TOF Gain vs Run Number: The axis is the full scale ADC for Top Left Sector TOF PMTs. The horizontal axis is run number. The range is 50 runs.

Reconstruction Variable	Design Value	Measured Value
$\Delta k'$	2%	3%
$\Delta\theta_e$	0.30°	0.45°
$\Delta\phi_e$	0.50°	0.56°
Δz_e	1.0 cm	1.0 cm

Table 4.3: BLAST Drift Chamber Reconstruction Resolution

resolution is

$$\frac{\Delta p}{p} = \frac{8p}{0.3L_0}\frac{1}{\int Bd\ell}\sqrt{(\epsilon_1/2)^2+(\epsilon_2/2)^2+(\epsilon_1/2)^2} \tag{4.13}$$

where L_0 is the track length and $\int Bd\ell$ is the integral of the BLAST magnetic field along the path of the particle [3]

Elastic scattering from each hydrogen dataset was the reaction used to determine the drift chamber reconstruction resolution. The kinematic variables reconstructed in the drift chambers are the electron and proton polar angle, azimuthal angle, and momentum θ_e, k', ϕ_e, θ_p, p, ϕ_p. From Chapter 2 we recall that the momentum of an ultra-relativistic elastically scattered electron can be expressed as a function of electron scattering angle θ_e.

$$k' = \frac{\epsilon}{(1 + \frac{2\epsilon sin^2(\theta_e/2)}{M_p})} \tag{4.14}$$

The angle of the scattered proton can also be expressed as a function of θ_e

$$\theta_p = sin^{-1}\Big(\frac{1}{1+tan^2(\frac{\theta_e}{2})(\frac{\epsilon}{M_p}+1)}\Big)^{\frac{1}{2}} \tag{4.15}$$

Furthermore, the angle of azimuth ϕ_e and ϕ_p around the beam axis for the electron and proton respectively, are related by coplanarity since the final state of elastic scattering only has the two particles. Comparing the above calculated variables with those measured by the drift chambers yields a measurement of reconstruction resolution.

Assuming 130 μm intrinsic wire resolution and incorporating Monte Carlo studies of

multiple scattering, the present BLAST drift chamber reconstruction resolution values, including the vertex resolution Δz_e, are summarized in Table 4.3 [3].

The present measured values are close to those specified in the BLAST Technical Design Review.

4.3.4 Čerenkov Detector Efficiency

The Čerenkov counters lie between the drift chambers and the time-of-flight scintillators. Therefore a coincidence of drift chamber tracks and hits in scintillators on the other side of the Čerenkov counter provided a suitable trigger in measuring Čerenkov efficiency. An efficiency of approximately 85 % was measured with some degradation in efficiency toward the backward angle boxes. This was found to be due to edge effects where the downstream curved electron track completed the trigger with the most upstream TOF but missed the corresponding Čerenkov counter [63]. The efficiency of the Čerenkov counters is summarized in Figure 4-15 with respect to corresponding TOF detector.

4.3.5 Calibrating the BLAST Data Acquisition System

Trigger timing

The LeCroy 4564 OR module that provides the common strobe to the trigger supervisor was put in place to simplify the drift chamber reconstruction [61]. The adjustment of this Retiming-OR (RTO) required setting the 4518 programmable delay modules just downstream of the 3420 CFD modules such that synchronization of the RTO signals was achieved.

To conduct the trigger retiming a scintillator designated as the start counter (START) was placed just outside the scattering chamber such as it was in TOF efficiency testing (with TOFs installed in BLAST) described in section 4.3.2. Coincidence events were recorded between the START and each TOF for a particular sector of BLAST. The output

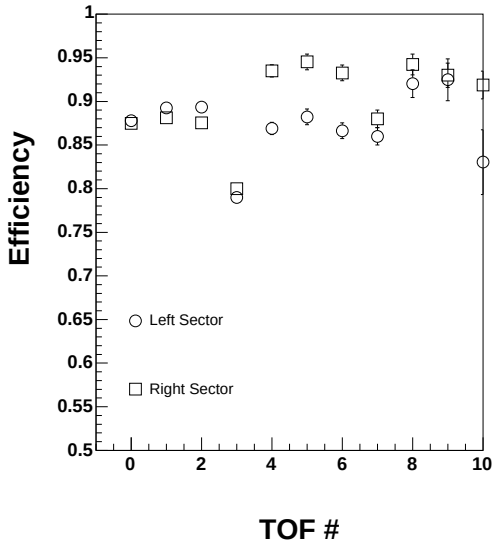

Figure 4-15: Čerenkov Detector Efficiency Measurements

of the RTO was moved from its running configuration, as an input to the TS (strobed mode), to a TDC channel so that its timing information could be recorded. The TS was thus run in non-strobed mode requiring a TRUE signal from the cross-sector memory look-up unit (XMLU) only. This modification is shown in the simplified trigger diagram in Figure 4-16

To make the analysis independent of absolute start time the measured TDC quantity was $(TDC_{RTO} - TDC_{START})$ where TDC_{START} is taken to be the mean of the TDC distribution from the upstream and downstream phototubes on the start counter. The delay of each channel was set so that the mean of the value $(TDC_{RTO} - TDC_{START})$ was, at most, the minimum adjustment (2 nsec) of the 4518 programmable delays for all channels.

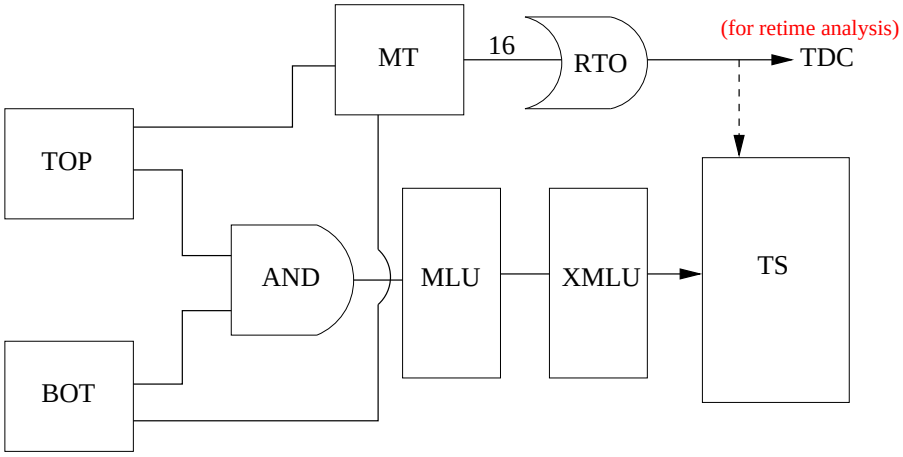

Figure 4-16: Simplified Trigger for Retiming Analysis

Trigger	Required TRUE	prescale	1st/2nd level rates [Hz]
1	TOF_l & TOF_r	1	$\sim$ 32/2
2	(TOF_l & !TOF_r & NC_r)||(TOF_r & !TOF_l & NC_l)	1	$\sim$ 1100/66
3	(TOF_l & TOF_l & CC_l)||(TOF_r & TOF_r & CC_r)	10	$\sim$ 87/5
4	(TOF_l & TOF_l)||(TOF_r & TOF_r)	100	$\sim$ 235/14
5	(TOF_l & BAT_r & CC_{bat})||(TOF_r & BAT_r & CC_{bat})	1	$\sim$ 16/1
6	TOF(12-15)$_l$ || TOF(12-15)$_r$	1000	$\sim$ 760/46
7	(TOF(0-11)$_l$ & CC_l)|| (TOF(0-11)$_r$ & CC_r)	3	$\sim$ 3200/92
8	Flasher	1	$\sim$ 3/(n/a)

Table 4.4: BLAST DAQ Trigger Types and Data Rates

Data Rates

The BLAST trigger supervisor has 8 defined trigger types to aid in the event selection for each reaction channel. With TOF representing time-of-flight detectors, CC for Čerenkov, NC for neutron, and Flasher representing the pulsed laser diagnostic system, these trigger types are outlined in Table 4.4 The overall deadtime was $\sim$ 15% [3] Certain trigger types have a prescale factor set to decrease their rate and thus maintain diversity of the recorded data with regard to trigger type. This is especially true of trigger type 6

representing singles events where only one sector of BLAST sees a true event.

ADC Pedestals

When the Fastbus ADC receives a gate it begins integrating current whether a particular PMT is generating a signal in response to a true event or not. Usually there is a DC offset that is internal to the ADC. During each 400 ns ADC gate, that spectrum is recorded and reflects the DC offset. This spectrum is called a pedestal and it occurs in all ADC channels. To obtain an absolute ADC measurement of a real event the pedestal was subtracted. To determine the pedestal a demand was made in the analysis that no true TDC signal occured for a given ADC signal. This discriminated against all true events. The pedestal values were determined in this manner for all runs and written to the BLAST MySQL database. Figure 4-17 displays raw and pedestal-subtracted ADC spectra for one quadrant of BLAST TOF detectors. The blue histograms contain both the pedestal which is the sharp peak at the low end of the ADC spectrum, and the real events at higher ADC values. The shaded histograms are the same real data but with the pedestal subtracted. The most probable value (MPV) is taken from the Landau fit of the latter as the pedestal subtracted gain of the phototubes.

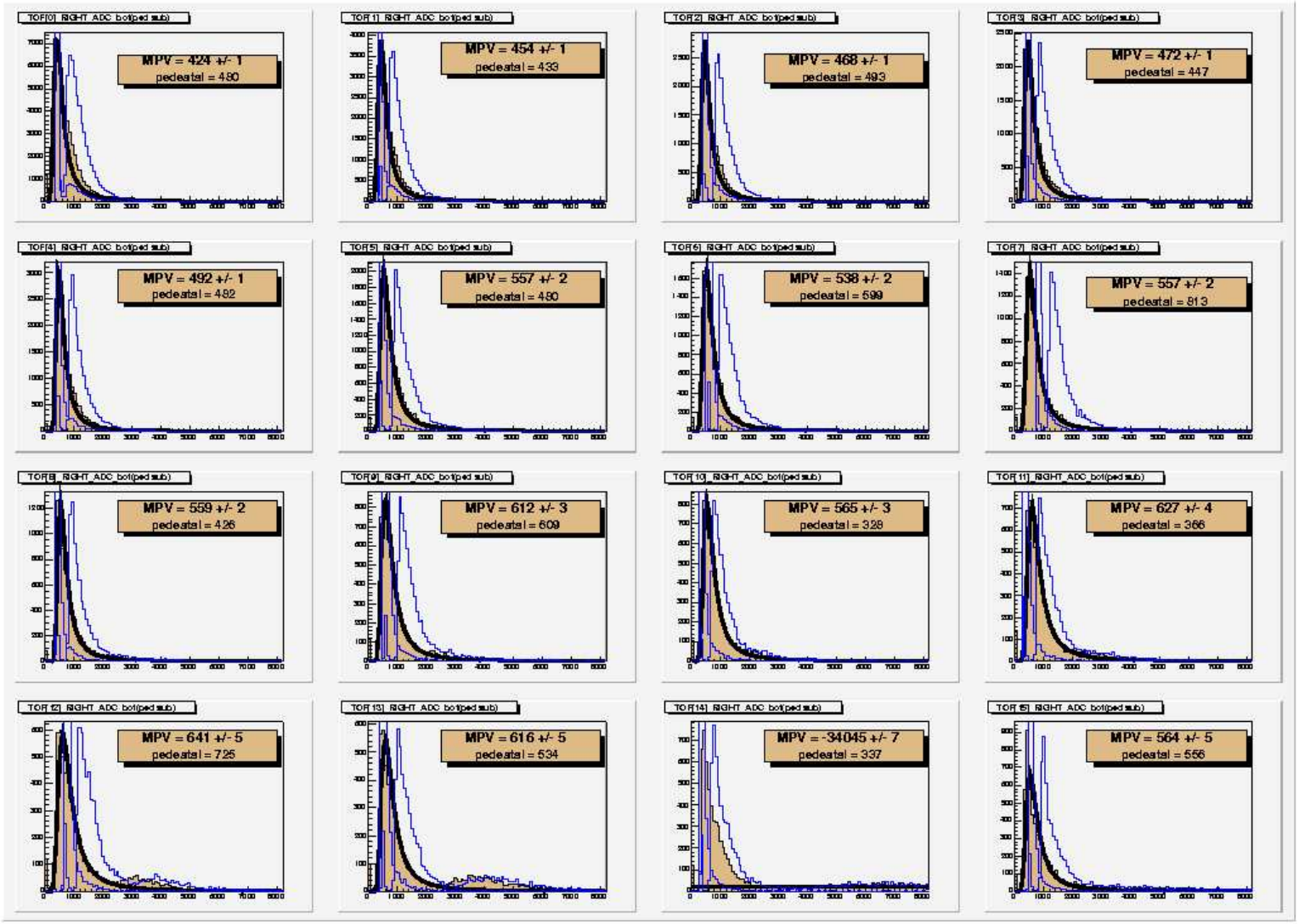

Figure 4-17: TOF Pedestal-Subtracted Gains

CHAPTER 5

Data Analysis

During this experiment approximately ∼1000 kC of charge were collected while data was taken simultaneously for various reaction channels. The polarized deuterium data were taken intermittently with other data for beam, target, and detector studies, as well as polarized hydrogen data, over the periods of May, July-September 2005, and February-May 2005. In addition to the beam-target vector asymmetry, this analysis makes use of the tensor polarization observables of the T_{20} experiment [22] as well as the measurement of the product of beam and target polarization, hP_z, from the deuteron electrodisntegration channel [63].

5.1 Drift Chamber Track Reconstruction

Although a rough estimate of polar angle θ with respect to the beam can be made using the TOF detectors, it is the drift chambers that provide a measurement of this as well as other kinematic variables such as the azimuthal angle about the beam ϕ and momentum p.

A particle of charge q and mass m moving in a magnetic field $\mathbf{B}$ with a velocity $\mathbf{v}$ will experience a force $q\mathbf{v} \times \mathbf{B}$. Relating this force to Newtonian laws of motion for an object subjected to centripetal acceleration yields an expression for the radius of the particle's trajectory.

$$r = \frac{p}{qB} \tag{5.1}$$

where p is the momentum of the particle. This idea is the basis for the reconstruction of particle momenta using the BLAST drift chamber data. Knowledge of the BLAST magnetic field along a charged particle's trajectory and the solution to a fit of that trajectory allows the determination of the particle's momentum.

As it travels through the BLAST drift chambers a particle has a position $\mathbf{x} \rightarrow (z, d)$ and momentum $\mathbf{p} \rightarrow (p, \theta, \phi)$ that together entail 5 degrees of freedom. With regard to physics analysis referenced to the interaction vertex, these are labeled, as above, (p, θ, ϕ, z, d) where d is the distance of closest approach to the beamline. With regard to reconstruction analysis, the trajectory at the drift chamber entrance plane is described by $(p_w, \theta_w, \phi_w, x_w, y_w)$. In this latter system x_w is along the face of the drift chamber in the horizontal plane and increases in the upstream direction, y_w is in the same orientation as the y-coordinate in the BLAST frame, and z_w is perpendicular to the drift chamber entrance planes and directed away from the beamline [54]. The distance of closest approach is fixed at $d = 0$ since the beam position is known much better than the drift chamber positions. This reduces the number of degrees of freedom to four.

Twelve hits are required on drift chamber sense wires to reconstruct a track. As described in chapter 3, three stubs form a track in the drift chambers. A first pass fit of these stubs is made with the assumption that the track is circular. Many stubs are associated with each track and this initial fast fitting accounts for all combinations of stubs with an iterative elimination of bad track candidates.

Once tracks are initially linked, fitting is done numerically by finding the roots of $\mathbf{p} = \mathbf{f}^{-1}(x_0)$ where $\mathbf{p} = (p, \theta, \phi, z)$ and $\mathbf{x}_0$ contains the coordinates of the track hits. The roots $\mathbf{x} = \mathbf{f}(\mathbf{p})$ are solved for using a modified version of the Newton-Rhapson method [54]. This method is summarized in Figures 5-1(a), 5-1(b), 5-1(c), 5-1(d).

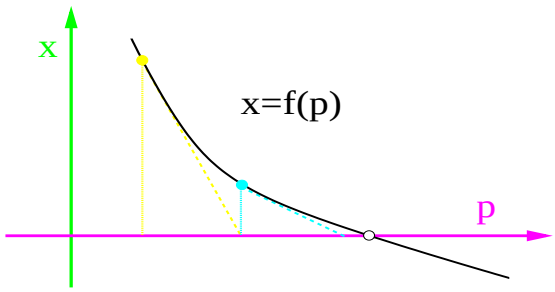

(a) In one dimension, the derivative of f maps the deviation dx from the initial guess to the adjustment dp, and so forth.

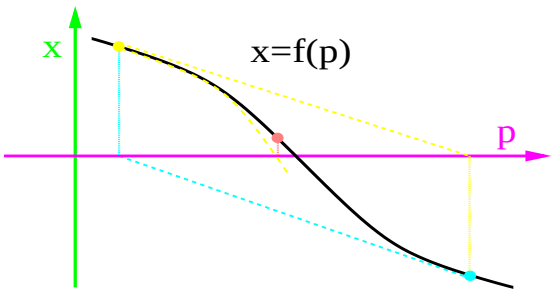

(b) In some cases the Newton method may fail to converge, and it is necessary to backtrack to a smaller correction dp.

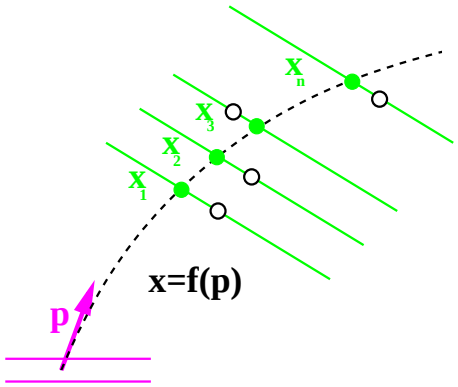

(c) For track fitting, the function f maps the 4-dimensional track trajectory $\mathbf{p}$ to the 18-dimensional vector of wire hits $\mathbf{x}$.

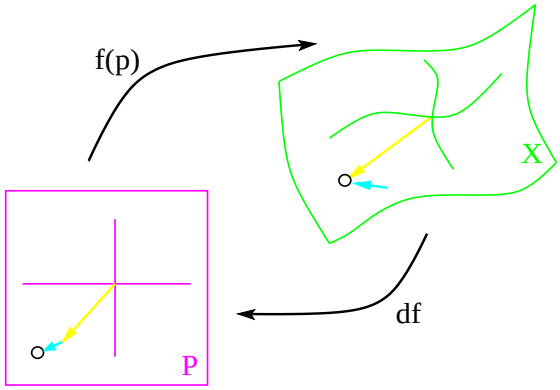

(d) In each interation the trajectory $\mathbf{p}$ is corrected by $\mathbf{dp} = \mathbf{J}^{-1}\mathbf{dx}$, where J is the Jacobian derivative and $\mathbf{dx}$ is the deviation of the simulated track from the wire hits.

Figure 5-1: An application of the Newton-Rhapson method to track fitting.

5.2 BLAST Monte Carlo

Monte Carlo simulations of elastic electron-deuteron events in the BLAST detector were created with the code *blastmc* which was based on GEANT 3.21 written in Fortran. An event generator, *DGen*, which was based in C++, simulated various electron scattering processes including the elastic channel. These simulations accounted for energy loss and multiple scattering of the scattered particles. The Abbott parameterization I [7] of the world data on the deuteron elastic form factors $G_C(Q^2)$, $G_Q(Q^2)$, and $G_M(Q^2)$, was used as the input to the elastic cross section.

The simulated events were written to a CODA format file and the Monte Carlo data were analyzed in the same manner as the real electron-deuteron data with only minor differences. For example, beam and target polarizations were assumed to be 100% but the data were scaled by the beam-target polarization product hP_z. The vertex was generated with a triangular distribution function to follow the measured target density distribution [3]. In our analysis four million Monte Carlo events were generated, a considerable fraction of which did not survive the initial screening.

The Monte Carlo (MC) provided a check on the quality of the data analysis. Specifically, we made use of the Monte Carlo in the analysis of systematic errors and of the vector polarization observables themselves. In the latter case, however, the fact that the BLAST MC is based on the Abbott parameterization indicates that, for an infinite amount of events, the Monte Carlo will always converge to Abbott. As will be seen in Chapter 6, the results of this experiment are compared to the prediction of Abbott as well as others.

5.2.1 Radiative Corrections

Due to the finite energy resolution of particle detectors, any soft ($E_\gamma < \delta E_{detector}$) photons emitted by the incident or the scattered electron will not be detected. Furthermore, the virtual photons of vertex corrections can not be observed by even a detector

with perfect resolution. Thus, true elastic scattering is not what is observed and the measured cross section is the elastic cross section scaled by some factor representing these radiative corrections. As opposed to their contribution to the elastic scattering cross section, however, radiative effects are expected to cancel to first order [68], when measuring polarization asymmetries by taking ratios of the cross sections.[1]

5.3 Selection of Elastic Events

Prior to applying specific elastic cuts, general event selection criteria were imposed across the board to discard any events that were considered either unphysical or not emanating from the target region. Data passing these cuts were then subjected to more stringent kinematic, and then timing, cuts for selection of elastic electron-deuteron events.

5.3.1 First Order Cuts

Interaction Vertex

The vertex z of the interaction for each event is obtained from drift chamber reconstruction. Two basic cuts are made in this regard. First, a cut is made to ensure that the observed tracks originate in the target region. Second, a cut is made to require that multiple tracks have a common vertex and thus result from the same interaction.

Electromagnetic showers which are a product of the beam halo striking a collimator upstream of the target were a primary source of background in this experiment. These showers were eliminated by the above vertex cuts.

Although the target cell lengths used were 40 and 60 cm in length, over the course of the experiment the interaction region was assumed to lie within $z = -15$ and $+18$ cm. This was done as the target holding field was limited beyond this range thus causing

[1] At the time of this writing a study of radiative corrections is being conducted. This is based on a mapping of the elastic electron-proton scattering code MASCARAD for the elastic electron-deuteron channel [68].

marked deviations in the target spin angle.

The common vertex cut was applied by taking the absolute value of the difference of the vertex for a track in the left sector with that of a track in the right sector. Since the measured vertex depends on electron angle, and the resolution of this angle varies over the kinematic range, the common vertex cut will be a function $f(\theta_e)$ of this resolution [65]. Applying this idea we have for the common vertex cuts

$$|z_L - z_R|_{\theta_e=20^\circ} < 4.9 \text{ cm} \tag{5.2}$$

$$|z_L - z_R|_{\theta_e=80^\circ} < 2.5 \text{ cm} \tag{5.3}$$

The common vertex distribution prior to the application of these cuts is shown in Figure 5-2.

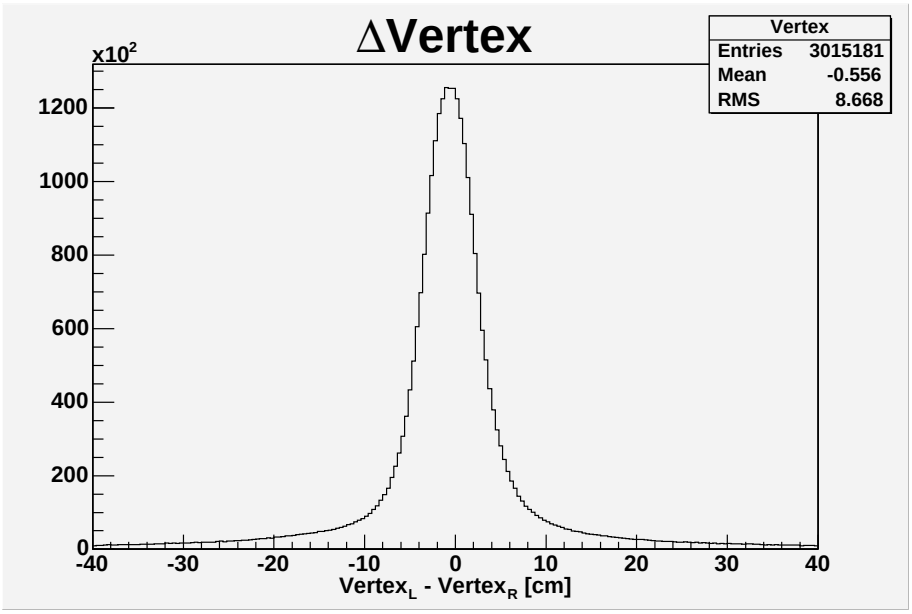

Figure 5-2: Left-Right Vertex Difference

BLAST Acceptance Cuts

In addition to vertex cuts, global cuts were placed on the data to eliminate those events that were recorded but physically should be well out of the BLAST acceptance. This meant limiting the polar angle of the observed particles to be within the range $20^\circ < \theta < 80^\circ$. The azimuthal angle was limited to the range $-20^\circ < \phi < +20^\circ$. The BLAST angular acceptance is shown in Figure 5-3 where the angle of azimuth is plotted against the polar angle. Note that some events are well outside the BLAST acceptance especially at polar angles of $\theta > 80^\circ$. These events were eliminated from the analysis.

Also the momentum acceptance of BLAST was limited by these first order crude cuts

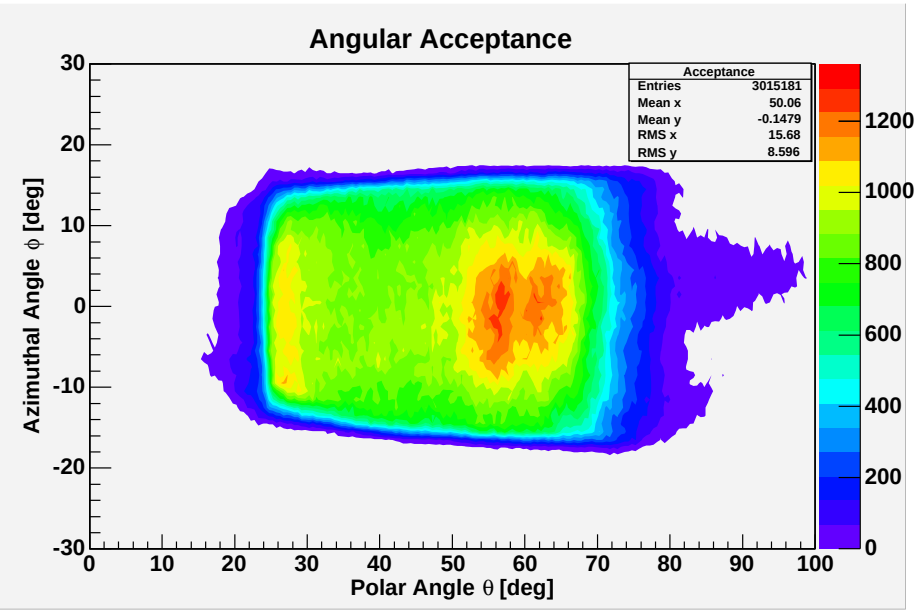

Figure 5-3: Reconstructed Angular Acceptance Distribution

to be between 0.12 and 0.95 GeV/c with the former limit being well below the deuteron detection threshold ($\sim 30 MeV/c$), and the latter limit exceeding the beam energy, to account for drift chamber uncertainties.

Charge Determination

Once vertex and acceptance cuts had been applied, the charge of each particle in a given event was determined. This was done using the knowledge of the BLAST magnetic field and the sense of curvature of the trajectory for each particle. The BLAST field was operated mainly in what was called *inbending* mode where negatively charged particles were bent toward the z-axis. This caused many unwanted reaction products such as electrons from Møller scattering to be directed down the beampipe and thus outside of the BLAST acceptance.

5.3.2 Elastic Kinematic Cuts

Once the data had been screened for unphysical or non-target related events, tighter kinematic constraints were placed to further isolate the elastically scattered electron-deuteron pairs.

Coarse Kinematic Cuts

Prior to being subjected to stringent governing equations of elastic scattering, coarse cuts were applied to eliminate any unlikely elastic events. Initially these included coplanarity and graphical selection of events with regard to momenta which removed a portion of the data from plots of momenta in the opposing sectors of BLAST that did not correspond to elastic scattering. The rough graphical cuts required that [65]

$$|\mathbf{k}_e| \; > \; \frac{3}{4} - \frac{1}{3}|\mathbf{P}_X| \tag{5.4}$$

where $\mathbf{k}_e$ is the momentum of the scattered electron and $\mathbf{P}_X$ is the momentum of the positively charged particle scattered into the opposite sector.

Being that elastic electron-deuteron scattering produces a two-body final state, the

outgoing trajectories will lie in a plane with the beam axis due to the conservation of momentum. We can thus form a coplanarity cut limited by the resolution of the angles of azimuth, ϕ_L and ϕ_R, for particles scattered into the left and right sectors of BLAST respectively, as an additional coarse selection criterion for elastic events. The coplanarity cut required that

$$|\phi_L - \phi_R| \ < \ 3^\circ \tag{5.5}$$

Electrons elastically scattered to the most backward angle of the BLAST acceptance

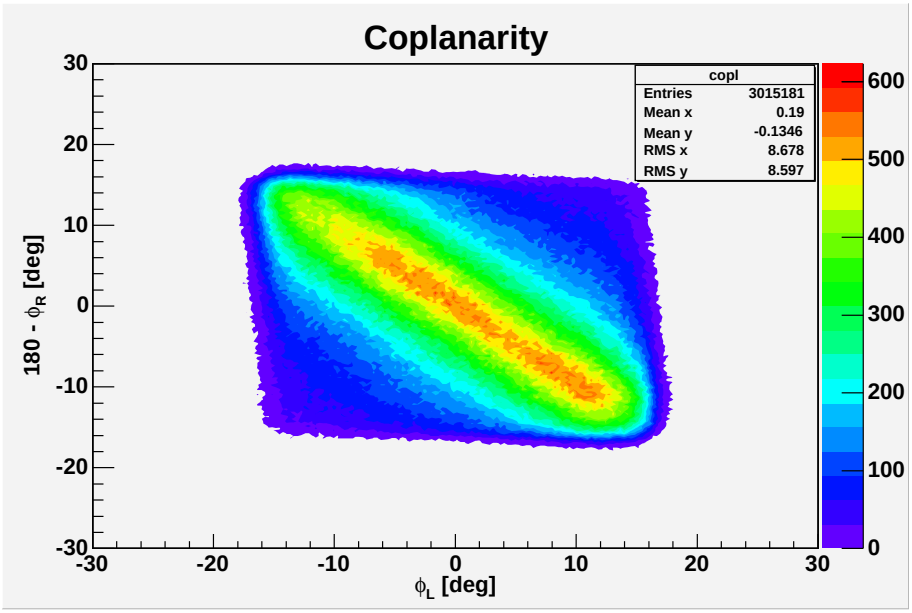

Figure 5-4: Coplanarity of Track Trajectories

will have a momentum of $\simeq 0.62$ GeV/c. Since electrons have a rest mass of 0.511 MeV, these high Q^2 electrons can still be considered ultra-relativistic and thus have a value of $\beta \simeq 1$. That is, for all intents and purposes, they are moving are the speed of light in the frame of the Bates South Hall. Elastically scattered deuterons corresponding to these

electrons will have momenta equal to the momentum transfer $\mathbf{q}$ in the lab frame where

$$|\mathbf{q}|^2 \;=\; \omega^2 - q^2 \;=\; \omega^2 + Q^2 \;\simeq\; 0.92(GeV/c)^2 \tag{5.6}$$

so that the momentum of the deuteron is $P_d = \sqrt{|\mathbf{q}|^2} = 0.96$ GeV/c. With the deuteron mass of $M_d = 1.876$ (GeV/c), this yields

$$M_d \;=\; \frac{P_d}{\beta\gamma} \;=\; \frac{P_d}{\beta}\sqrt{1-\beta^2} \qquad \rightarrow \beta \;=\; \sqrt{\frac{1}{(M_d/P_d)^2+1}} \;\simeq\; 0.46 \tag{5.7}$$

Therefore, cutting on β is a clear way of requiring that tracks in the left and right sectors of BLAST correspond to electron deuteron pairs even at the highest momentum transfers. The β cut was defined as such that, if the positive particle was above its maximum possible β, the event was discarded. No coarse β cuts were made on the electron as this was addressed with a coarse electron momentum cut of $|\mathbf{k}_e| < 0.95$ [GeV/c].

Those events passing the second level trigger 1, which required a drift chamber track in both left and right sectors, numbered 1,703,942 for the total 2004-2005 dataset. Of these, 1,249,380 remained after the application of the coarse kinematic cuts.

Fine Kinematic Cuts

After passing the coarse cuts described in the previous paragraphs, the data were subjected to tighter kinematic constraints adopted directly from the T_{20} elastic analysis [65]. This again entailed using momenta and track angle as selection criteria but this time in a more direct comparison to the resolution of the spectrometer.

The scattered electron polar angle θ_e was used to calculate the momenta of the scattered electon and deuteron as well as the deuteron polar angle θ_d under the assumption that elastic scattering had taken place. The difference of these kinematic variables with

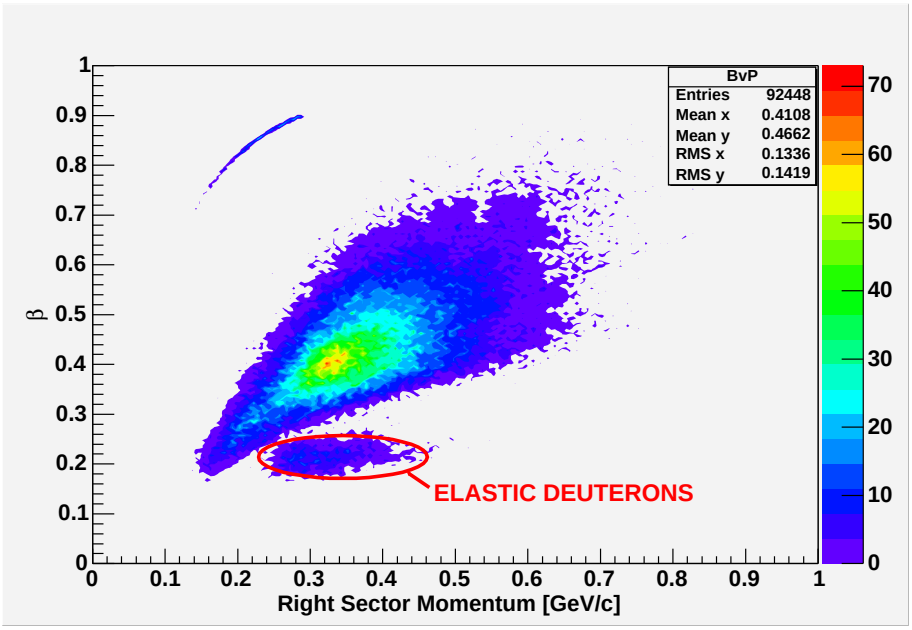

Figure 5-5: β vs. Momentum for a positively charged particle in the right sector of BLAST. Vertex cuts and coplanarity cuts have been applied at this stage. The elastic electron-deuteron events are circled at low β. Highly relativistic pions appear in the upper left with values of $\beta \rightarrow 1$

repsect to their measured counterparts was taken and compared with set values [65].

$$-0.12\ GeV/c\ <\ |\mathbf{k}(\theta_e)| - |\mathbf{k}^{elastic}|\ <\ 0.12\ GeV/c \tag{5.8}$$

$$-0.25\ GeV/c\ <\ |\mathbf{P}_d(\theta_e)| - |\mathbf{P}_d^{elastic}|\ <\ 0.25\ GeV/c \tag{5.9}$$

where $|\mathbf{k}|$ and $|\mathbf{P}_d|$ are the measured momenta of the scattered electron and deuteron respectively and $|\mathbf{k}^{elastic}|$ is calculated from 2.40 while $|\mathbf{P}_d^{elastic}|$ is found from the law of cosines to be

$$|\mathbf{P}_d^{elastic}|\ =\ \sqrt{\epsilon^2 + \epsilon'^2 - 2\epsilon\epsilon\cos\theta_e} \tag{5.10}$$

This was the final screening of the data based on drift chamber reconstruction. These kinematic cuts were as follows: The number of events from the total dataset remaining after the application of the fine kinematic cuts was 594,328.

5.3.3 Elastic Timing Cuts

A dominant source of background in this experiment were protons from the electrodisintegration of the deuteron. A significant portion of these protons survive the aforementioned kinematic screening. Therefore additional constraints must be applied to ensure that elastically electron-deuteron events have been selected.

To demostrate the validity of this, consider a deuteron moving with a momentum of 300 MeV/c in the lab frame. This momentum corresponds to an energy of

$$E \;=\; \gamma mc^2 \;=\; \sqrt{\mathbf{p}^2 + M_d} \;\simeq\; 0.985\; GeV \tag{5.11}$$

where the corresponding value of $\gamma = 0.218$. Over a distance of 3 m in the lab frame this deuteron has a time of flight of $\sim$63 $nsec$. A proton at this momentum would have a time of flight of $\sim$46 $nsec$. Clearly, if a proton and a deuteron have the same momentum as measured by the drift chambers, they can be separated in timing.

Based on the above idea, the final cut in the selection of elastic electron-deuteron pairs was on the TDC values of the BLAST TOF scintillators [65]. Since all timing is relative in BLAST as measured with respect to the RTO common strobe, cuts were made on the time of flight *differences* between hits in the left and right sectors. Taking the difference of the time of flight removed any dependence on the relative start time of the trigger. The warranting of such cuts is seen in Figure 5-6 which shows a grouping of deuterons for TOF differences across the left and right sectors of BLAST >500 channels. Timing cuts are now applied where, in addition to the described elastic cuts, a cut on TOF detector number has been made since the timing cuts are detector dependent. An example of this is shown in Figure 5-7 where the detector cut requires events only appearing in RTOF15 and LTOF0 with timing cuts applied which were particular to these TOFs. Specific timing cuts were made for all possible detector combinations. In these two figures, a cut has been made to select events with positively charged particles in the right sector and electrons in

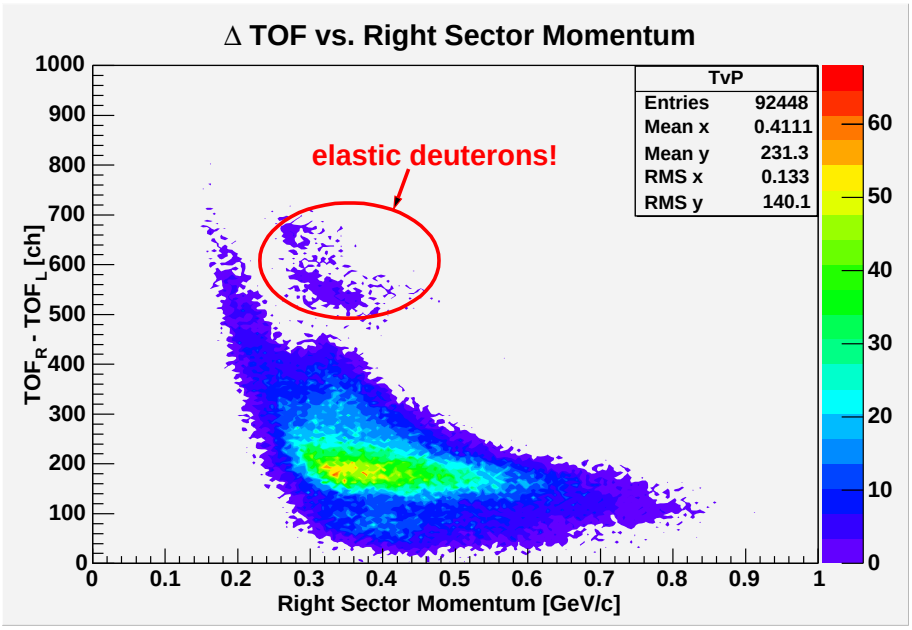

Figure 5-6: TOF Difference vs. Right Sector Momentum: All TOF Detectors

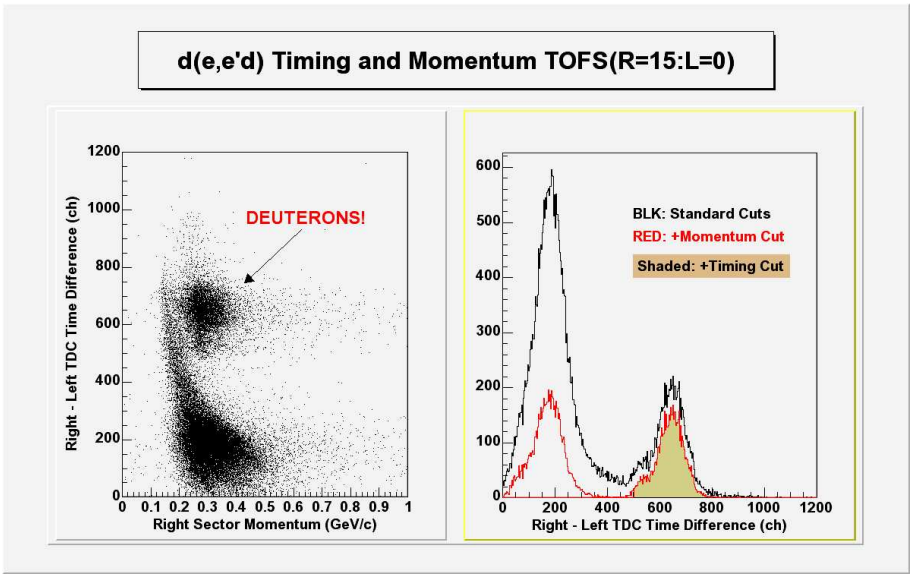

Figure 5-7: TOF Difference vs. Right Sector Momentum: Cut on RTOF15 and LTOF0

the left sector. After the application of the base level and kinematic cuts two peaks are clearly distinguishable in the timing spectrum. With electrons moving near the speed of light for both *ed* and *ep* events, the time difference between these two events is evident with the longer time of flight TDC values belonging to the deuterons.

After application of the timing cuts 494,402 events out of the total dataset remained.

5.4 Quality of the Data

Those events that survive all of the aforementioned cuts are used in a check of the data quality. In Figure 5-8 we see the difference bewteen the energy ω delivered by the incident electon beam minus that energy assuming that elastic scattering has taken place. The unfilled histogram represents those data that pass the basic general cuts for good physical events in BLAST. The shaded histogram are those events passing the elastic scattering cuts described in the previous section. The gaussian distribution roughly centered on $\omega = 0$ of the latter gives confidence that a good selection of elastic events has been made. This is further reinforced by the good agreement of the predicted measured polar angles θ_L and θ_R for particles entering the left and right sector of BLAST respectively. Measured values of θ_R versus θ_L are shown in Figure 5-9. A comparison of the measured angles θ_L and θ_R with the calculated angle θ_q based on the measured angle θ_e from the opposite sector is shown in Figure 5-10.

The lack of perfect symmetry in Figure 5-8 is most likely due to two causes. The first is the not accounting for energy loss as the particles traverse the BLAST detector components. This results in a lower observed energy than that calculted for elastic scattering. However, since the electrons in this case are minimum ionizing, this will be a small effect. The second issue is that of kinematic corrections. At the time of this writing, there still exist certain corrections to the electron momenta that are required to obtain symmetry

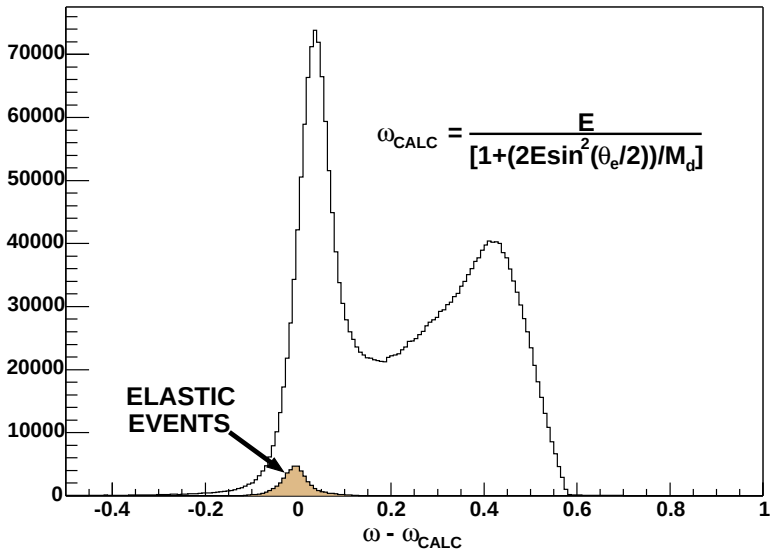

Figure 5-8: Quality of the elastic data as illustrated by comparison of measured and calculated value of ω which is measured from $\omega = \epsilon - \epsilon'$ where $\epsilon = 0.850\ GeV/c$ and ϵ' is the magnitude of the measured momentum of the scattered electron. ω_{CALC} takes ϵ' from Equation 2.40 assuming that elastic scattering has taken place. The unfilled histogram are those events passing general data quality cuts, while the shaded histogram are those events passing the elastic cuts.

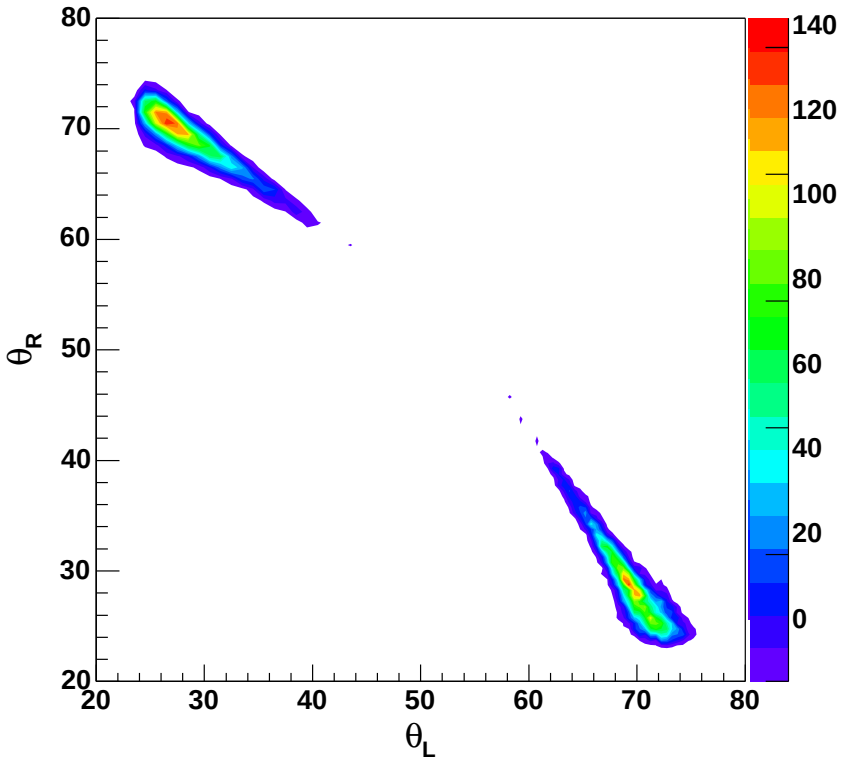

Figure 5-9: The measured polar angles θ_R vs. θ_L following implementation of elastic cuts.

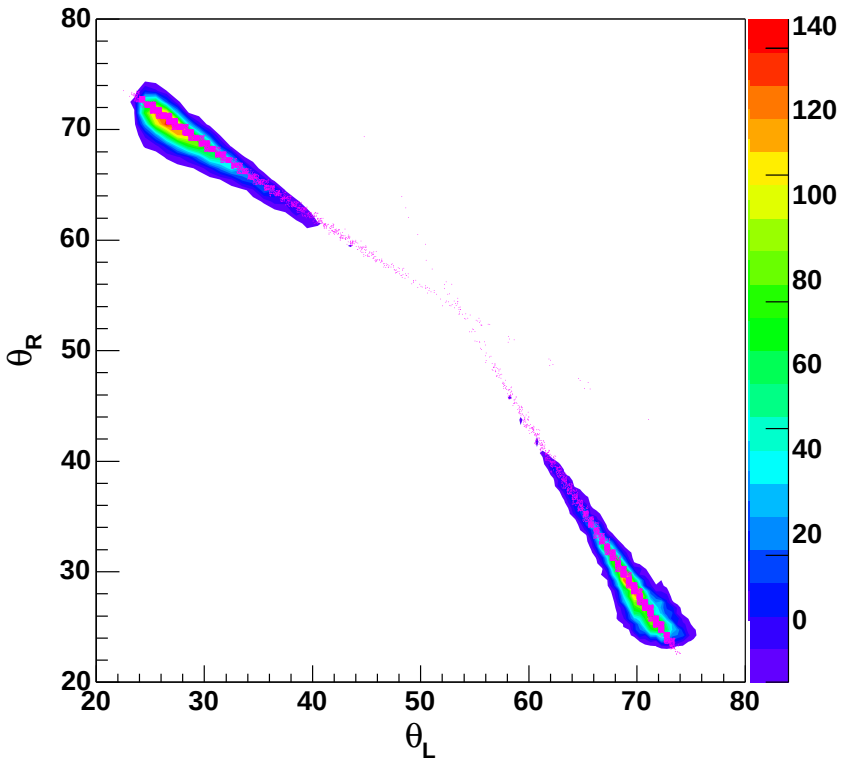

Figure 5-10: Quality of the elastic data as illustrated by comparision of the measured polar angles θ_R vs. θ_L where the overlayed magenta markers represent θ_q calculated from θ_e from the opposite sector

that is lacking in Figure 5-8. These corrections are

$$k_{LEFT} = 1.05 \times k_{LEFT} \tag{5.12}$$

$$k_{RIGHT} = 0.99 \times k_{RIGHT} \tag{5.13}$$

where k_{LEFT} and k_{RIGHT} are the momenta of an electron in the left and right sectors of BLAST respectively. A comparison of kinematics with and without these kinematic corrections applied is shown with Figures 5-11 and 5-12. One can see that $\omega - \omega_{CALC}$ the left hand plot in 5-11 is more symmetric about zero while the center plot of $P_d - P_{d,CALC}$ has only changed slightly in the peak and is still skewed by energy loss. In the right hand plot of each figure is the measured left polar angle θ_L versus the measured right polar angle θ_R. Overlayed is the polar angle θ_q calculated from θ_e in each sector. Here we see relatively good agreement regardless of the corrections. Because of the question surrounding their origin, no kinematic corrections have been employed in the analysis of the final extracted observables.

An example of a reconstructed elastic event is shown in Figure 5-13. The common

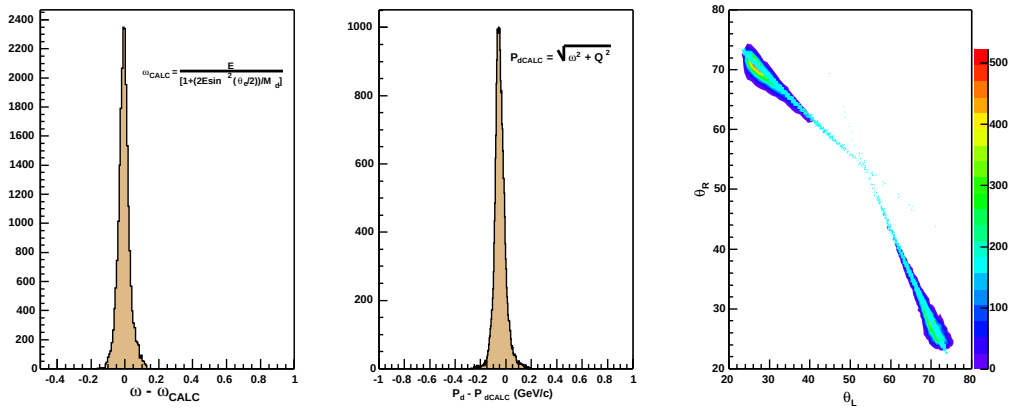

Figure 5-11: Kinematic quantites with corrections applied: From left to right: ω-ω_{CALC}, P_D-$P_{D,CALC}$, θ_L vs. θ_R where the cyan markers represent θ_q calculated from θ_e for each sector

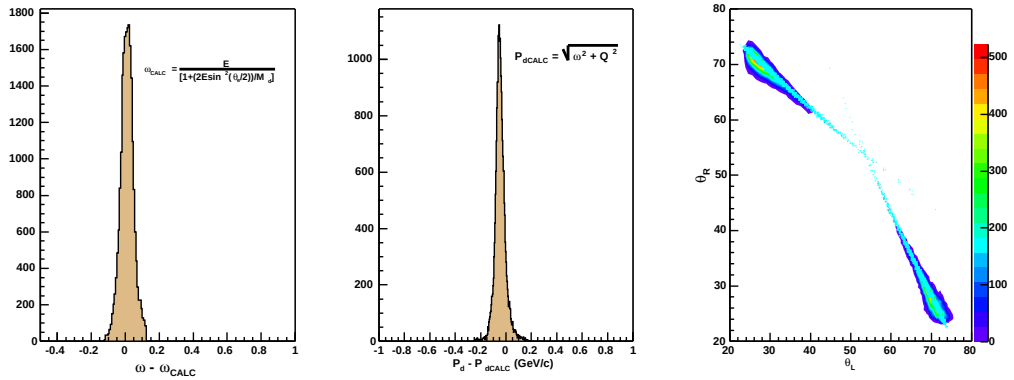

Figure 5-12: Kinematic quantites without corrections applied: From left to right: ω-ω_{CALC}, P_D-$P_{D,CALC}$, θ_L vs. θ_R where the cyan markers represent θ_q calculated from θ_e for each sector

vertex and correlation of forward and backward angles with the charge of the particles are characteristic of an elastic event. In the plan view the inbending track in the forward angle is the electron since the BLAST field was in inbending mode for this event. Note that the Čerenkov box corresponding to this track has fired supporting the notion that it is relativistic. The backward angle track that is outbending is the deuteron. In the upstream elevation view of the same event one can see that the tracks are very nearly coplanar in azimuth.

Much of this event selection relies on the elastic electron deuteron event selection of the T_{20} experiment [65] at BLAST since the same data are used. The cuts on the raw data between the two analyses are virtually the same, as they should be. The difference in the number of events passing all of the cuts on the data is approximately 3%.

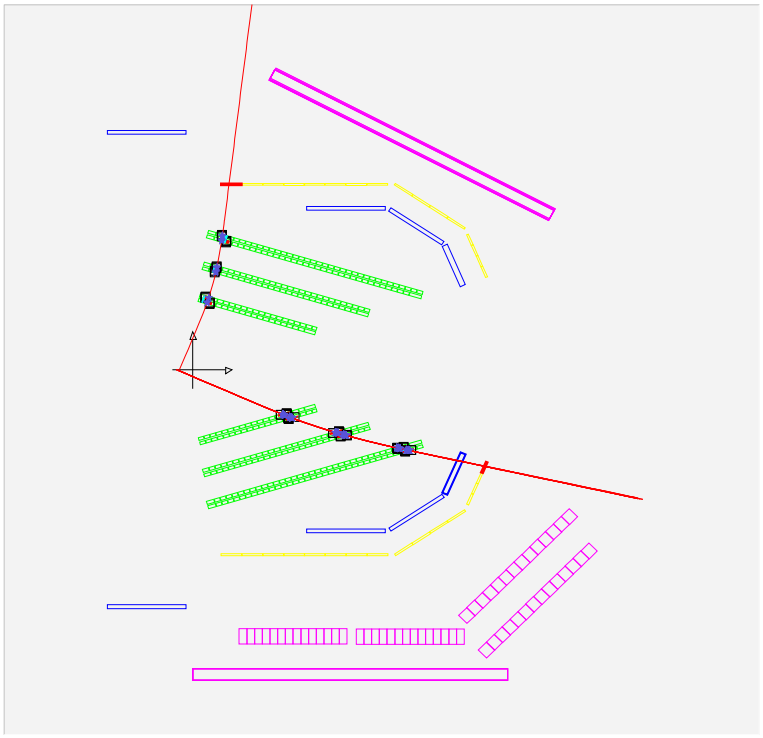

Figure 5-13: Reconstructed Elastic Event TOP View

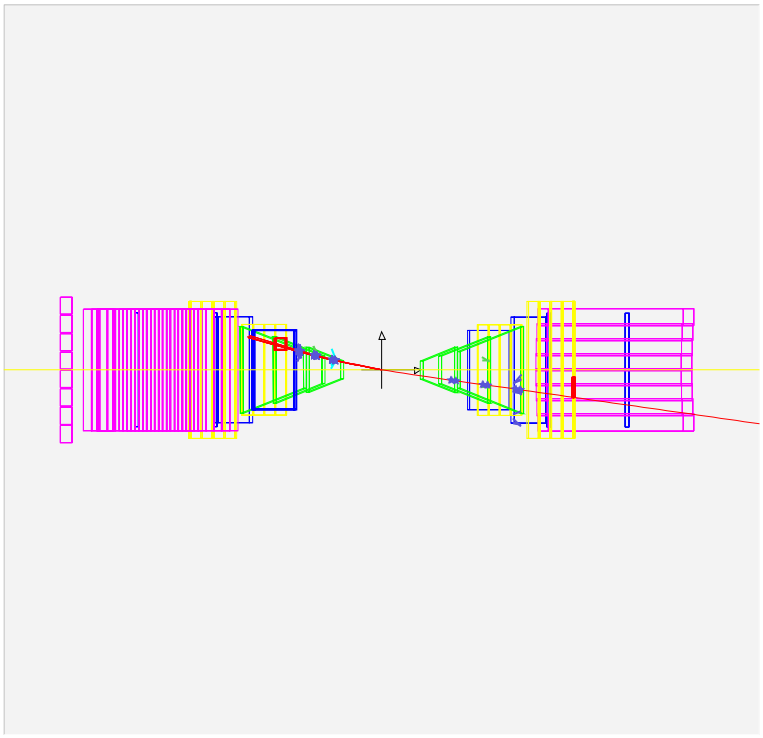

Figure 5-14: Reconstructed Elastic Event Upstream View

5.5 The Experimental Beam-Target Vector Asymmetry

5.5.1 Beam-Target Polarization States

The critical field B_c required for the decoupling of the deuteron hyperfine states is $\sim 117\ G$. This is well below the BLAST ABS holding field magnitude of $450\ G$ and thus allows for two-state injection. That is, to form the state $V+$, the injected hyperfine states are $|1\rangle$ and $|6\rangle$. The former is a pure state and not dependent on the critical field whereas the latter only contributes to the vector polarization at $B >> B_c$ where B is the applied field. The vector minus state $V-$ is formed by the dual injection of states $|3\rangle$ and $|4\rangle$. A summary of the target states, including those required for tensor polarization $\pm T$, is shown in Table 3.1[23].

Beam helicity, flipped once per fill, and target state, which was changed several times per fill, were digitized in a bit register ADC on an event by event basis [3]. These data were also written to scalers along with the accumulated beam-charge collected for each state.

5.5.2 A_{ed}^V in terms of beam-target states

One can form a beam-target asymmetry A_{ed}^V from the above states in terms of the cross section measured for each combination of beam, vector and tensor polarization. The six possible cross sections $\sigma(h, V, T)$ are summed to yield the total cross section σ_0.

$$\sigma_0 \ = \ \sigma(+,+,+1) + \sigma(-,+,+1) + \sigma(+,-,+1) + \sigma(-,-,+1) + \sigma(+,0,-2) + \sigma(-,0,-2) \tag{5.14}$$

[3] See Figure 3-2 for a description of the deuteron hyperfine states.

From equation 2.32 one can use a particular combination of these states to form the beam-target vector asymmetry.

$$A_{ed}^{V} \;=\; \frac{6}{4}\frac{1}{hP_z}\frac{1}{\sigma_0}[\sigma(+,+,+1) - \sigma(-,+,+1) - \sigma(+,-,+1) + \sigma(-,-,+1)] \tag{5.15}$$

where again P_z is the vector polarization of the target defined by

$$P_z \;=\; n_+ - n_- \tag{5.16}$$

where $n_\pm$ are the numbers of deuterons in the state $\pm V$. In practice, it is number of counts and not a pure cross section that is measured. To ensure proper normalization by charge, we define

$$\sigma_i(h,V,T) \equiv N_i\frac{\bar{q}}{q_i} \tag{5.17}$$

where N_i and q_i are the number of counts and the collected charge in state i and $\bar{q}$ is the average charge for each state.

$$\bar{q} \equiv \sum_i^6 \frac{q_i}{6} \tag{5.18}$$

Error on the Asymmetry

The statistical error on the asymmetry depends on the number of charge-normalized counts in each beam-target polarization state. That is, if we define $\sigma_i(h,V,T) \equiv N_i \cdot (\bar{q}/q_i)$ as the cross section of the i^{th} beam-target state where q_i is the integrated beam charge in state i, $\bar{q}$ is average charge in each state, and N_i is the number of counts in state i, then the error on the asymmetry, δ_A, is

$$\delta_A^2 \;=\; \sum_{i=1}^{6}\Big(\frac{\partial A}{\partial \sigma_i}\Big)^2 \delta\sigma_i^2 \tag{5.19}$$

where

$$\delta\sigma_i^2 \;=\; \Big(\frac{\partial\sigma_i}{\partial N_i}\Big)^2 \delta N_i^2 \;=\; \Big(\frac{\bar{q}}{q_i}\Big)^2 (\sqrt{N_i})^2 \tag{5.20}$$

assuming a poisson distribution of counts in each state.

An error in the product of the beam and target polarization, hP_z, will produce only a global shift up or down in the data and does not constitute an *independent* uncertainty on each data point. It was found that the $\sim 2\%$ error on hP_z produces a $\sim 2\%$ shift in the beam-target vector asymmetry.

5.5.3 Q^2 Bin Selection

The statistical error on the beam-target vector asymmetry, the vector polarization observables T_{10}^e and T_{11}^e, and the magnetic dipole form factor G_M, provided the impetus for choosing the number of bins in the independent variable Q^2 to be two. The proper value for Q^2 in each bin was specified as follows. The elastic electron-deuteron cross section, being in the *nbarn* regime even at low Q^2, limited the number of counts such that the Q^2 range be set as $0 < Q^2 < 0.4\ (GeV/c)^2$. A histogram of 200 bins was filled over this range and divided equally into two sections. In each section, the mean value of Q^2 was then determined. This determination of proper Q^2 values in each bin is illustrated in Figure 5-15

The beam-target vector asymmetry A_{ed}^V was built out of six two-bin histograms in Q^2 with each of these histograms for a particular beam-target polarization state. The Q^2 value for each of the two bins in A_{ed}^V, which was in the bin center by default, was then set to the mean Q^2 value for that bin as obtained above. For the case of the vector polarization observables, which require both left and right asymmetries, the average Q^2 of both sectors was taken for each bin.

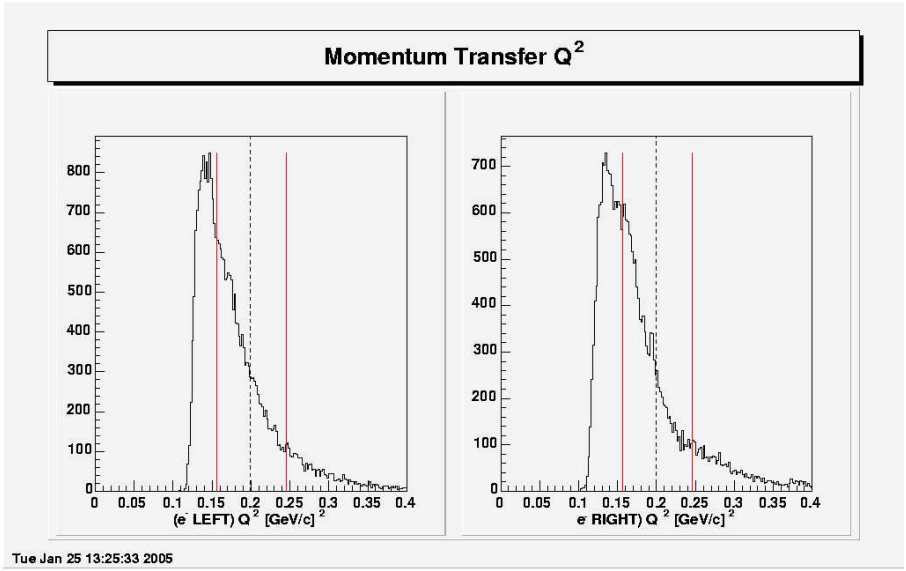

Figure 5-15: Finding the mean Q^2 for each bin

CHAPTER 6

Results and Discussion

The elastic vector polarization observables of the deuteron as provided by the BLAST experiment are the beam-target vector asymmetry A_{ed}^{V} and the analyzing powers T_{10}^{e} and T_{11}^{e}. From these, in combination with the world data for the structure function $A(Q^2)$, an extraction has been made of the magnetic dipole form factor G_M.

6.1 Measurement of the Beam-Target Vector Asymmetry

The magnetic holding field of the BLAST internal target was such that the polarization vector was oriented at an acute polar angle θ_T that was off the beam axis and in the BLAST yz-plane. This allowed for two simultaneous measurements to be made of the beam-target vector asymmetry. These were $A_{ed\perp}^{V}$, for the case of perpendicular kinematics and $A_{ed\parallel}^{V}$ for the case of parallel kinematics. In the former, the electron leaves a track in the left sector of BLAST while the momentum transfer $\mathbf{q}$, and hence the deuteron, are directed into the right sector. This means that $\mathbf{q}$ is nearly perpendicular to the target polarization vector which is nominally beam-left. The converse is true in the latter with the electron entering the right sector of BLAST and the deuteron entering the left with $\mathbf{q}$ nearly parallel to the target angle. As an example, parallel kinematics is illustrated in in Figure 6-1. In this figure the solid(dashed) straight red line corresponds to an electron in the right sector of BLAST while the wavy solid(dashed) line is the corresponding $\mathbf{q}$ vector directed into the

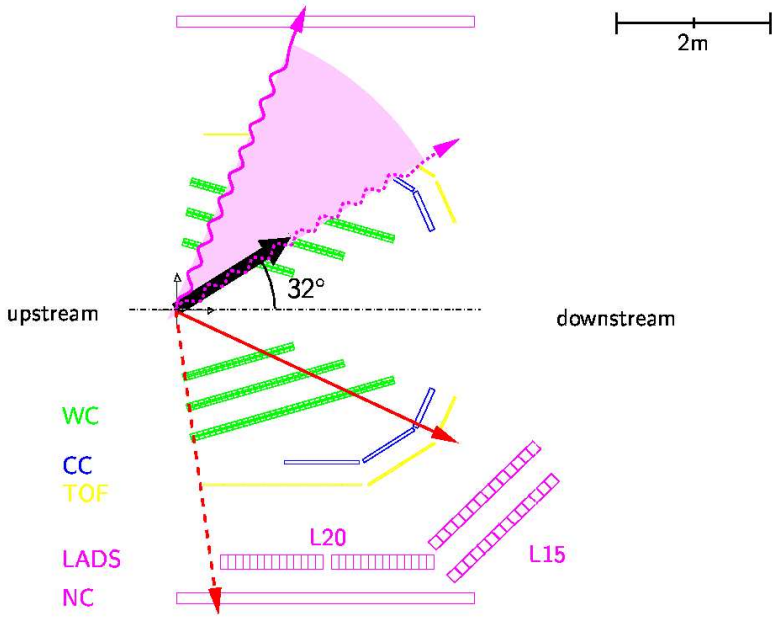

Figure 6-1: Parallel Kinematics: An electron is scattered into the right sector of BLAST while **q** is directed into the left sector. The converse is true in perpendicular kinematics where and electron is scattered into the left sector of BLAST while **q** is directed to the right.

left sector, approximately parallel to the target polarization vector.

These two measurements, defined by Equation 5.15 of the previous chapter, are shown in Figures 6-2, 6-3 and 6-4 for the case of a beam-left target polarization angle of 47° (May 2004), 32° (July-Sept 2004) and 47° (Spring 2005) respectively.

The curves in these plots are fitted asymmetries built out of parameterizations of the world data for the deuteron elastic form factors $G_C(Q^2)$, $G_Q(Q^2)$, and $G_M(Q^2)$ by Abbott [7]. Note that the BLAST data are statistically consistent with the asymmetries from these parameterizations. A key point in this consistency is that the parameterized asymmetry has been scaled by the product of the beam and target polarization, hP_z, for each target angle setting. The error on hP_z produces a *global* shift in the data and is on the order of 1.6% (statistical), 2.3% (systematic) and 0.7% (statistical), 2.9% (systematic) for the 2004 and 2005 datasets respectively. The combined dataset therefore has a relative systematic shift due to hP_z of 0.6% due to the statistical error on hP_z and of 1.8% due to the systematic error on hP_z. Since the values of hP_z were provided by the analysis of the BLAST data for the deuteron electrodisintegration channel $d(e,e'p)n$ [63], the independent measurement of the elastic channel asymmetry A_{ed}^V provides a cross check on the two reaction channels $d(e,e'd)$ and $d(e,e'p)n$ as measured by BLAST.

6.2 Extraction of T_{10}^e and T_{11}^e

Since two simultaneous measurements, $A_{ed\parallel}^V$ and $A_{ed\perp}^V$, were made for the beam-target vector asymmetry, two equations have been provided for the two unknown observables T_{10}^e

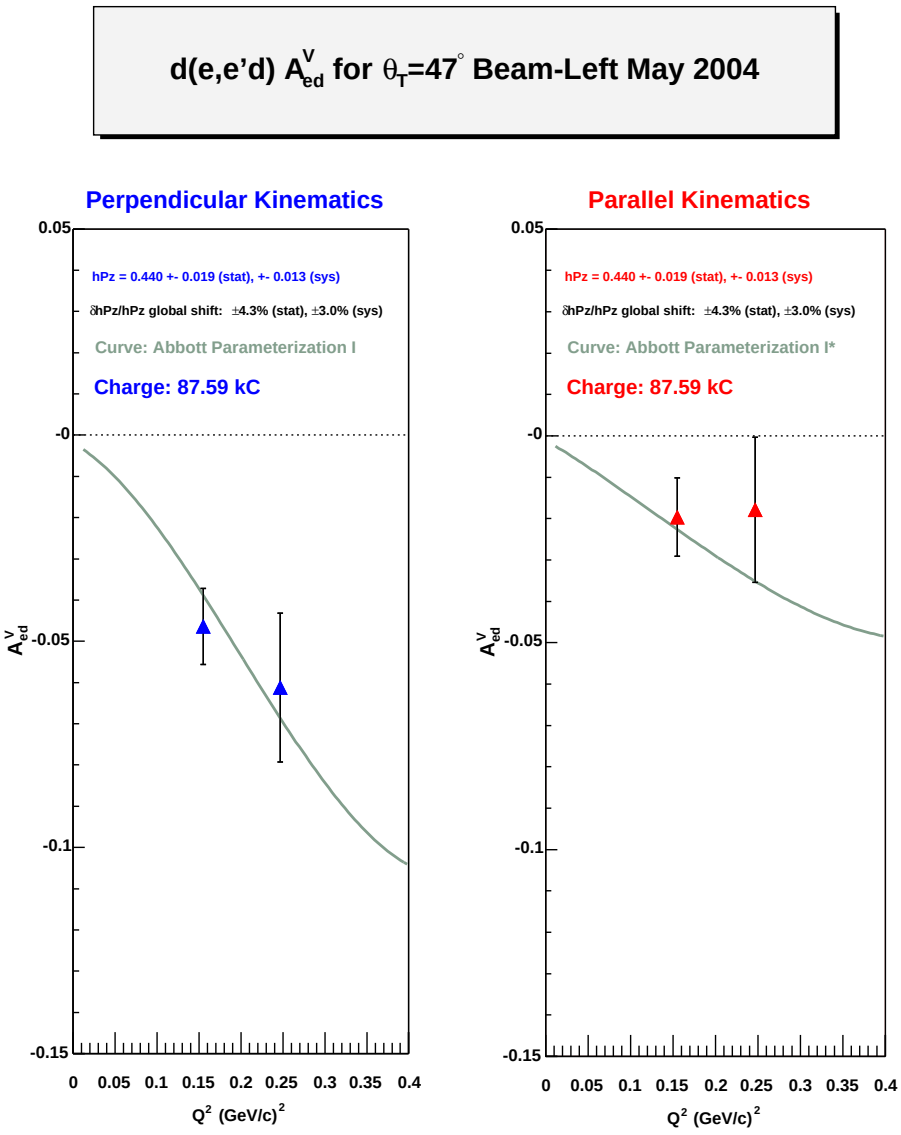

Figure 6-2: Beam-Target Vector Asymmetries $A^{ed}_{V\perp}$ and $A^{ed}_{V\parallel}$ for $\theta_T = 47°$ (May 2004)

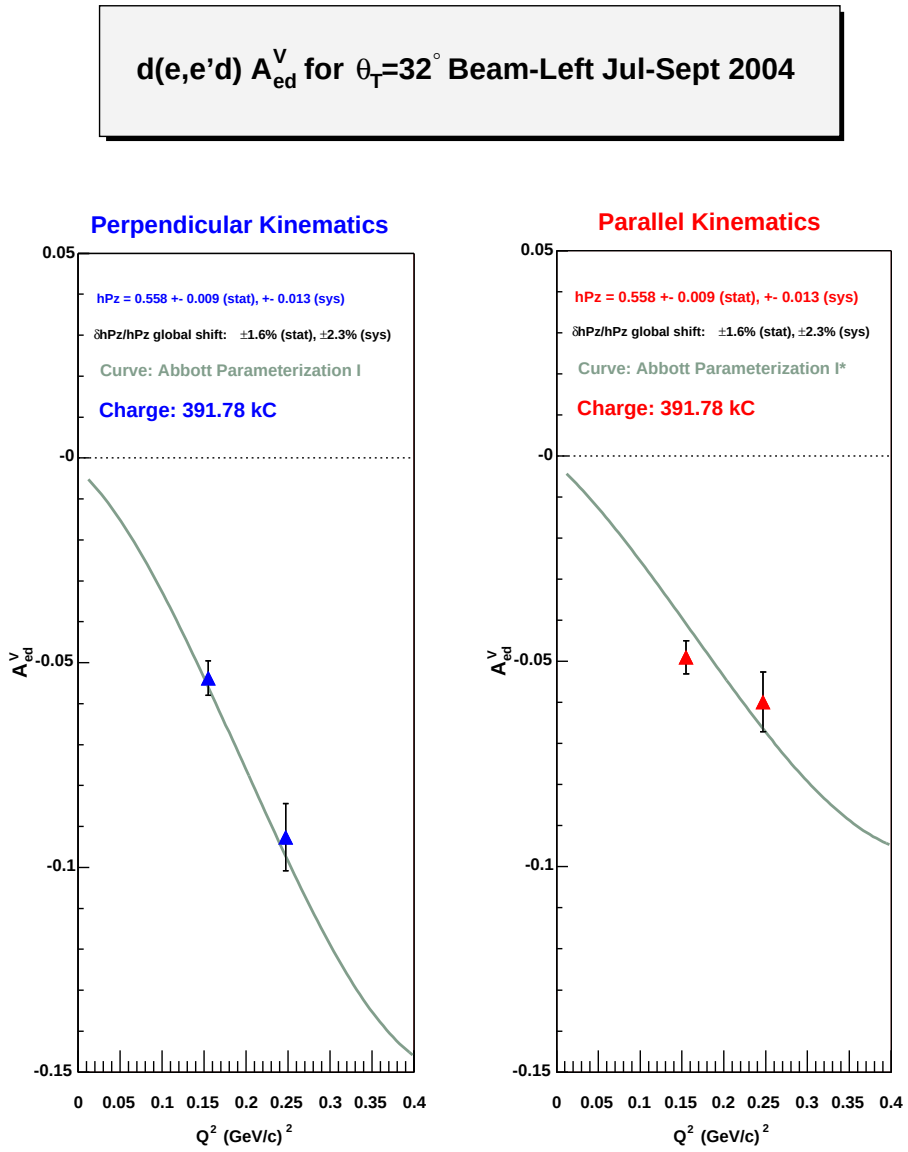

Figure 6-3: Beam-Target Vector Asymmetries $A_{V\perp}^{ed}$ and $A_{V\parallel}^{ed}$ for $\theta_T = 32°$ (July-Sept 2004)

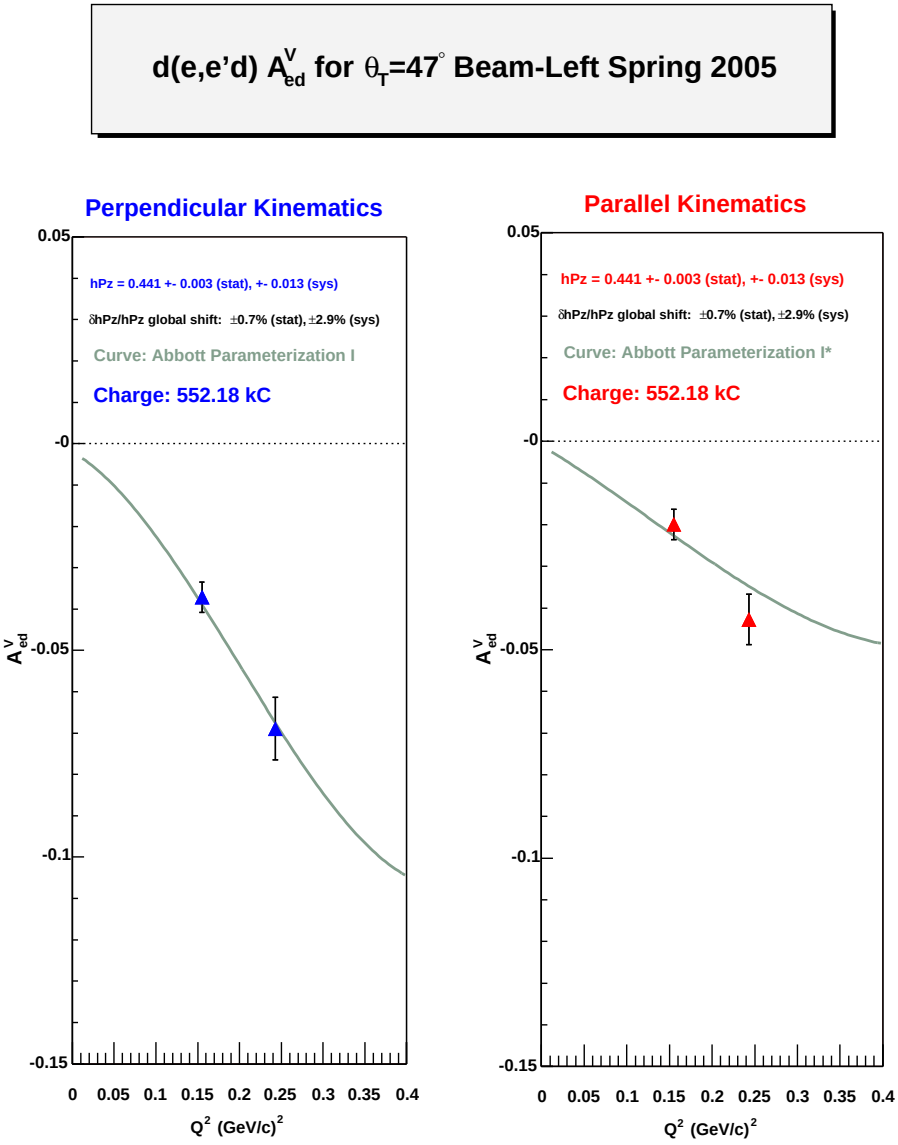

Figure 6-4: Beam-Target Vector Asymmetries $A_{V\perp}^{ed}$ and $A_{V\parallel}^{ed}$ for $\theta_T = 47°$ (Spring 2005)

and T_{11}^e[1] contained in the theoretical form of the asymmetry 2.33. That is we use

$$A_{ed\parallel}^V = hP_z\Big[\frac{1}{\sqrt{2}}\cos\theta_\parallel^* T_{10}^e(Q,\theta_e) - \sin\theta_\parallel^*\cos\phi_\parallel^* T_{11}^e(Q,\theta_e)\Big] \tag{6.1}$$

$$A_{ed\perp}^V = hP_z\Big[\frac{1}{\sqrt{2}}\cos\theta_\perp^* T_{10}^e(Q,\theta_e) - \sin\theta_\perp^*\cos\phi_\perp^* T_{11}^e(Q,\theta_e)\Big] \tag{6.2}$$

to extract T_{10}^e and T_{11}^e. Doing this we find

$$T_{10}^e = -\frac{1}{hP_z}\sqrt{\frac{2}{3}}\Big[\frac{\sin\theta_\parallel^*\cos\phi_\parallel^* A_{ed\perp}^V - \sin\theta_\perp^*\cos\phi_\perp^* A_{ed\parallel}^V}{\cos\theta_\parallel^*\sin\theta_\perp^*\cos\phi_\perp^* - \cos\theta_\perp^*\sin\theta_\parallel^*\cos\phi_\parallel^*}\Big] \tag{6.3}$$

$$T_{11}^e = \frac{1}{hP_z}\frac{\sqrt{3}}{3}\Big[\frac{\cos\theta_\parallel^* A_{ed\perp}^V - \cos\theta_\perp^* A_{ed\parallel}^V}{\cos\theta_\perp^*\sin\theta_\parallel^*\cos\phi_\parallel^* - \cos\theta_\parallel^*\sin\theta_\perp^*\cos\phi_\perp^*}\Big] \tag{6.4}$$

where $\theta_{\perp,\parallel}^*$ and $\phi_{\perp,\parallel}^*$ are defined in the following section.

6.2.1 Calculating θ^* and ϕ^* for BLAST

To obtain θ^* and ϕ^* for the extraction of T_{10}^e and T_{11}^e, two rotations in 3-space must be conducted. The first is a rotation about the beam (z) axis by the angle of azimuth ϕ_e. This takes one from the BLAST frame to the scattering frame. A second rotation is then applied about the y-axis of the scattering frame so that the scattering frame z-axis aligns with the three-momentum vector $\mathbf{q}$. To illustrate this consider the target spin unit vector in the BLAST frame, $\hat{S^B}$, as shown in Figure 6-5.

$$\hat{S}^B = \begin{pmatrix} \hat{x}^B \\ \hat{y}^B \\ \hat{z}^B \end{pmatrix} \rightarrow \begin{pmatrix} \sin\theta_T \\ 0 \\ \cos\theta_T \end{pmatrix} \tag{6.5}$$

The scattering frame is that which has the x and z axes coplanar with the beam axis, the scattered electron momentum vector, and the three momentum vector $\mathbf{q}$. To transform

[1] At times $T_{10}^e(Q^2)$ and $T_{11}^e(Q^2)$ are designated in the shorthand T_{1q}^e where $q = 0, 1$

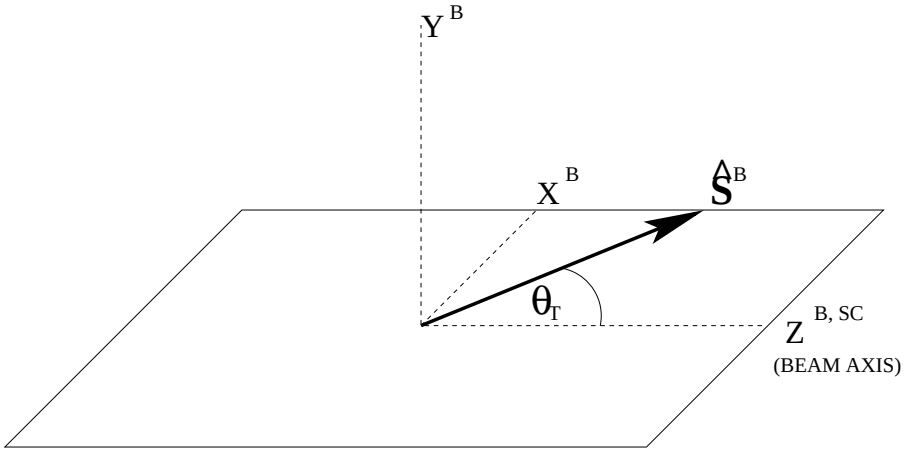

Figure 6-5: The BLAST Frame

from the BLAST frame to the scattering frame we rotate about the z-axis (i.e. the beam axis) by the angle of azimuth ϕ_e with the matrix

$$R_z^{SC}(\phi_e) \;=\; \begin{pmatrix} \cos\phi_e & \sin\phi_e & 0 \\ -\sin\phi_e & \cos\phi_e & 0 \\ 0 & 0 & 1 \end{pmatrix} \tag{6.6}$$

As shown in Figure 6-6, the spin vector in the scattering frame is then

$$\hat{S}^{SC} \;=\; R_z^{SC}(\phi_e)\hat{S}^B \;=\; \begin{pmatrix} \cos\phi_e \sin\theta_T \\ \sin\phi_e \sin\theta_T \\ \cos\theta_T \end{pmatrix} \tag{6.7}$$

A rotation around the y-axis of the scattering frame by the angle $\theta_{\mathbf{q}}$ aligning the z-axis with the **q**-vector takes one from the scattering frame to the physics, or what we shall

designate as Q, frame. This is shown in Figure 6-7.

$$\hat{S}^Q \;=\; R_y^Q(\theta_{\mathbf{q}})\hat{S}^{SC} \;=\; \begin{pmatrix} \cos\theta_{\mathbf{q}}\cos\phi_e\sin\theta_T + \sin\theta_{\mathbf{q}}\cos\theta_T \\ -\sin\phi_e\sin\theta_T \\ -\sin\theta_{\mathbf{q}}\cos\phi_e\sin\theta_T + \cos\theta_{\mathbf{q}}\cos\theta_T \end{pmatrix} \;=\; \begin{pmatrix} \hat{S}_x^Q \\ \hat{S}_y^Q \\ \hat{S}_z^Q \end{pmatrix} \tag{6.8}$$

From Figure 6-8 we see that we can write

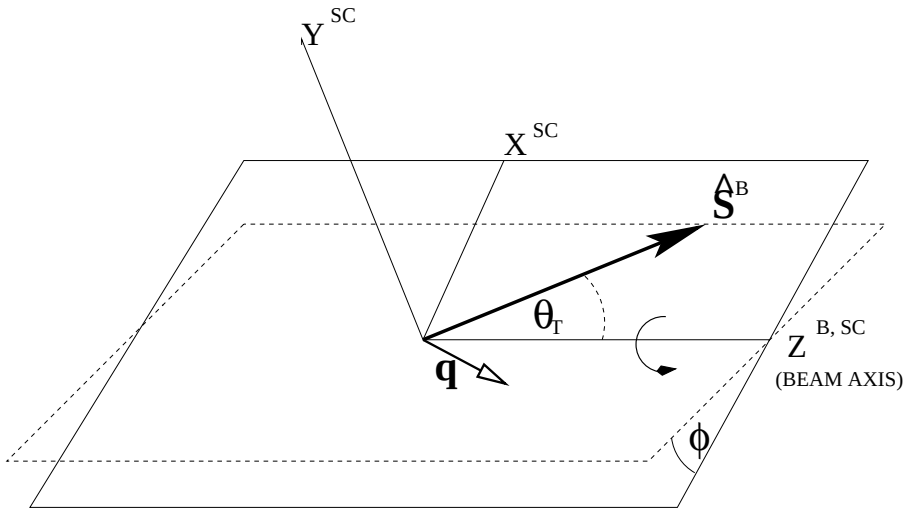

Figure 6-6: Rotating from the BLAST to Scattering Frame

$$\begin{pmatrix} \hat{S}_x^Q \\ \hat{S}_y^Q \\ \hat{S}_z^Q \end{pmatrix} \;=\; \begin{pmatrix} |\hat{S}^Q|\sin\theta^*\cos\phi^* \\ |\hat{S}^Q|\sin\theta^*\sin\phi^* \\ |\hat{S}^Q|\cos\theta^* \end{pmatrix} \tag{6.9}$$

From this we can obtain θ^* and ϕ^* in terms of BLAST variables.

$$\theta^* \;=\; \cos^{-1}\Big(\frac{S_z^Q}{|\hat{S}^Q|}\Big) \;=\; \cos^{-1}(\cos\theta_{\mathbf{q}}\cos\theta_T - \sin\theta_{\mathbf{q}}\cos\phi_e\sin\theta_T) \tag{6.10}$$

$$\phi^* \;=\; \sin^{-1}\Big(\frac{S_y^Q}{|\hat{S}^Q|\sin\theta^*}\Big) \;=\; \sin^{-1}\Big(\frac{-\sin\phi_e\sin\theta_T}{\sin\theta^*}\Big) \tag{6.11}$$

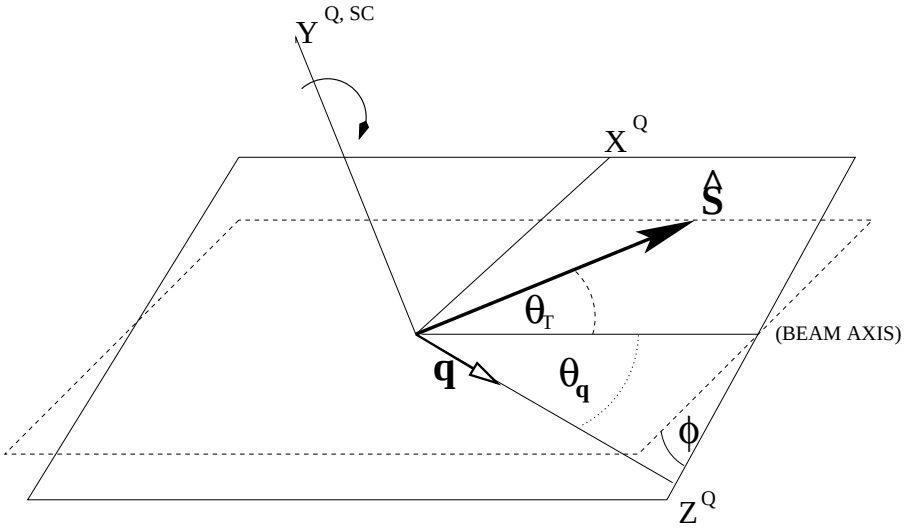

Figure 6-7: Rotating from the Scattering Frame to the Q (Physics) Frame

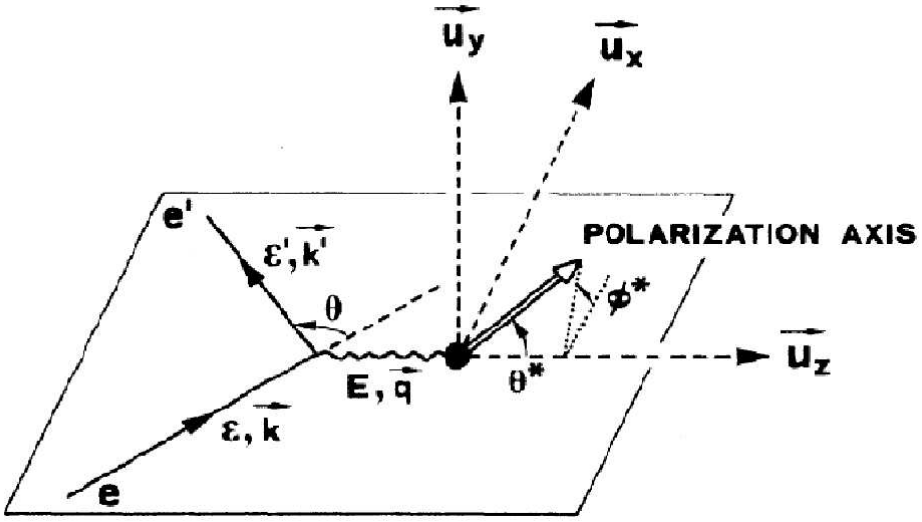

Figure 6-8: The Physics Coordinate System

For the case of elastic scattering, $\theta_{\mathbf{q}}$ can be written in terms of θ_e as in equation 2.41. Also, the apparent covariance between θ^* and ϕ^* is removed upon insertion of 6.10 into the denominator of 6.11.

Once the mean value of Q^2 was determined for each bin as described in Section 5.5.3 of the previous chapter, θ^* was calculated using 6.10 based on this mean value of Q^2. The angle ϕ^* was then obtained using this value of θ^* as well as the mean value of the azimuthal angle ϕ_e.

6.3 Error Analysis on T^e_{10} and T^e_{11}

6.3.1 Statistical Errors from A^V_{ed}

Since the statistics of T^e_{1q} are contained in the beam-target vector asymmetries $A^{ed}_{V,\parallel}$ and $A^{ed}_{V,\perp}$, these were the sole source of statistical error in the measurement of the vector polarization observables. Error propagation on T^e_{10} and T^e_{11} yields

$$\delta^{2\,(STAT)}_{T1q} \;=\; \Big(\frac{\partial T^e_{1q}}{\partial A_\parallel}\Big)^2 \delta^2_{A_\parallel} + \Big(\frac{\partial T^e_{1q}}{\partial A_\perp}\Big)^2 \delta^2_{A_\perp} \tag{6.12}$$

where $\delta^2_{A_\parallel}$ and $\delta^2_{A_\perp}$ are taken from equations 5.19.

6.3.2 Systematic Errors

Other than the measured asymmetries, T^e_{10} and T^e_{11} depend only on the angles θ^* and ϕ^*. Therefore the main contributors to the systematic errors in these observables are the polarization target angle θ_T, and the reconstructed polar and azimuthal angles θ_e and ϕ_e respectively. These are intrinsic in the propagation of errors in the vector polarization observables.

$$\delta^{2\,(SYS)}_{T1q} \;=\; \Big(\frac{\partial T^e_{1q}}{\partial \theta^*_\perp}\Big)^2 \delta^2_{\theta^*_\perp} + \Big(\frac{\partial T^e_{1q}}{\partial \theta^*_\parallel}\Big)^2 \delta^2_{\theta^*_\parallel} + \Big(\frac{\partial T^e_{1q}}{\partial \phi^*_\parallel}\Big)^2 \delta^2_{\phi^*_\parallel} + + \Big(\frac{\partial T^e_{1q}}{\partial \phi^*_\perp}\Big)^2 \delta^2_{\phi^*_\perp} \tag{6.13}$$

It is not clear that the independent sources of systematic error should be added in quadrature. Instead a study was performed shifting each of these systematic sources by its respective uncertainty and observing the shift in the observables T_{10}^e and T_{11}^e. The resulting systematic errors are shown in Table 6.7.

Note that there is no contribution to the systematic error from the vector polarization asymmetries. Also note that the effect of the uncertainty in the product of the beam and target polarizations, hP_z is not taken into account. As in the case of the asymmetries, it is not addressed here as it constitutes a global shift in the measurements and not an *independent* uncertainty on each data point. However, this global shift due to hP_z is accounted for in the presentation of the results.

6.3.3 Interpreting the T_{1q} Data

The BLAST data for the measurement of T_{10}^e and T_{11}^e are shown in Figures 6-9 and 6-10 respectively. The data are summarized in Section 6.8. The error bars on the data points are statistical while the systematic errors are displayed separately. Note that the overall error on these observables is dominated by statistics.

To our knowledge, this measurement of T_{10}^e and T_{11}^e from double polarization asymmetries is the first of its kind. Comparison with the world data therefore must be estimated through the indirect construction of T_{10}^e and T_{11}^e via equations 2.27 and 2.28. Herein, the first parameterization of the world data on the form factors G_C, G_Q, and G_M by Abbott [7] is used to estimate these observables over our Q^2 range. T_{10}^e and T_{11}^e as obtained in this manner are represented by the green curves in Figures 6-9 and 6-10.

In addition to the Abbott parameterization, we have in Figures 6-9 and 6-10 the theoretical predictions of the vector polarization observables by Arenhövel [30] and Phillips [15]. The former, which makes use of the Bonn Qb potential [69], has been disseminated into the various contributions that comprise the full theoretical prediction. The latter effective field theory (EFT) calculation is based in chiral perturbation theory where the

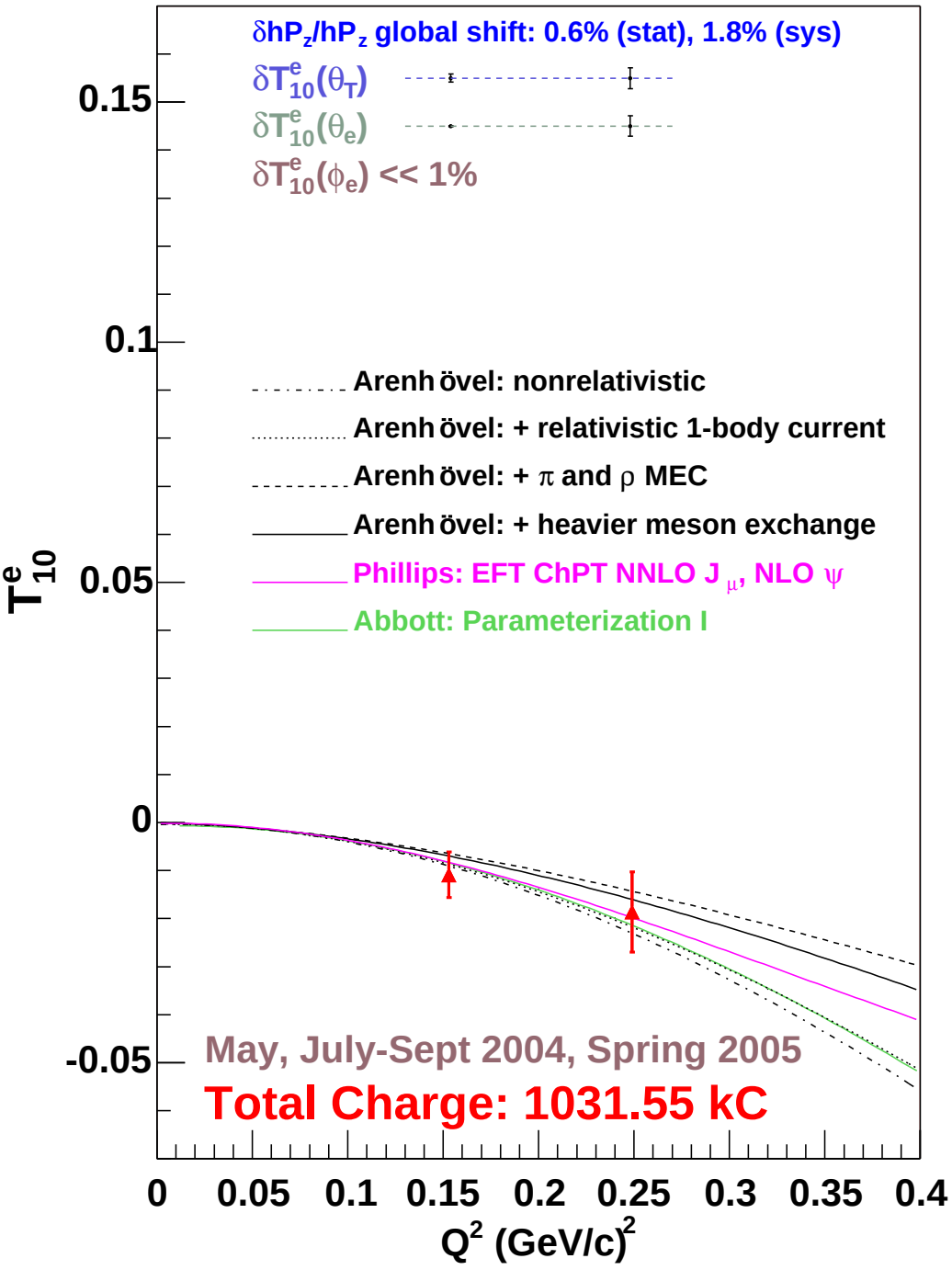

Figure 6-9: The BLAST Measurment of the Vector Analyzing Power T^e_{10}

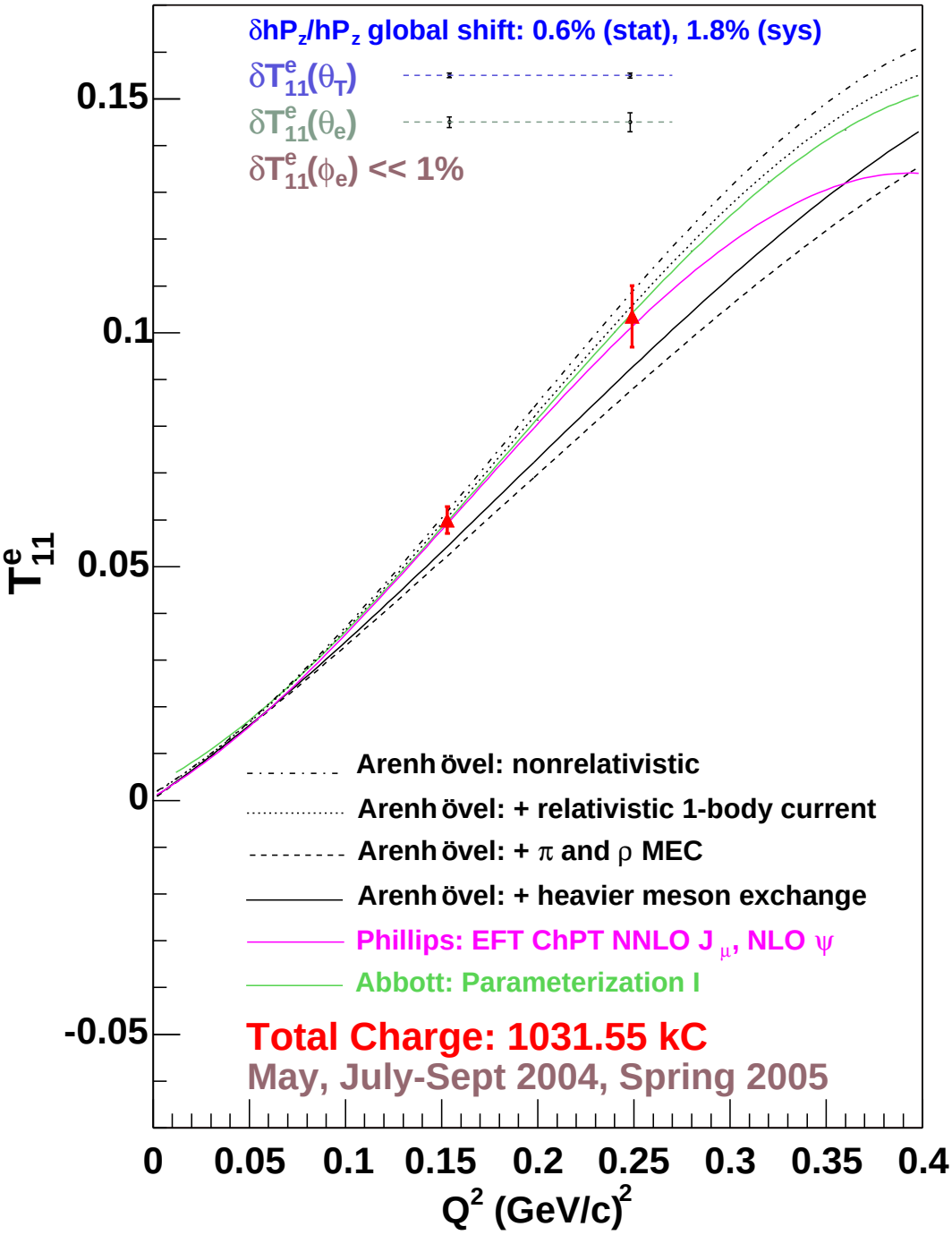

Figure 6-10: The BLAST Measurment of the Vector Analyzing Power T_{11}^e

current operator is computed to next-to-next-to leading order (NNLO) and the NN potential (deuteron wave function) is computed to NLO.

The observable T_{10}^e is of such small magnitude that, even with $\sim$ 1 MC of beam-integrated charge, a statistically significant measurement of it can not really be made with the current amount of BLAST data. That is, even though a trend is seen in these data to follow the general direction of the Abbott parameterization and the theoretical predictions of Arenhövel and Phillips, the statistical error bars are sufficiently large so as to span the model dependence at both Q^2 points of measurement.

In the case of T_{11}^e, however, the larger relative magnitude of this observable is such that, with the statistics collected in the BLAST experiment, a significant measurement has indeed been made. Again we see a general agreement between the theoretical predictions, the Abbott parameterization, and the BLAST data. Here however, the error on T_{11}^e is small enough so that the data begin to constrain the theoretical predictions. Specifically, T_{11}^e is in statistical agreement with the non-relativistic (NR) and NR+1-body current contributions from Arenhövel. Meson exchange currents (MECs), on the other hand, seem to play a part that is inconsistent with the BLAST measurement in this Q^2 region. Also, below $\sim$ 0.25 $(GeV/c)^2$, Phillips EFT calculation has a slope that is comparable with the above mentioned Arenhövel models. This leaves Phillips in good agreement with the BLAST data as well in this regime. Above this point, the Phillips calculation seems to change slope in a more marked fashion warranting more data in this region to address this divergence. Lastly, in the BLAST measurement Q^2 range, the Abbott parameterization falls between the aforementioned models of Arenhövel and Phillips. This provides empirical reinforcement that the BLAST measurement is consistent with the world data on the form factors G_C, G_Q, and G_M.

6.4 Extracting the Elastic Magnetic Dipole Form Factor G_M

As will be seen, the magnetic dipole form factor G_M is strongly correlated with the vector polarization observable T_{11}^e. For this reason, we can use the BLAST data on T_{11}^e in an extraction of G_M as described below.

In addition to the vector polarization observables T_{10}^e and T_{11}^e, the BLAST experiment has provided data for the target tensor polarization observables T_{20} and T_{21}. Ideally, these four measurements would overconstrain the form factors G_C, G_Q, and G_M. However, from the current data on T_{10}^e and T_{11}^e it is evident that the former will not be useful in this regard as it is a small enough effect that it is very nearly statistically consistent with zero. In lieu of T_{10}^e we make use of the structure function $A(Q^2)$ which is known to high precision in the low Q^2 range [7]. Incidentally, one notices from the form of $A(Q^2)$ in 2.17 that the kinematic factor $\tau = Q^2/4M_d^2$ mitigates the contribution of G_M, and more so of G_Q, leaving $A(Q^2)$ to be dominated by G_C in the low Q^2 region.

With the above in mind, we proceeded to vary the form factors and conduct a χ_ν^2 minimization where the four observables T_{11}^e, T_{20}, T_{21}, $A(Q^2)$, and the three parameters, G_C, G_Q, and G_M, leave us with one degree of freedom. That is, we formed

$$\chi_\nu^2 = \frac{1}{\nu}\sum\left\{\frac{1}{\sigma_i^2}[f_i - f(Q_i^2)]\right\} \tag{6.14}$$

$$f = \{T_{11}^e, T_{20}, T_{21}, A(Q^2)\} \tag{6.15}$$

where $\nu = 1$ degree of freedom, f_i are the measured values of the observables, σ_i are the uncertainties in those measurements, and $f(Q_i^2)$ are the values of the functions for each observable at the i^{th} value of Q^2.

To obtain values for T_{20}, T_{21}, and $A(Q^2)$ at the Q^2 points of the BLAST T_{11}^e measurements, we fit the data of these former three measurements and used the functional form to determine the values of these observables. This is discussed in the following sections.

6.4.1 Fitting the World Data for $A(Q^2)$

Over our Q^2 range of interest the available data for $A(Q^2)$ are mainly from measurements at Saclay [5] with a few high precision points from Mainz [6] in the lower end of the region. It is here that we note the discrepancy, on the order of $\sim 8\%$, between the Saclay and Mainz data. This is in effect a source of systematic error in the extraction of the magnetic dipole form factor. To address this discrepancy, we first fit the Saclay data as it spans our entire Q^2 region of interest, and then scale this functional form in a least squares fit of the Mainz data. This provides us with one value of $A(Q^2)$ at $Q^2 = 0.248$ $[GeV/c]^2$ based on Saclay, and two values of $A(Q^2)$, based on Saclay and Mainz, at the lower Q^2 point of 0.154 $[GeV/c]^2$.

The best fit of the Saclay data was achieved with a functional form of

$$y(Q^2) \;=\; a_0 \cdot Q^2 + a_1 \cdot e^{-a_2 \cdot Q^2} \tag{6.16}$$

A Taylor expansion of this fitting function to second order about the parameter a'_j, defined in terms of the parameter increment $\delta a_j = a_j - a'_j$, yields the inverse of the error matrix $\boldsymbol{\epsilon = \alpha^{-1}}$, [70]

$$\alpha_{jk} \;\equiv\; \sum \frac{1}{\sigma_i^2}\Big[\frac{\partial y'(Q_i^2)}{\partial a_j}\frac{\partial y'(Q_i^2)}{\partial a_k} - [y_i - y'(Q_i^2)]\frac{\partial^2 y'(Q_i^2)}{\partial a_j \partial a_k}\Big] \tag{6.17}$$

where y' is the value of the fitting function evaluated at the initial parameter values a'_j, y is the function evaluated at the true values of the parameters a_j, and σ_i are the errors on the world data for the i^{th} Q^2 point.

The fit of $A(Q^2)$ for the Saclay data, and the scaling of this fit to the Mainz data are shown in Figure 6-11. The red markers are the interpolated values at the Q^2 points of the BLAST T_{11}^e measurement. The interpolated values of $A(Q^2)$ were found to be 0.03265±8.0E-05 at 0.154 [GeV/c]^2 and 0.00845±9.9E-05 at 0.248 [GeV/c]^2 from the

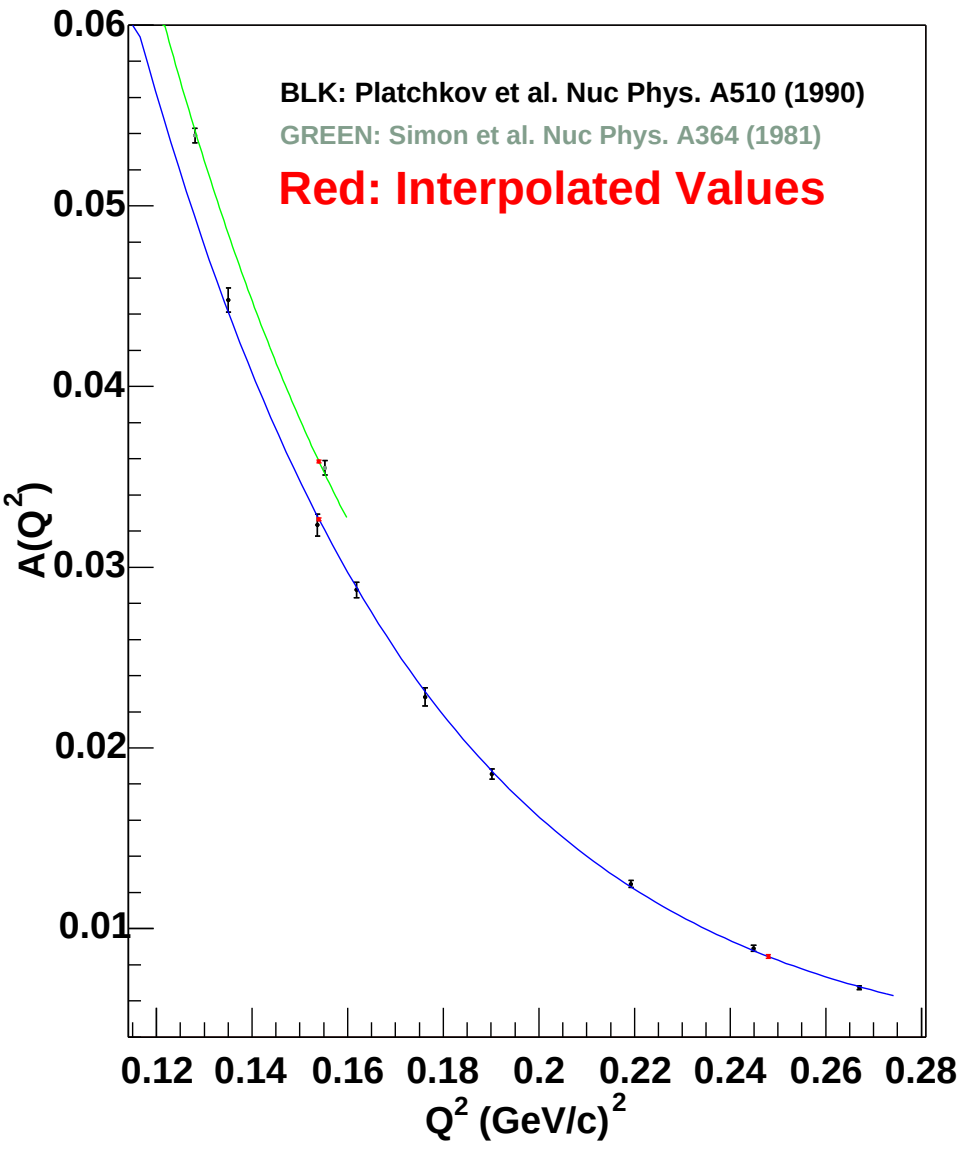

Figure 6-11: Fitting the World Data for $A(Q^2)$

Saclay data and 0.03585±8.0E-05 at 0.154 $[\mathrm{GeV/c}]^2$ from the Mainz data.

6.4.2 Fitting the BLAST T_{20} and T_{21}

The BLAST data for the target tensor polarization observables T_{20} and T_{21} [4] which are shown in Figure 6-12 cover an extensive region in Q^2 of which only a portion below

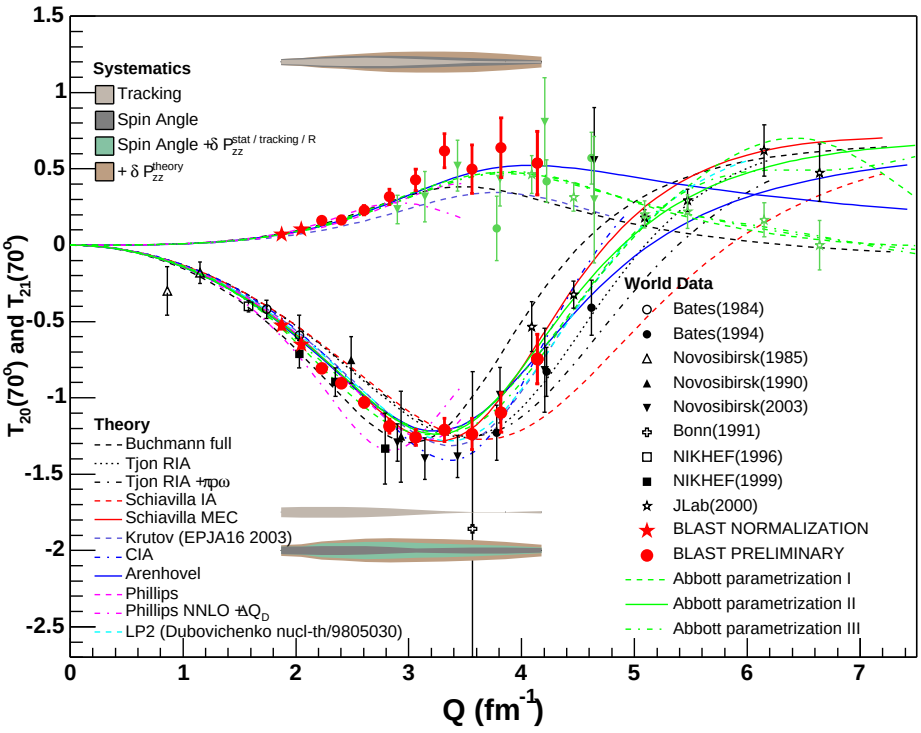

Figure 6-12: The BLAST data (in red) for the tensor analyzing powers T_{20} and T_{21} [4]

0.4 $[GeV/c]^2$ was required for this analysis. These data were fitted with second order polynomials and the errors on the fits were again determined from the full covariant error matrix $\boldsymbol{\epsilon} = \boldsymbol{\alpha}^{-1}$, where, in this case [70]

$$\alpha_{jk} \equiv \sum \left[\frac{1}{\sigma_i} f_j(Q_i^2) f_k(Q_i^2) \right] \tag{6.18}$$

where $f_0 = 1$, $f_1 = Q^2$, $f_2 = (Q^2)^2$. The fits to T_{20} and T_{21} are shown in Figure 6-13, where again the red markers are those values of these observables at our Q^2 points of interest. The interpolated values were found to be T_{20} =-0.59558±0.010128 and T_{21} =-0.09760±0.01360 at Q^2 =0.154 [GeV/c]^2 and T_{20} =-0.94234±0.01240 and T_{21} =-0.22269±0.01924 at Q^2 =0.248 [GeV/c]^2.

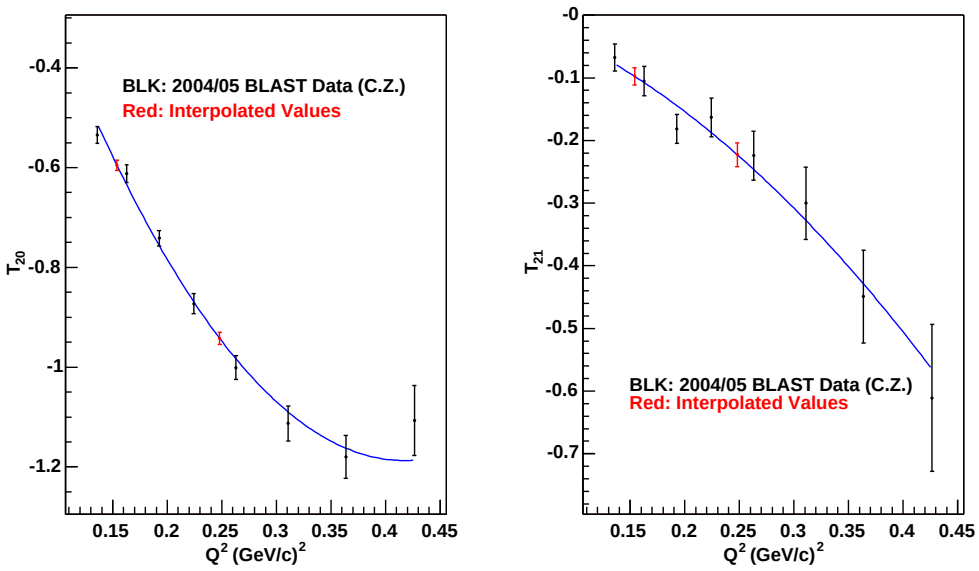

Figure 6-13: Fitting the BLAST Data for T_{20} and T_{21} at low Q^2 [4]

6.4.3 χ^2_ν Distribution of G_C, G_Q, and G_M

The three form factors G_C, G_Q, and G_M, serving as parameters in this χ^2_ν reduction, were varied through all possible values to one part in a thousand over their respective ranges. That is, G_C, G_Q, and G_M were each varied independently in nested loops from zero to 1.0, 25.83, and 1.714 respectively in step sizes equal to one thousandth of their respective ranges. The distribution of χ^2_ν versus each of these parameters at both Q^2 points are shown in Figure 6-14. For each value of each form factor there exists a multitude of

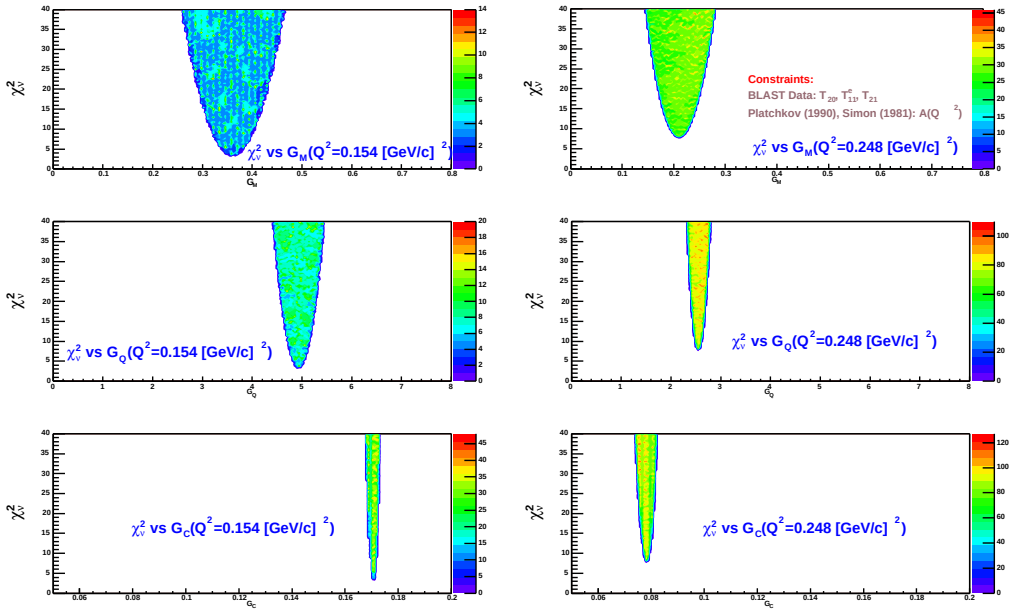

Figure 6-14: χ^2_ν Distribution versus G_C, G_Q, and G_M

values of χ^2_ν corresponding to the variation of the other two, thus resulting in the filled parabolas shown in Figure 6-14. For example, for each value of G_M, there are many combinations of G_C and G_Q which produce a wide variety of values for χ^2_ν. Additionally, the number of solutions for each combination of parameters is not spread evenly over the χ^2_ν distribution and concentrations of solutions manifest themselves as peaks or ridges, indicated by the color scale, out of the page.

We then fit the lower edge of the χ^2_ν distribution parabola which corresponds to a local[2] minimum in χ^2_ν for each parameter. We thus determine the exact parabolic form of each distribution to better identify the global minimum corresponding to the best value of that parameter. The fits for each of the parameters, at each Q^2 point are shown in Figure 6-15 and the results for the form factors are summarized in Section 6.8.

[2]Here a local minimum is local with respect to G_M (or G_C or G_Q depending against which parameter one plots X^2_ν)

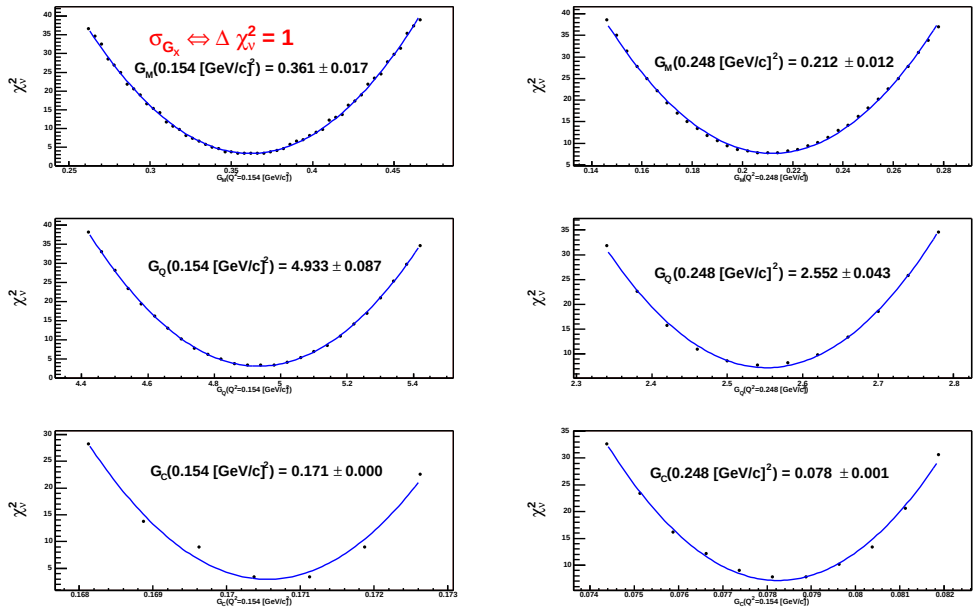

Figure 6-15: χ^2_ν Distribution Local Minima for G_C, G_Q, and G_M

6.4.4 Statistical and Systematic Errors

Only statistical errors for T^e_{11}, T_{20}, T_{21}, and $A(Q^2)$ were used in the determination of the parameters G_C, G_Q, and G_M. The statistical error, therefore, in each of these parameters, at each Q^2 point, is that variation in the parameter that causes a change of $\Delta\chi^2_\nu = 1$. If we vary each parameter a_j by an arbitrary amount Δa_j, and then define [70]

$$\chi^2_1 \equiv \chi^2(a_j - \Delta a_j) \tag{6.19}$$

$$\chi^2_2 \equiv \chi^2(a_j) \tag{6.20}$$

$$\chi^2_3 \equiv \chi^2(a_j + \Delta a_j) \tag{6.21}$$

$$\tag{6.22}$$

then the error on the respective parameter is [70]

$$\sigma_j \;=\; \Delta a_j \sqrt{2(\chi_1^2 - 2\chi_1^2 + \chi_3^2)^{-1}} \tag{6.23}$$

To obtain the systematic errors on G_M we applied the same method as in the case of T_{10}^e and T_{11}^e. In this case, however, we exchanged the negligible $\delta G_M(\phi_e)$ for the systematic error due to the tensor polarization P_{zz} which enters our analysis through the use of T_{20}. We thus varied independently θ_T, θ_e, and P_{zz} by their respective uncertainties and observed the systematic shift in G_M.

6.5 Interpreting the G_M Data

The extracted values of the magnetic dipole form factor G_M, where $A(Q^2)$ is taken from a fit of the Saclay data only, are shown in Figure 6-16. The error bars on the data points are statistical while the systematic errors are displayed separately.

G_M as obtained using the $A(Q^2)$ from Mainz [6] for the low Q^2 point is shown, with the high Q^2 point still using the Saclay data [5], in Figure 6-17. Note how G_M as found with the Mainz value for $A(Q^2)$ is higher than the corresponding Saclay based point but that it still resides within one standard deviation of the latter.

The non-intuitive manifestation of larger statistical error bars on the lower Q^2 point of G_M is due to dependence of G_M on T_{11}^e as shown in Equation 2.28. Through standard error propagation one finds that the partial rate of change of G_M with respect to T_{11}^e, $(\partial G_M/\partial T_{11}^e)$, is equivalent to G_M/T_{11}^e. At lower Q^2, the magnitude of G_M increases while that of T_{11}^e decreases. This dominates the error and produces the observed effect.

Again the data are plotted against the theoretical predictions of Arenhövel and Phillips as well as the parameterization of the world data by Abbott. It is interesting to note that here the spread in the theoretical models is more constant over the range of momentum transfer than it is in either T_{10}^e or T_{11}^e. Also again we see the deviation in Phillips EFT

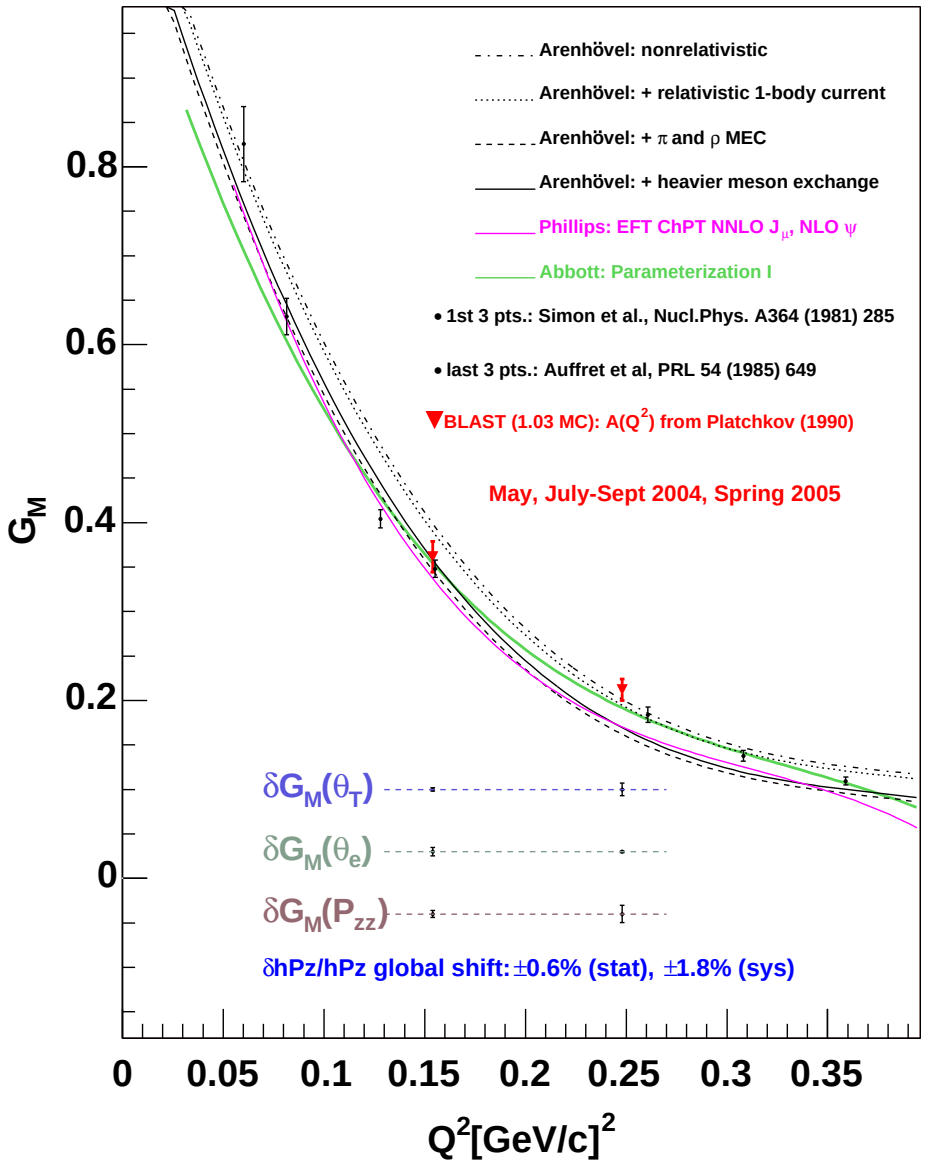

Figure 6-16: The Extraction of the Deuteron Magnetic Dipole Form Factor G_M from the BLAST data for T_{11}^e, T_{20}, T_{21}, and the structure function $A(Q^2)$ which has been taken from measurements at Saclay [5]

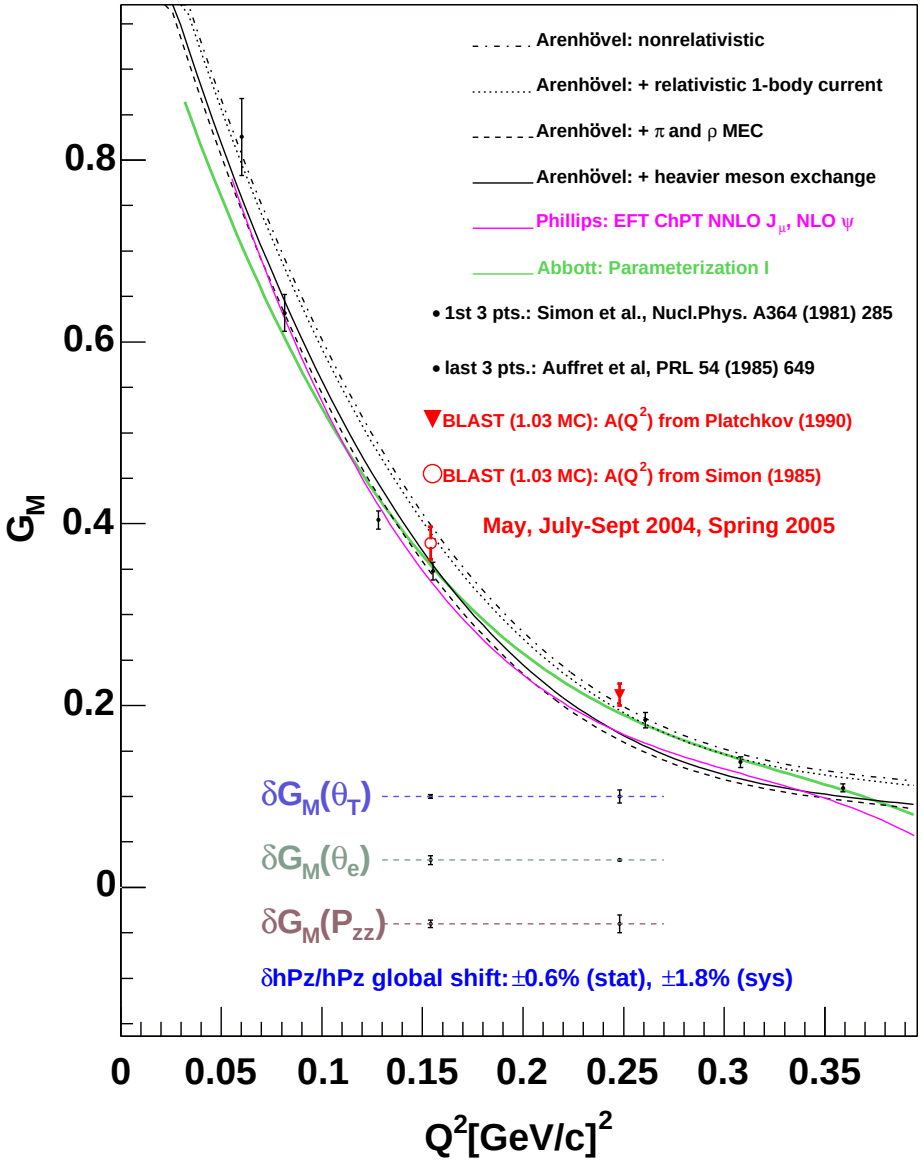

Figure 6-17: The Extraction of the Deuteron Magnetic Dipole Form Factor G_M from the BLAST data for T_{11}^e, T_{20}, T_{21}, and the structure function $A(Q^2)$ as obtained from world data. The value for G_M at the lower Q^2 point was obtained using the Mainz data [6] for $A(Q^2)$, whereas the higher Q^2 point was obtained using the Saclay data [5] for $A(Q^2)$

calculation occurring with its point of crossing Arenhövel's full calculation coinciding with the same Q^2 value as in T_{11}^e. Also note how the Abbott parameterization deviates slightly from the theory below $Q^2 < 0.12\ (GeV/c)^2$.

The world data on G_M are taken from the Rosenbluth separation experiments of Simon [6] and Auffret [71]. These data are plotted with statistical errors only. Of significance in these plots is the lack of world data on G_M in this low Q^2 region. A summary of the world data for G_M in the low Q^2 region is contained in Table 6.1 while current theoretical predictions for G_M at the Q^2 values of the BLAST data for T_{11}^e are contained in Table 6.2.

One can see that the values of G_M as extracted from the BLAST data are comparable

$Q^2 \left[\frac{GeV}{c}\right]^2$	$G_M \pm \delta G_M\ (stat.)$	Source
0.060	0.8255±0.0423	[6]
0.082	0.6319±0.0204	[6]
0.128	0.4042±0.0101	[6]
0.154	0.3615±0.0172	BLAST, [5]
0.154	0.3787±0.0180	BLAST, [6]
0.155	0.3479±0.0097	[6]
0.248	0.2119±0.0120	BLAST, [5]
0.261	0.1839±0.0086	[71]
0.308	0.1378±0.0059	[71]
0.359	0.1094±0.0044	[71]

Table 6.1: A summary of the world data for G_M based on Rosenbluth measurements of $B(Q^2)$ along with G_M extracted from the BLAST data for T_{11}^e, T_{20}, and T_{21} (statistical errors shown only)

with the world data as derived from the structure function $B(Q^2)$. It is important to note that the systematic errors associated with the Rosenbluth separations are not quoted here and the systematics on the BLAST extraction of G_M are relatively small, especially at the lower Q^2 point. These systematic errors, depending on the scattering angles θ_e and ϕ_e, as well as the target angle θ_T, were described in Section 6.4.4 and are tabulated in

Source	G_M at $0.154\left[\frac{GeV}{c}\right]^2$	G_M at $0.248\left[\frac{GeV}{c}\right]^2$
Arenhövel: Non-Relativistic [30]	0.399	0.201
Arenhövel: NR+1-Body Current [30]	0.389	0.195
Arenhövel: + π and ρ MECs [30]	0.349	0.162
Arenhövel: + heavier MECs [30]	0.358	0.169
Phillips: EFT ChPT [15]	0.338	0.170
Abbott: Parameterization I [7]	0.355	0.192

Table 6.2: A summary of values of G_M from various theoretical predictions and the Abbott parameterization I at the Q^2 points of the BLAST data for T_{11}^e.

Table 6.8 in the Results Summary Section 6.8.

Note that the first data point virtually overlaps the data of Auffret and the high Q^2 is very near the data of Simon. It was considered to combine all of the data into one point in Q^2 and hopefully place a data point in the gap between the Auffret and Simon data. However, the significantly greater amount of events at lower Q^2 due to the cross section would result in only a minimal shift from the current low Q^2 point. Regardless, the extraction of G_M from the BLAST data and the world data on $A(Q^2)$ represent a use of polarization observables, superior to T_{22} measurements [1], in obtaining the magnetic dipole form factor of the deuteron.

6.6 The Electric Monopole and Quadrupole Form Factors

In addition to the magnetic dipole form factor G_M, the electric monopole form factor G_C and the electric quadrupole form factor G_Q were extracted in this analysis as shown in Figures 6-14 and 6-15.

One can see from equation 2.17 that the deuteron electromagnetic structure function $A(Q^2)$ is dominated by G_C at low Q^2. This is due to the factor $\tau = Q^2/4M_d^2$ multiplying G_M and τ^2 multiplying G_Q. Therefore one would expect our extraction of G_C to be linked directly to the world data of Saclay and Mainz as shown in Figure 6-11. That

is, since $A(Q^2) \simeq G_C$ at low Q^2, we are essentially using G_C to extract G_C. Thus, this measurement of the electric monopole form factor is in essence, a consistency check.

The extracted values of G_C and G_Q are shown in Figures 6-18 and 6-19 respectively. Note that the values of G_C extracted from the BLAST data for T_{11}^e, T_{20}, T_{21}, and the Saclay measurement of the structure function $A(Q^2)$, virtually overlap the Abbott parameterization for the world data. This, along with the small error on G_C, are due to the fact that we are tightly constraining G_C through the use of $A(Q^2)$ in our X_ν^2 minimization. This can be seen in the very steep slopes of the X_ν^2 distribution for G_C in Figure 6-15. This means that only a miniscule change in G_C is required produce a ΔX_ν^2 equal to unity. This is likewise in the case of G_Q.

The sizes of the error bars on the form factors are directly affected by the small relative errors on the fits of the world data for $A(Q^2)$ shown in Figure 6-11 and the BLAST data for T_{20} and T_{21} of Figure 6-13. The small errors in these fits are due to the fact that we have combined all of the bins into just two for each measurement. This effect propagates into the error on the form factors and is exacerbated through the sensitivity of the form factors to the different parameters as will be shown in the next section. There is a strong dependence of G_C on $A(Q^2)$ and of G_Q on T_{20} and the small errors on the interpolated values of $A(Q^2)$ and T_{20} result in small errors on G_C and G_Q respectively. This effect is mitigated in the case of G_M as it will be shown that it is most sensitive to T_{11}^e which has a larger relative error than $A(Q^2)$ or T_{20}. The systematic errors on G_Q, primarily those due to P_{zz}, are more significant than in the case of G_C and prove to be limiting factor in the accuracy of this measurement.

6.7 Sensitivity of the Form Factors

A study was conducted to determine how sensitive each of the form factors was with respect to the parameters T_{11}^e, T_{20}, T_{21}, and $A(Q^2)$. This was done by observing the change

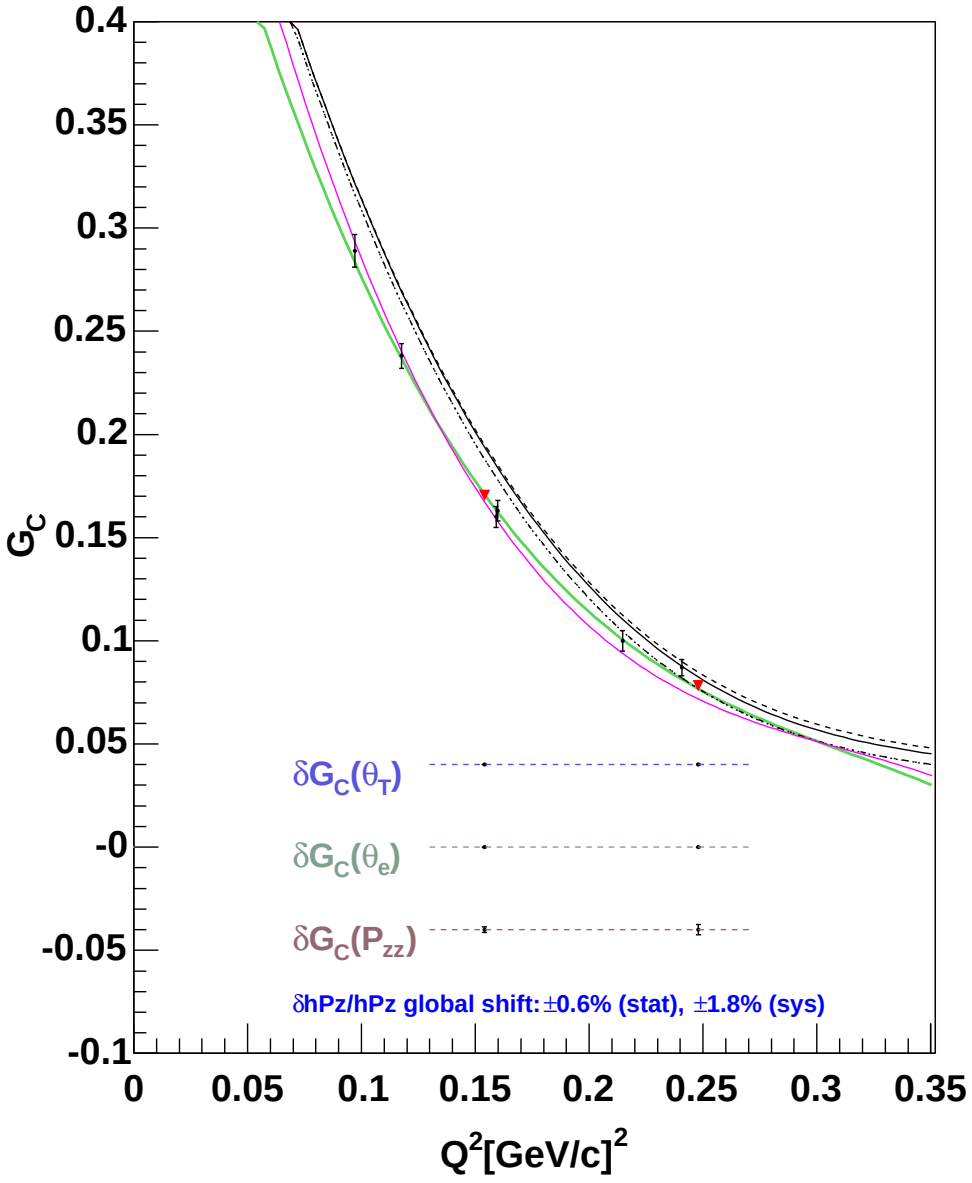

Figure 6-18: The Extraction of the Deuteron Electric Monopole Form Factor G_C from the BLAST data for T_{11}^e, T_{20}, T_{21}, and the structure function $A(Q^2)$ which has been taken from measurements at Saclay [5]. The extracted values of G_C based on the BLAST data are in red and the world data are taken from Abbott [7]. The legend for the curves is the same as in Figure 6-16

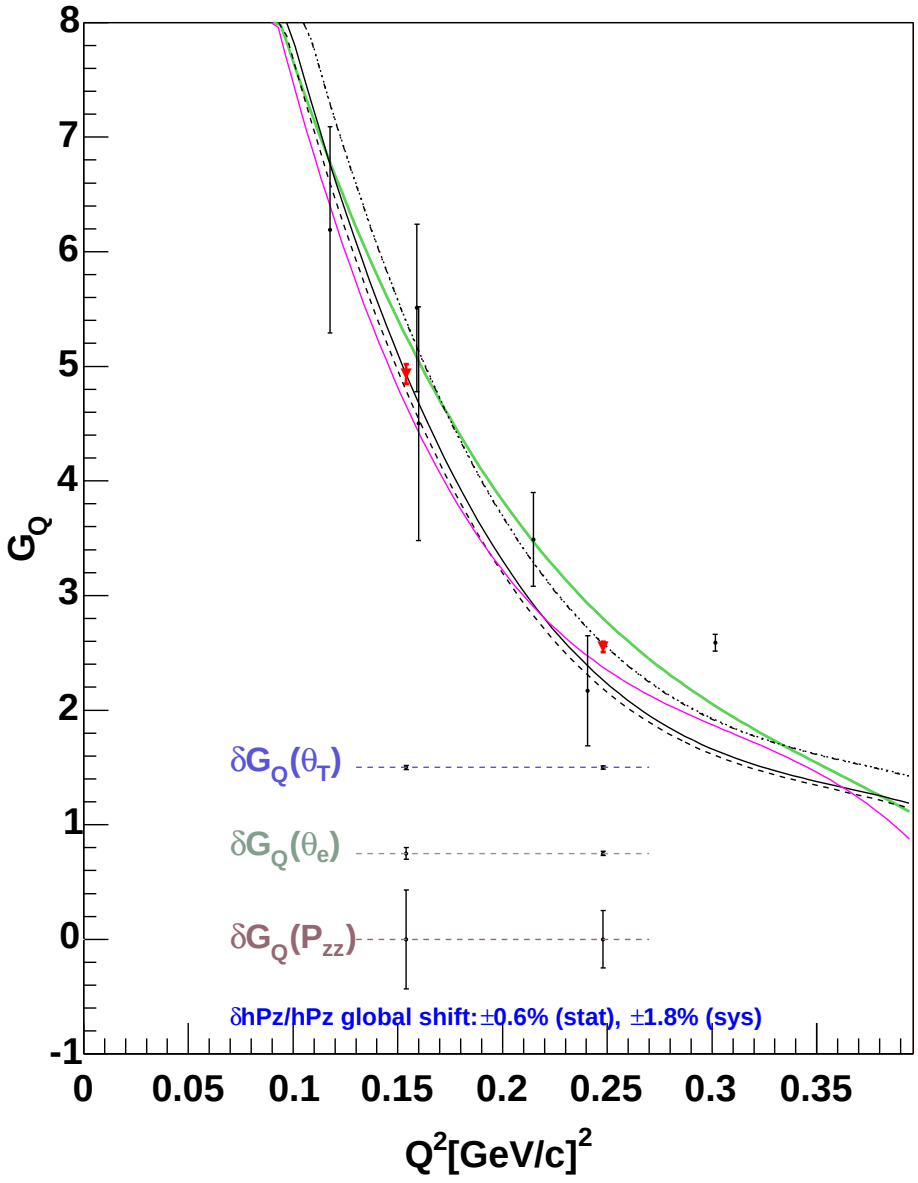

Figure 6-19: The Extraction of the Deuteron Electric Quadrupole Form Factor G_Q from the BLAST data for T_{11}^e, T_{20}, T_{21}, and the structure function $A(Q^2)$ which has been taken from measurements at Saclay [5] The extracted values of G_Q based on the BLAST data are in red and the world data are taken from Abbott [7]. The legend for the curves is the same as in Figure 6-16

$Q^2\left[\frac{GeV}{c}\right]^2$	Varied Parameter	ΔG_C [%]	ΔG_Q [%]	ΔG_M [%]
0.154	T_{11}^e	0.17	0.02	4.70
0.248	T_{11}^e	0.40	0.15	3.90
0.154	T_{20}	0.30	5.00	0.40
0.248	T_{20}	0.70	5.60	1.70
0.154	T_{21}	0.40	0.07	0.02
0.248	T_{21}	1.60	0.20	0.20
0.154	$A(Q^2)$	2.50	2.50	2.50
0.248	$A(Q^2)$	2.40	2.50	2.50

Table 6.3: Sensitivity of G_C, G_Q, G_M with respect to an independent 5% change in each of theparameters T_{11}^e, T_{20}, T_{21}, $A(Q^2)$

in the form factors when each of the parameters was independently varied by 5%. The results of this study appear in Table 6.3. Note how the extracted value of G_M depends strongly on the vector polarization observable T_{11}^e. Since it is T_{11}^e that is the focus of this work, it is appropriate that G_M, in light of its dependence on T_{11}^e, be the highlighted form factor measurement here. In the case of the electric quadrupole form factor G_Q, it is T_{20} that is the most influential parameter.

6.8 Results Summary

The BLAST data for the beam-target vector asymmetry, for the cases of perpendicular and parallel kinematics are shown in Tables 6.4, 6.5, and 6.6. These are broken into the three major data sets which are defined by target polarization angle as well as the value of hP_z.

The BLAST data for the vector polarization observables T_{10}^e and T_{11}^e are shown in Table 6.7. The BLAST data for the magnetic dipole form factor G_M, the electric quadrupole form factor G_C, and the electric monopole form factor G_Q are shown in Tables 6.8, 6.9 and 6.10 respectively.

$Q^2\left[\frac{GeV}{c}\right]^2$	$A^{ed}_{V,\perp}$	$\delta A_\perp$ $(stat.)$	$A^{ed}_{V,\parallel}$	$\delta A_\parallel$ $(stat.)$
0.151	-0.0478213	0.0090165	-	-
0.156	-	-	-0.0206789	0.0095255
0.247	-0.0617712	0.0201295	-	-
0.252	-	-	-0.0134370	0.0172329

Table 6.4: A^V_{ed} for May 2004: $\theta_T = 47°$, $hP_z = 0.44$, Charge = 87 kC, $\delta hP_z/hP_z$: 4.3% (statistical), 3.0% (systematic)

$Q^2\left[\frac{GeV}{c}\right]^2$	$A^{ed}_{V,\perp}$	$\delta A_\perp$ $(stat.)$	$A^{ed}_{V,\parallel}$	$\delta A_\parallel$ $(stat.)$
0.152	-0.0549425	0.0041096	-	-
0.156	-	-	-0.0492252	0.0040828
0.247	-0.0974621	0.0090899	-	-
0.251	-	-	-0.0587160	0.0071437

Table 6.5: A^V_{ed} for July-Sept 2004: $\theta_T = 32°$, $hP_z = 0.56$, Charge = 392 kC, $\delta hP_z/hP_z$: 1.6% (statistical), 2.3%(sys)

$Q^2\left[\frac{GeV}{c}\right]^2$	$A^{ed}_{V,\perp}$	$\delta A_\perp$ $(stat.)$	$A^{ed}_{V,\parallel}$	$\delta A_\parallel$ $(stat.)$
0.152	-0.0378992	0.00363181	-	-
0.157	-	-	-0.0199692	0.00365075
0.242	-0.0735461	0.00847195	-	-
0.252	-	-	-0.0417467	0.00595983

Table 6.6: A^V_{ed} for Spring 2005: $\theta_T = 47°$, $hP_z = 0.45$, Charge = 555 kC, $\delta hP_z/hP_z$: 0.7% (statistical), 2.9% (systematic)

$Q^2\left[\frac{GeV}{c}\right]^2$	T^e_{1q}	δT^e_{1q} $(stat.)$	$\delta T^e_{1q}(\theta_T)$	$\delta T^e_{1q}(\theta_e)$	$\delta T^e_{1q}(\phi_e)$
0.154	T^e_{10} = -0.01089	0.00472	0.00080	0.00011	2.0E-07
0.154	T^e_{11} = 0.05995	0.00289	0.00051	0.00110	2.0E-07
0.248	T^e_{10} = -0.01859	0.00836	0.00217	0.00214	6.0E-07
0.248	T^e_{11} = 0.10351	0.00657	0.00055	0.00200	1.0E-07

Table 6.7: T^e_{1q} for 2004 ($\theta_T = 47°$ and 32°), 2005 $\theta_T = 47°$, Charge = 1.03 MC, Combined $\delta hP_z/hP_z$: 0.6% (statistical), 1.8% (systematic)

$Q^2\left[\frac{GeV}{c}\right]^2$	$A(Q^2)$ Source	G_M	δG_M $(stat.)$	$\delta G_M(\theta_T)$	$\delta G_M(\theta_e)$	$\delta G_M(P_{zz})$
0.154	Saclay	0.3615	0.0172	0.0018	0.0049	0.0040
0.154	Mainz	0.3787	0.0180	0.0018	0.0049	0.0040
0.248	Saclay	0.2119	0.0120	0.0072	0.0008	0.0098

Table 6.8: G_M for 2004 ($\theta_T = 47^\circ$ and 32°), 2005 $\theta_T = 47^\circ$, Charge = 1.03 MC, Combined $\delta hP_z/hP_z$: 0.6% (statistical), 1.8% (systematic)

$Q^2\left[\frac{GeV}{c}\right]^2$	$A(Q^2)$ Source	G_Q	δG_Q $(stat.)$	$\delta G_Q(\theta_T)$	$\delta G_Q(\theta_e)$	$\delta G_Q(P_{zz})$
0.154	Saclay	4.933	0.087	0.020	0.051	0.432
0.154	Mainz	5.169	0.091	0.020	0.051	0.432
0.248	Saclay	2.552	0.044	0.015	0.018	0.250

Table 6.9: G_Q for 2004 ($\theta_T = 47^\circ$ and 32°), 2005 $\theta_T = 47^\circ$, Charge = 1.03 MC, Combined $\delta hP_z/hP_z$: 0.6% (statistical), 1.8% (systematic)

$Q^2\left[\frac{GeV}{c}\right]^2$	$A(Q^2)$ Source	G_C	δG_C $(stat.)$	$\delta G_C(\theta_T)$	$\delta G_C(\theta_e)$	$\delta G_C(P_{zz})$
0.154	Saclay	0.1706	0.0005	0.0001	0.0001	0.0014
0.154	Mainz	0.1787	0.0004	0.0001	0.0001	0.0014
0.248	Saclay	0.0782	0.0008	0.0001	0.0001	0.0025

Table 6.10: G_C for 2004 ($\theta_T = 47^\circ$ and 32°), 2005 $\theta_T = 47^\circ$, Charge = 1.03 MC, Combined $\delta hP_z/hP_z$: 0.6% (statistical), 1.8% (systematic)

CHAPTER 7

Summary and Outlook

The BLAST experiment, with its unique trio of the MIT-Bates intense polarized electron beam, polarized ABS internal target, and large acceptance spectrometer, provided a powerful instrument in the study of the deuteron vector polarization observables. The beam-target vector asymmetry, with the simultaneous cases of parallel and perpendicular kinematics, created a clever means in the extraction of the observables T_{10}^e and T_{11}^e. Even with the elastic electron-deuteron scattering cross section being in the nanobarn regime, BLAST allowed for the determination of T_{11}^e at two Q^2 points with sub-10% relative statistical error. This, in addition to the small systematic errors on T_{11}^e, resulted in the ability to use this measurement as a constraint on the various theoretical models of the NN interaction.

Confidence in this measurement also came in the form of the relative agreement of the BLAST data with that of the observables built out of the parameterizations of the world data by Abbott.

The use of the more statistically favorable quantity T_{11}^e, along with the BLAST tensor polarization observables T_{20} and T_{21}, and the world data for $A(Q^2)$, provided a new extraction the deuteron magnetic dipole form factor G_M from the spin observables. This experiment explored a region in Q^2 where not much data on G_M exists. This dearth of empirical results therefore makes future experiments desirable in this Q^2 region. In addition a consistency check was made of the electric monopole and quadrupole form factors G_C and G_Q.

This analysis has also brought to light once again the discrepancy in the world data for the measurement of the structure function $A(Q^2)$ at low Q^2 and provided additional impetus for new measurements in this region. It is encouraging to know that there is an approved proposal at Jefferson Lab to make a new measurment of $A(Q^2)$ [72] in this low Q^2 region.

At higher Q^2 values we have seen that the effective field theory calculations of T_{11}^e and G_M by Phillips deviate significantly from the predictions of Arenhövel and the Abbott parameterizations. The behaviour of this relatively recent approach to the deuteron provides an impetus for futher exploration in this region as well.

The measurements described in this monograph play but a small part in the grand picture of the NN interaction, but it is a part that is fundamental. Perhaps the road to the truth in electromagnetic nuclear physics is an asymptotic one, but with each new measurement, the truth becomes, ever so slightly, more clear.

List of References

[1] M. Garçon and W. Van Orden. *Adv.Nucl.Phys.*, 26:293, 2001.

[2] J.Mitchell (spokesperson). Cebaf proposal pr94-013, 1994.

[3] V. Ziskin. PhD thesis, Massachusetts Institute of Technology, 2005.

[4] C. Zhang. PhD thesis, Massachusetts Institute of Technology, 2006.

[5] S. Platchkov. *Nuc. Phys.*, A510:740, 1990.

[6] G.G. Simon. *Nuc. Phys.*, A364:285, 1981.

[7] D. Abbott. *Eur. Phys. J.*, pages 421–427, 2000.

[8] R.T. Birge and D.H. Menzel. *Phys. Rev.*, 37:1669(L), 1931.

[9] F.G. Brickwedde H.C. Urey and G.M. Murphy. *Phys. Rev.*, 39:164(L), 1932.

[10] W. Heisenberg. *Zeits. f. Physik*, 78:150, 1932.

[11] E. Fermi. *Nuovo Cimento*, 11:1, 1934.

[12] H.A. Bethe and R. Peirels. *Proc. Roy. Soc.*, A148:146, 1935.

[13] H. Yukawa. *Proc. Phys. Math Soc.*, 17:48, 1935.

[14] H. Arenhövel et al. *EPJA*, 10:183, 2001.

[15] D. Phillips. *Phys. Lett. B*, 567:12, 2003.

[16] R. Hofstadter. *Rev. Mod. Phys.*, 28:214, 1956.

[17] J. Carlson and R. Schiavilla. *Rev. Mod. Phys.*, 70:743, 1998.

[18] R. Gilman et al. *J. Phys. G: Nucl. Part. Phys.*, 28:R37–R116, 2002.

[19] M.E. Schulze. *Phys.Rev.Lett.*, 52:597, 1984.

[20] M. Garçon. *Nucl.Phys.*, pages 445c–454, 1990.

[21] I. The. PhD thesis, Massachusettes Institute of Technology, 1992.

[22] Z. Zhou. A study of the deuteron structure using tensor polarized deuterium and the blast detector, 2000.

[23] S. Boffi et al. *Electromagnetic Response of Atomic Nuclei.* Oxford University Press, 1996.

[24] T. DeForest and J.D. Walecka. *Adv. Phys.*, 15, 1966.

[25] M.N. Rosenbluth. *Phys. Rev.*, 79:615–619, 1950.

[26] T.W. Donnelly and A.S. Raskin. *Ann. Phys.*, 169:247, 1986.

[27] Z. Zhou. PhD thesis, University of Wisconsin, 1999.

[28] A.R. Edmunds. *Angular Momentum in Quantum Mechanics*. Princeton University Press, 1968.

[29] S.E. Darden. University of Wisconsin Press, Madison, Wisconsin, 1971.

[30] H. Arenhövel W. Leidemann and E.L. Tomusiak. *Z. Phys.*, A331:123, 1988.

[31] N.A. Jelley. *Fundamentals of Nuclear Physics*. Cambridge University Press, 1990.

[32] R.V. Reid. *Ann. Phys.*, 50:411, 1968.

[33] M. Lacombe et al. *Phys. Rev. C*, 21:861, 1980.

[34] Ch. Elster R. Machleidt, K. Holinde. *Phys. Rep.*, 149:1, 1987.

[35] Y. Song R. Machleidt, F. Sammarruca. *Phys. Rev. C*, 53:R1483, 1996.

[36] V.G.J. Stoks et al. *Phys. Rev. C*, 49:2950, 1994.

[37] R. Schiavilla R.B. Wiringa, V.G.J. Stoks. *Phys. Rev. C*, 51:38, 1995.

[38] M. Bouwhuis. PhD thesis, Universiteit Utrecht, 1998.

[39] M. Gari and H. Hyuga. *Phys. Rev. Lett.*, 36:345, 1976.

[40] E. Hummel and J.A. Tjon. *Phys. Rev. Lett.*, 63:1788, 1989.

[41] The BLAST Collaboration.

[42] http://mitbates.lns.mit.edu/bates/control/main MIT-Bates Website, 2004.

[43] The BLAST Collaboration, 1997.

[44] Townsend Zwart. (private communication), 2005.

[45] W.A. Franklin. *BLAST Compton Polarimeter Website*, 2003.

[46] M. Ferro-Luzzi. *Phys. Rev. Lett.*, 77:2630, 1996.

[47] Hauke Kolster. Conceptual design report for the atomic beam source of the blast polarized deuterium target, 2002.

[48] L.W. Anderson and D.R. Swenson. *Nuclear Instrumentation and Methods*, page 157, 1985.

[49] J.B. Birks. *The Theory and Practice of Scintillation Counting.* Pergamon Press, 1964.

[50] W.R. Leo. *Techniques for Nuclear and Particle Physics Experiments: A How-To Approach.* Springer-Verlag, 1996.

[51] R.T. Giles. *Nuclear Instruments and Methods in Physics Research*, A252, 1986.

[52] Bicron Saint-Gobain Detectors. Bc-408: Premium plastic scintillator, 2003.

[53] D. Hasell. Blast drift chamber report, the blast collaboration, 1998.

[54] C. Crawford. PhD thesis, Massachusetts Institute of Technology, 2005.

[55] D. Hasell. (private communication), 2005.

[56] Frederick Tong uk Lee. (private communication), 2005.

[57] O. Filoti. *The Čerenkov Counters for the BLAST Detectors, APS-DNP Fall Meeting, Chicago*, 2004.

[58] Michael Kohl, 2004.

[59] K. Dow. (private communication), 2005.

[60] R. Alarcon (BLAST Collaboration). *Electronuclear Physics with Internal Targets and the BLAST Detector*, page 1, 1999.

[61] D. Hasell. (private communication), 2002.

[62] Taylan Akdogan. (private communication), 2005.

[63] A. Maschinot. PhD thesis, Massachusetts Institute of Technology, 2005.

[64] J. Friedrich and T. Walcher. *Eur. Phys. J.*, page 607, 2003.

[65] Chi Zhang, 2004.

[66] K. Dow et al. *Magnetic Measurements of the BLAST Spectrometer*, 2005.

[67] A. Sindile. The blast mysql database, 2002.

[68] N. Merenkov A. Afanasev, I. Akushevich. *JETP*, 98:403–416, 2003.

[69] H. Arenhövel et al. (private communication), 2004.

[70] P.R. Bevington and K.D. Robinson. *Data Reduction and Error Analysis for the Physical Sciences.* McGraw-Hill, 2002.

[71] S. Auffret et al. *Phys. Rev Lett.*, 54:649, 1985.

[72] X. Jiang (spokesperson) R.Gilman, D. Higinbotham. Jlab proposal e-05-004, 2005.

APPENDIX

Deuteron Static Properties

Charge: $1.6E-19\ C$
Mass: 1875.58 $[MeV/c^2]$
Spin and Parity: $J^\pi = 1^+ \rightarrow$ Allowed states $(L,S) = (0,1)$ [$\sim 96\%$] or $(2,1)$ [$\sim 4\%$][1]
Magnetic Moment: $\mu_D = +0.8574\mu_N$
Quadrupole Moment: $Q_D = 0.2859\ [fm^2]$
Radius: 1.96 $[fm]$
Isospin: $T = 0$
Binding Energy: 2.2245 $[MeV]$

Deuteron Elastic Form Factors

$$G_C(Q^2 \rightarrow 0) = 1 \tag{A-1}$$
$$G_Q(Q^2 \rightarrow 0) = M_D^2 Q_D = 25.83 \tag{A-2}$$
$$G_M(Q^2 \rightarrow 0) = (M_D/M)\mu_D = 1.714 \tag{A-3}$$

Kinematics

$$Q^2 \simeq 4\epsilon\epsilon' \sin^2\left(\frac{\theta_{\mathbf{kk'}}}{2}\right) \qquad (ERL) \tag{A-4}$$
$$\epsilon' = \frac{\epsilon}{(1 + \frac{2\epsilon \sin^2(\theta_e/2)}{M_d})} \tag{A-5}$$
$$\theta_e = 2\sin^{-1}\sqrt{\frac{Q^2}{(4\epsilon^2 - \frac{2\epsilon Q^2}{M_d})}} \tag{A-6}$$
$$\theta_d = \sin^{-1}\left(\frac{1}{1+\tan^2(\frac{\theta_e}{2})(\frac{\epsilon}{M_d}+1)}\right)^{\frac{1}{2}} \tag{A-7}$$

Rosenbluth Cross Section

$$\sigma_0 = \sigma_{Mott} \cdot \left(\frac{\epsilon'}{\epsilon}\right) \cdot \left[A(Q^2) + B(Q^2)\tan^2\frac{\theta_e}{2}\right] \tag{A-8}$$

[1] P_S and P_D are model dependent!

$$A(Q^2) \;=\; G_C^2(Q^2) + \frac{8}{9}\tau^2 G_Q^2(Q^2) + \frac{2}{3}\tau G_M^2(Q^2) \tag{A-9}$$

$$B(Q^2) \;=\; \frac{4}{3}\tau(1+\tau)G_M^2(Q^2) \tag{A-10}$$

$$\tau \;=\; \frac{Q^2}{4M_d^2} \tag{A-11}$$

Vector & Tensor Elastic Polarization Observables

$$A_{ed}^V \;\equiv\; \frac{\Delta}{\Sigma} \;=\; hP_z\sqrt{3}\Big[\frac{1}{\sqrt{2}}\cos\theta^* T_{10}^e(Q,\theta_e) - \sin\theta^*\cos\phi^* T_{11}^e(Q,\theta_e)\Big] \tag{A-12}$$

$$T_{10}^e(Q^2,\theta_e) \;=\; -\sqrt{\frac{2}{3}}\frac{1}{S}\tau\{(1+\tau)[1+\tau\sin^2(\theta_e/2)]\}^{1/2} G_M^2 \tan\frac{\theta_e}{2}\sec\frac{\theta_e}{2} \tag{A-13}$$

$$T_{11}^e(Q^2,\theta_e) \;=\; \sqrt{\frac{3}{2}}\frac{1}{S}\frac{4}{3}[\tau(1+\tau)]^{1/2} G_M(G_C + \frac{\tau}{3}G_Q)\tan\frac{\theta_e}{2} \tag{A-14}$$

$$T_{20}(Q^2,\theta_e) \;=\; -\sqrt{2}\frac{1}{S}\tau\Big(\frac{4}{3}G_C G_Q + \frac{4}{9}G_Q^2 + \frac{1}{6}(1+(\tau+1)\tan^2(\theta_e/2))G_M^2\Big) \tag{A-15}$$

$$T_{21}(Q^2,\theta_e) \;=\; -\frac{2}{\sqrt{3}}\frac{1}{S}\tau\Big(\tau+\tau^2\sin^2(\theta_e/2)\Big)^{1/2} G_M G_Q \sec\frac{\theta_e}{2} \tag{A-16}$$

$$T_{22}(Q^2,\theta_e) \;=\; -\frac{1}{2\sqrt{3}}\frac{1}{S}\tau G_M^2 \tag{A-17}$$

$$T_{kq} \;=\; t_{kq}(-1)^{k+q} \tag{A-18}$$

T_{kq} are analyzing powers (for polarized target measurement)
t_{kq} are polarization tensors (for recoil polarization measurement)

Relate spherical tensors t_{kq} to cartesian moments,

$$t_{10} = \sqrt{\frac{3}{2}}p_z \tag{A-19}$$

$$t_{1\pm1} = \mp\frac{\sqrt{3}}{2}(p_x \pm ip_y) \tag{A-20}$$

Experimental Asymmetry from Arenhövel's Cross Section

$$\sigma(h,P_z,P_{zz}) \;=\; \sigma_0[1 + hA_e + P_z A_d^V + P_{zz}A_d^T + h(P_z A_{ed}^V + P_{zz}A_{ed}^T)] \tag{A-21}$$

Note: A_e=A_{ed}^T=A_d^V=0 in the OPE approximation.

$$P_z = n_+ - n_- \qquad \text{(vector polarization)} \tag{A-22}$$

$$P_{zz} = n_+ + n_- - 2n_0 \qquad \text{(tensor polarization)} \tag{A-23}$$

$$n_+ + n_- + n_0 \;=\; 1 \tag{A-24}$$

$$A_{ed}^V \;=\; \frac{1}{4hP_z\sigma_0}[\sigma(+,+,+1) - \sigma(-,+,+1) - \sigma(+,-,+1) + \sigma(-,-,+1)] \tag{A-25}$$

where σ_0 is the total cross section for all beam-target states.

VITA

Peter Joseph Karpius

Peter Joseph Karpius was born in Danbury, CT USA on 4 November 1969. He received a Bachelor of Science degree in Physics from the State University if New York, College at Cortland in 1993. A year and a half later in 1994 he completed a second Bachelor's degree in Mechanical Engineering at Clarkson University in Potsdam, NY. After contracting as a Field Engineer at Vermont Yankee Nuclear Power he attended Cornell University in Ithaca, NY completing a Master of Engineering degree in Engineering Physics there in 1996 with research done in experimental plasma physics. From 1996 to 2000 he was employed as a Spacecraft Integration, Research and Design Engineer at Space Systems Loral in Palo Alto, CA. While at Loral he continued his education taking courses at Stanford University and UC Berkeley. He passed the State of California EIT/FE exam in 1999. In July 2000 he entered the graduate program at the University of New Hampshire where, in 2004, he received a Master of Science degree in Physics. This dissertation was defended at the University of New Hampshire on 18 October 2005.